



DTIC
JAN 04 1995

19941228084

PERFORMANCE CHARACTERIZATION OF A
HIGHLY-OFFSET DIFFUSER WITH AND
WITHOUT BLOWING VORTEX
GENERATOR JETS

THESIS
Michael B. Senseney
Captain, USAF

AFIT/GAE/ENY/94D-14

DEPARTMENT OF THE AIR FORCE
AIR UNIVERSITY
AIR FORCE INSTITUTE OF TECHNOLOGY

Wright-Patterson Air Force Base, Ohio

DTIC

Approved for public release;
Distribution unlimited

AFIT/GAE/ENY/94D-14

PERFORMANCE CHARACTERIZATION OF A
HIGHLY-OFFSET DIFFUSER WITH AND
WITHOUT BLOWING VORTEX
GENERATOR JETS

THESIS
Michael B. Senseney
Captain, USAF

AFIT/GAE/ENY/94D-14

DRAFT QUALITY IMPROVED 2

Approved for public release; distribution unlimited

The views expressed in this thesis are those of the author and do not reflect the official policy or position of the Department of Defense or the U. S. Government.

Accession For	
NTIS	CRA&I <input checked="" type="checkbox"/>
DTIC	TAB <input type="checkbox"/>
Unannounced <input type="checkbox"/>	
Justification _____	
By _____	
Distribution /	
Available Copies	
Dist	Approved for Distribution
A-1	

AFIT/GAE/ENY/94D-14

PERFORMANCE CHARACTERIZATION OF A
HIGHLY-OFFSET DIFFUSER WITH AND
WITHOUT BLOWING VORTEX
GENERATOR JETS

THESIS

Presented to the Faculty of the School of Engineering
of the Air Force Institute of Technology
Air University
In Partial Fulfillment of the
Requirements for the Degree of
Master of Science

Michael B. Senseney, B.S.
Captain, USAF

December 1994

Approved for public release; distribution unlimited

Preface

This document is the end product of nearly a year's work, and what a year it was.

Last November, this research program was just an vaguely-defined idea in my head. In the time since then, it was fleshed out, whittled down, built up, tested upon, analyzed, and, now, written up, signed, sealed, and delivered. When tests went well, probes didn't break, the compressors ran, and the computers cooperated, the whole experience was very exciting and encouraging. I'm sure I learned more through the execution of this program than the results of this study could possibly imply.

I can claim very little of the credit for this work for myself. I had outstanding support from my advisory team: Major Thomas Buter, Dr Rodney D. W. Bowersox, and Dr Philip Beran. My personal thanks to each for their own contributions: Major Buter, for agreeing to take on this experiment, for not being above turning a wrench every now and then, and for understanding that there was more to life than school; Dr Bowersox, for his experimental expertise and assistance in test setup and data reduction; and Dr Beran, for careful review of the drafts of this thesis. Each of these gentlemen demanded a quality product, and I hope I have not let them down.

The AFIT model shop was simply superb in their support of this experiment. It could not have been undertaken without their willingness to help me determine the best ways to build things and their hard work to construct and modify my apparatus, sometimes, literally, while I waited. Thanks to Mr Jack Tiffany, Mr David Driscoll, Mr John Brohas, and, especially, Mr Joe Hoeffel, for putting up with a dumb engineer in your

REPORT DOCUMENTATION PAGE

Form Approved
OMB No. 0704-0188

Public reporting burden for this collection of information is estimated to average 1 hour per response, including the time for reviewing instructions, searching existing data sources, gathering and maintaining the data needed, and completing and reviewing the collection of information. Send comments regarding this burden estimate or any other aspect of this collection of information, including suggestions for reducing this burden, to Washington Headquarters Services, Directorate for Information Operations and Reports, 1215 Jefferson Davis Highway, Suite 1204, Arlington, VA 22202-4302, and to the Office of Management and Budget, Paperwork Reduction Project (0704-0188), Washington, DC 20503.

1. AGENCY USE ONLY (Leave blank)			2. REPORT DATE December 1994		3. REPORT TYPE AND DATES COVERED Master's Thesis		
4. TITLE AND SUBTITLE Performance Characterization of a Highly-Offset Diffuser with and without Blowing Vortex Generator Jets			5. FUNDING NUMBERS				
6. AUTHOR(S) Michael B. Senseney, Captain, USAF							
7. PERFORMING ORGANIZATION NAME(S) AND ADDRESS(ES) Air Force Institute of Technology WPAFB, OH 45433-6583			8. PERFORMING ORGANIZATION REPORT NUMBER AFIT/GAE/ENY/94D-14				
9. SPONSORING / MONITORING AGENCY NAME(S) AND ADDRESS(ES) WL/FIMA Wright-Patterson AFB, OH 45433-6583			10. SPONSORING / MONITORING AGENCY REPORT NUMBER				
11. SUPPLEMENTARY NOTES							
12a. DISTRIBUTION / AVAILABILITY STATEMENT Approved for public release; distribution unlimited				12b. DISTRIBUTION CODE			
13. ABSTRACT (Maximum 200 words) The effect of blowing vortex generator jets (VGJs) on the performance of a highly-offset (s-duct) diffuser was investigated experimentally. VGJs are pitched, skewed jets which generate streamwise vortices as well as injecting high-momentum fluid into the boundary layer. Diffuser performance with and without VGJs was measured for an inlet Mach number of 0.6 ($Re/x = 1.27e7$ per cm). Pitot static and hot-film instrumentation was used to measure flow properties at the diffuser inlet and exit planes. Without blowing, the flow on the lower surface of the diffuser was massively separated. Blowing at 0.48% mass flow ratio through three lower-surface VGJs reduced the size of the separated flow region, reduced the thickness of the boundary layer at the exit plane, increased pressure recovery by 1.3%, and increased the static pressure rise achieved in the diffuser by over 50%. Turbulence intensity, turbulent shear stress, and turbulent kinetic energy were reduced as well. Distortion of the exit plane flowfield increased with blowing.							
14. SUBJECT TERMS Boundary Layer, Boundary Layer Control, Diffusers, Subsonic Diffusers, Turbulent Boundary Layer, Vortex Generators					15. NUMBER OF PAGES 186		
					16. PRICE CODE		
17. SECURITY CLASSIFICATION OF REPORT UNCLASSIFIED		18. SECURITY CLASSIFICATION OF THIS PAGE UNCLASSIFIED		19. SECURITY CLASSIFICATION OF ABSTRACT UNCLASSIFIED		20. LIMITATION OF ABSTRACT UL	

GENERAL INSTRUCTIONS FOR COMPLETING SF 298

The Report Documentation Page (RDP) is used in announcing and cataloging reports. It is important that this information be consistent with the rest of the report, particularly the cover and title page. Instructions for filling in each block of the form follow. It is important to stay within the lines to meet optical scanning requirements.

Block 1. Agency Use Only (Leave blank).

Block 2. Report Date. Full publication date including day, month, and year, if available (e.g. 1 Jan 88). Must cite at least the year.

Block 3. Type of Report and Dates Covered.

State whether report is interim, final, etc. If applicable, enter inclusive report dates (e.g. 10 Jun 87 - 30 Jun 88).

Block 4. Title and Subtitle. A title is taken from the part of the report that provides the most meaningful and complete information. When a report is prepared in more than one volume, repeat the primary title, add volume number, and include subtitle for the specific volume. On classified documents enter the title classification in parentheses.

Block 5. Funding Numbers. To include contract and grant numbers; may include program element number(s), project number(s), task number(s), and work unit number(s). Use the following labels:

C - Contract	PR - Project
G - Grant	TA - Task
PE - Program Element	WU - Work Unit
	Accession No.

Block 6. Author(s). Name(s) of person(s) responsible for writing the report, performing the research, or credited with the content of the report. If editor or compiler, this should follow the name(s).

Block 7. Performing Organization Name(s) and Address(es). Self-explanatory.

Block 8. Performing Organization Report Number. Enter the unique alphanumeric report number(s) assigned by the organization performing the report.

Block 9. Sponsoring/Monitoring Agency Name(s) and Address(es). Self-explanatory.

Block 10. Sponsoring/Monitoring Agency Report Number. (If known)

Block 11. Supplementary Notes. Enter information not included elsewhere such as: Prepared in cooperation with...; Trans. of...; To be published in.... When a report is revised, include a statement whether the new report supersedes or supplements the older report.

Block 12a. Distribution/Availability Statement.

Denotes public availability or limitations. Cite any availability to the public. Enter additional limitations or special markings in all capitals (e.g. NOFORN, REL, ITAR).

DOD - See DoDD 5230.24, "Distribution Statements on Technical Documents."

DOE - See authorities.

NASA - See Handbook NHB 2200.2.

NTIS - Leave blank.

Block 12b. Distribution Code.

DOD - Leave blank.

DOE - Enter DOE distribution categories from the Standard Distribution for Unclassified Scientific and Technical Reports.

NASA - Leave blank.

NTIS - Leave blank.

Block 13. Abstract. Include a brief (Maximum 200 words) factual summary of the most significant information contained in the report.

Block 14. Subject Terms. Keywords or phrases identifying major subjects in the report.

Block 15. Number of Pages. Enter the total number of pages.

Block 16. Price Code. Enter appropriate price code (NTIS only).

Blocks 17. - 19. Security Classifications. Self-explanatory. Enter U.S. Security Classification in accordance with U.S. Security Regulations (i.e., UNCLASSIFIED). If form contains classified information, stamp classification on the top and bottom of the page.

Block 20. Limitation of Abstract. This block must be completed to assign a limitation to the abstract. Enter either UL (unlimited) or SAR (same as report). An entry in this block is necessary if the abstract is to be limited. If blank, the abstract is assumed to be unlimited.

shops. It is truly unfortunate that such a valuable resource - not to mention several gifted craftsmen - is on the cutting block in the face of budget reductions.

The personnel who run the AFIT/ENY laboratories also deserve recognition for their support, particularly Mr Jay Anderson, Mr Andy Pitts, and Mr Charles McNeeley. Their help in setting up the facility, operating the data acquisition equipment, and troubleshooting equipment problems was invaluable.

I owe a deep debt of gratitude to Col (select) Perry Lamy and the late Col Frank T. Birk, formerly of the 412 Test Group, for going to bat for me earlier in my career. Without their interest and initiative, I would no longer be in the Air Force.

On a more personal level, I inherited my work ethic - and my love of airplanes - from my father, Maj Morton P. Senseney, USAF (Ret). Thank you, dad, for teaching me well.

To my wife of three months and a few days, Lorraine, I say thank you for your understanding and encouragement. You kept me going many times when discouragement tried to take hold. Your cheery attitude, warm smile, and delicious cookies wouldn't let me get too far down. Now I'm yours again.

I am most greatly indebted, though, to our Lord and Maker. It is He who made me what I am, gave me the abilities that I have, and allowed me to accomplish this project. May this work bring glory to You, O Lord, and may I serve You forever.

Table of Contents

Preface	ii
List of Figures	vi
List of Tables	xii
List of Symbols	xiii
Abstract	xvi
I. Introduction	1
Background	3
Objective	6
Outline	6
II. Theory	8
Coordinate System	9
Boundary Layer Growth, Transition, and Turbulence	9
Adverse Pressure Gradients, Secondary Flows, and Separation	15
Vortex Generator Jet Theory	18
Diffuser Performance Criteria	22
Summary of Related Numerical Work	26
III. Test Apparatus, Instrumentation, and Procedure	29
Facility	29
Test Diffuser Geometry	32
Measurement Planes and Instrumentation	36
Test Procedures and Conditions	44
IV. Results and Discussion	49
Mean Flow Properties	50
Turbulent Flow Properties	78

V. Conclusions and Recommendations	85
Conclusions	85
Recommendations	87
 Figures	90
Appendix A: Uncertainty Analysis	138
Appendix B: Run Log	148
Appendix C: Hot-Film Probe Data Repeatability Check	163
Bibliography	167
Vita	170

List of Figures

<u>Figure</u>		<u>Page</u>
1.	Coordinate System With Respect to Diffuser	90
2.	Laminar and Turbulent Boundary Layer Profiles (Hill and Peterson, 1992:100)	90
3.	Coles' Law of the Wake Parameter Π (White, 1991:452)	91
4.	Law of the Wall Velocity Profile (Schetz, 1993:209)	91
5.	Boundary Layer Growth to Separation (Schlichting, 1951:34)	92
6.	Jet-Induced Vortices (after Zhang and Collins, 1993)	92
7.	AFIT Subsonic Diffuser Test Facility	93
8.	Diffuser Installed in Test Facility	93
9.	Diffuser Flowpath Details	94
10.	Test Section Upper and Lower Surfaces	95
11.	Assembled Test Section	95
12.	TSI Model 1218 Hot-Film Probe (TSI, 1987)	96
13.	TSI Model 1243 Hot-Film Probe (TSI, 1987)	96
14.	$M_1 = 0.6$ Inlet Plane Total Pressure Recovery Map	97
15.	$M_1 = 0.6$ Inlet Plane Total Pressure Recovery Profile	97
16.	$M_1 = 0.6$ Inlet Plane Total Pressure Recovery Profile	98
17.	$M_1 = 0.8$ Inlet Plane Total Pressure Recovery Map	98
18.	$M_1 = 0.6$ Inlet Plane Mach Number Map	99
19.	$M_1 = 0.8$ Inlet Plane Mach Number Map	99

<u>Figure</u>	<u>Page</u>
20. $M_1 = 0.6$ Inlet Plane Lower Surface $\frac{y}{\delta}$ vs $\frac{\bar{u}}{U_e}$ @ $z/b = 0.5$	100
21. $M_1 = 0.6$ Inlet Plane Lower Surface $\frac{y}{\delta}$ vs $\frac{\bar{u}}{U_e}$ @ $z/b = 0.3$	100
22. $M_1 = 0.8$ Shadowgraph	101
23. Sketch of Lower Surface Flow Pattern Without Blowing	101
24. Photograph of Sidewall Streaklines Showing Secondary Flow Direction ..	102
25. Sketch of Lower Surface Flow Pattern at $\frac{\dot{m}_j}{\dot{m}_d} = 0.0025$	102
26. Sketch of Lower Surface Flow Pattern at $\frac{\dot{m}_j}{\dot{m}_d} = 0.0048$	103
27. Lower Surface Static Pressure Coefficient vs x	103
28. $M_1 = 0.6$ Exit Plane Total Pressure Recovery Map with Blowing Off	104
29. $M_1 = 0.8$ Exit Plane Total Pressure Recovery Map with Blowing Off	104
30. $M_1 = 0.6$ Exit Plane Total Pressure Recovery Map with $\frac{\dot{m}_j}{\dot{m}_d} = 0.0048$...	105
31. Total Pressure Recovery Profiles @ $z/b = 0.1$	105
32. Total Pressure Recovery Profiles @ $z/b = 0.2$	106
33. Total Pressure Recovery Profiles @ $z/b = 0.3$	106
34. Total Pressure Recovery Profiles @ $z/b = 0.4$	107
35. Total Pressure Recovery Profiles @ $z/b = 0.5$	107
36. Total Pressure Recovery Profiles @ $z/b = 0.6$	108
37. Total Pressure Recovery Profiles @ $z/b = 0.7$	108

<u>Figure</u>	<u>Page</u>
38. Total Pressure Recovery Profiles @ $z/b = 0.8$	109
39. Total Pressure Recovery Profiles @ $z/b = 0.9$	109
40. Total and Static Pressure Recovery Profiles @ $z/b = 0.1$	110
41. Total and Static Pressure Recovery Profiles @ $z/b = 0.3$	110
42. Total and Static Pressure Recovery Profiles @ $z/b = 0.5$	111
43. Total and Static Pressure Recovery Profiles @ $z/b = 0.7$	111
44. Total and Static Pressure Recovery Profiles @ $z/b = 0.9$	112
45. $M_1 = 0.6$ Exit Plane Static Pressure Recovery Map with Blowing Off	113
46. $M_1 = 0.6$ Exit Plane Static Pressure Recovery Map with $\frac{\dot{m}_j}{\dot{m}_d} = 0.0048$	113
47. $M_1 = 0.6$ Exit Plane Mach Number Map with Blowing Off	114
48. $M_1 = 0.6$ Exit Plane Mach Number Map with $\frac{\dot{m}_j}{\dot{m}_d} = 0.0048$	114
49. Mach Number Profiles Computed From Pitot-Static Data @ $z/b = 0.1$	115
50. Mach Number Profiles Computed From Pitot-Static Data @ $z/b = 0.3$	115
51. Mach Number Profiles Computed From Pitot-Static Data @ $z/b = 0.5$	116
52. Mach Number Profiles Computed From Pitot-Static Data @ $z/b = 0.7$	116
53. Mach Number Profiles Computed From Pitot-Static Data @ $z/b = 0.9$	117
54. Mach Number Profiles Computed From Cross-Film Data @ $z/b = 0.3$	117
55. Mach Number Profiles Computed From Cross-Film Data @ $z/b = 0.5$	118

<u>Figure</u>	<u>Page</u>
56. Mach Number Profiles Computed From Cross-Film Data @ $z/b = 0.7$	118
57. Mach Number Profile Computed From Normal-Film Data - $z/b = 0.3$	119
58. Mach Number Profile Computed From Normal-Film Data @ $z/b = 0.5$	119
59. Comparison of 3 Sources for Mach Number - Blowing Off, $z/b = 0.5$	120
60. Mean Velocity Component Profiles - Blowing Off, $z/b = 0.3$	120
61. Mean Velocity Component Profiles - Blowing Off, $z/b = 0.5$	121
62. Mean Velocity Component Profiles - Blowing Off, $z/b = 0.7$	121
63. Mean Velocity Component Profiles - Blowing On, $z/b = 0.3$	122
64. Mean Velocity Component Profiles - Blowing On, $z/b = 0.5$	122
65. Mean Velocity Component Profiles - Blowing On, $z/b = 0.7$	123
66. Mean Flow Angle Profiles - Blowing Off, $z/b = 0.3$	123
67. Mean Flow Angle Profiles - Blowing Off, $z/b = 0.5$	124
68. Mean Flow Angle Profiles - Blowing Off, $z/b = 0.7$	124
69. Mean Flow Angle Profiles - Blowing On, $z/b = 0.3$	125
70. Mean Flow Angle Profiles - Blowing On, $z/b = 0.5$	125
71. Mean Flow Angle Profiles - Blowing On, $z/b = 0.7$	126
72. Hypothesized Vortex Arrangement at the Exit Plane - Blowing On	126
73. Turbulence Intensity (Cross-Film) - Blowing Off, $z/b = 0.3$	127
74. Turbulence Intensity (Cross-Film) - Blowing Off, $z/b = 0.5$	127

<u>Figure</u>	<u>Page</u>
75. Turbulence Intensity (Cross-Film) - Blowing Off, $z/b = 0.7$	128
76. Turbulence Intensity (Normal-Film) - Blowing Off, $z/b = 0.3$	128
77. Turbulence Intensity (Normal-Film) - Blowing Off, $z/b = 0.5$	129
78. Turbulence Intensity (Cross-Film) - Blowing On, $z/b = 0.3$	129
79. Turbulence Intensity (Cross-Film) - Blowing On, $z/b = 0.5$	130
80. Turbulence Intensity (Cross-Film) - Blowing On, $z/b = 0.7$	130
81. Turbulence Intensity (Cross-Film) Nondimensionalized by U_∞	131
- Blowing Off, $z/b = 0.5$	
82. Turbulence Intensity (Cross-Film) Nondimensionalized by U_∞	131
- Blowing On, $z/b = 0.5$	
83. Turbulent Kinetic Energy - Blowing On and Off, $z/b = 0.3$	132
84. Turbulent Kinetic Energy - Blowing On and Off, $z/b = 0.5$	132
85. Turbulent Kinetic Energy - Blowing On and Off, $z/b = 0.7$	133
86. Turbulent Kinetic Energy Nondimensionalized by U_∞^2	133
- Blowing On and Off, $z/b = 0.5$	
87. Turbulent Shear Stress Components - Blowing Off, $z/b = 0.3$	134
88. Turbulent Shear Stress Components - Blowing Off, $z/b = 0.5$	134
89. Turbulent Shear Stress Components - Blowing Off, $z/b = 0.7$	135
90. Turbulent Shear Stress Components - Blowing On, $z/b = 0.3$	135
91. Turbulent Shear Stress Components - Blowing On, $z/b = 0.5$	136
92. Turbulent Shear Stress Components - Blowing On, $z/b = 0.7$	136

<u>Figure</u>	<u>Page</u>
93. Turbulent Shear Stress Components Nondimensionalized by U_{∞}^2 - Blowing Off, $z/b = 0.5$	137
94. Turbulent Shear Stress Components Nondimensionalized by U_{∞}^2 - Blowing On, $z/b = 0.5$	137

List of Tables

Table	Page
1. Test Diffuser Geometric Reference Values	33
2. Test Section Dimensions	35
3. Uncertainty Analysis Summary	43
4. Test Matrix	48
5. Inlet Plane Boundary Layer Measurements	52
6. Total Pressure-Based Diffuser Performance Comparison	63
7. Diffuser Exit Plane Pressure Coefficient	69

List of Symbols

Symbol	Quantity
A_e	Diffuser Exit Area
A_i	Diffuser Inlet Area
b	Test Section Span
BLC	Boundary Layer Control
C_f	Coefficient of Friction
C_p	Pressure Coefficient
CFD	Computational Fluid Dynamics
D_{eq}	Equivalent Diameter = $4A/\pi$
d	Jet Diameter
M	Mach Number
m_d	Diffuser Inlet Mass Flow
\dot{m}_j	Blowing Mass Flow
N	Number of Data Samples
n	$N - 1$
Nu	Nusselt Number
P	Pressure
r_d	Total Pressure Recovery
r_s	Static Pressure Recovery
RMS	Root-Mean-Square

Re	Reynolds Number
T_e	Boundary Layer Edge Temperature
T_{aw}	Boundary Layer Adiabatic Wall Temperature
TSFC	Thrust Specific Fuel Consumption
U_e	Boundary Layer Edge Velocity
U_{ref}	Reference Velocity
U_∞	Freestream Velocity
U_j	Jet Exit Velocity
u_{eq}	van Driest Effective Velocity
u^*	Friction Velocity
u^+	Inner Region Scaled Velocity
$\bar{u}, \bar{v}, \bar{w}$	Mean Components of Velocity
u', v', w'	Turbulent Fluctuating Velocity Components
VGJ	Vortex Generator Jet
VR	Jet Velocity Ratio (U_j/U_∞)
x, y, z	Coordinate Directions
y^+	Inner Region Scaled Coordinate
α	VGJ Pitch Angle
B	Law of the Wall Parameter
β	Clauser's Boundary Layer Parameter, VGJ Skew Angle
δ	Boundary Layer Thickness

δ^*	Displacement Thickness
ϵ	Dissipation
γ	Ratio of Specific Heats
η_d	Diffuser Isentropic Efficiency
K	Turbulent Kinetic Energy
κ	Law of the Wall Parameter
λ	VGJ Spacing
μ	Coefficient of Viscosity
ν	Coefficient of Kinematic Viscosity
Π	Cole's Law of the Wake Parameter
ρ	Density
τ	Shear Stress

Additional Subscripts

$0, \infty$	Freestream
$1, i$	Inlet Plane
$2, e$	Exit Plane
d	Diffuser
T	Total
S	Static

Abstract

The effect of blowing vortex generator jets on the performance of a highly-offset (s-duct) diffuser was investigated experimentally. Vortex generator jets are pitched, skewed jets which generate vortices as well as injecting high-momentum fluid into the boundary layer. Diffuser performance with and without vortex generator jets was measured for an inlet Mach number of 0.6 ($Re/x = 1.2 \times 10^7$ per cm). Exit plane pressure recovery and Mach number contours were mapped using pitot and static probes. Hot wire anemometry was used to measure mean velocity components, turbulence intensity components, turbulent shear stress components, and turbulent kinetic energy at three spanwise locations on the exit plane.

Without blowing, the flow on the lower surface of the diffuser was massively separated. Blowing at 0.48% mass flow ratio through three lower surface vortex generator jets reduced the size of the separated-flow region and the exit plane boundary layer thickness, increased pressure recovery by 1.3%, and increased the static pressure rise achieved in the diffuser by over 50%. Turbulence intensity, turbulent shear stress and turbulent kinetic energy were significantly reduced by blowing. Blowing redistributed momentum within the diffuser and altered the secondary flow structure. However, flow properties were more dependent on spanwise location with blowing than without, resulting in increased distortion of the total pressure, static pressure, and flow angle fields.

PERFORMANCE CHARACTERIZATION OF A HIGHLY-OFFSET DIFFUSER WITH AND WITHOUT BLOWING VORTEX GENERATOR JETS

I. INTRODUCTION

Jet engine inlet diffuser design has become an increasingly important element in the optimization of overall aircraft propulsion system performance. In general, a diffuser is a fluid passage in which the fluid momentum decreases and pressure increases without any work being done (Hill and Peterson, 1992). A jet engine inlet diffuser delivers air from the intake to the front face of the compressor. Along its length the diffuser reduces the velocity of the air and increases its static pressure. Ideally, the diffuser would convert all of the kinetic energy removed from the air to pressure 'energy'. However, some energy is lost through the dissipative effects of viscosity. Only when the effect of viscosity is minimized can performance and efficiency be maximized.

A good diffuser design must prevent boundary layer separation, minimize total pressure loss, and deliver the air to the engine with relatively low turbulence, uniform velocity (magnitude and direction), and relatively mild pressure gradients. By definition, flow in a diffuser is subjected to an adverse axial pressure gradient. This adverse pressure gradient enhances boundary layer growth and promotes separation. A thick or separated boundary layer in the diffuser will likely produce large regions with reduced axial velocity, increased transverse velocities, and increased turbulence at the engine face. The resulting energy loss causes total pressure losses.

Frequently, it is advantageous to bury the engines in the aircraft structure. The diffuser must then turn the air while decelerating it and increasing its static pressure. Further, constraints on system weight and volume often require the diffuser to do all this in as short a length as possible. These considerations have led to the development of short

(and therefore highly divergent), highly-offset (S-duct) diffusers. The advantages of this type of diffuser may be exploited by civil transport aircraft, where the weight and volume savings can increase operating revenues, and by military combat aircraft, where reduced infra-red, radar, and acoustic signatures are also desired. Some examples of aircraft using S-duct diffusers are the Boeing 727 and Lockheed L-1011 transports, and the Northrop B-2, McDonnell Douglas F-18, and the Lockheed F-22 military aircraft.

Unfortunately, the gains in structural efficiency, weight reduction, and signature reduction achieved with short, highly-offset diffusers must be traded off against the reduced efficiency of these diffusers. Reducing the length of a diffuser induces an increase in the adverse axial pressure gradient needed to achieve equivalent diffusion, further encouraging boundary layer growth and separation. Secondary flows generated by the curvature of the duct create pressure gradients in the plane normal to the duct centerline, which cause slow-moving boundary layer fluid to be transported laterally and accumulate along the surface on the inside of the curve (Hill and Peterson, 1992). This effect thickens the boundary layer on that surface, increasing the likelihood of separation and creating more distorted conditions at the exit plane. A short, highly-offset diffuser is likely to have substantially poorer pressure recovery, higher levels of turbulence, and increased distortion at its exit plane than a straight-walled diffuser.

Diffuser losses have dramatic effects on overall propulsion system performance. For example, a one percent loss in total pressure recovery produces, roughly, a one-half percent decrease in installed engine thrust or a one-half percent increase in thrust-specific fuel consumption (TSFC). Increased levels of turbulence and distortion affect the structural integrity of the compressor as well as impacting performance. Thus, the flow peculiarities found in S-duct diffusers have a significant effect, and practical methods for boundary layer control in such diffusers warrant consideration.

Background

Three main techniques are commonly employed to minimize the dissipative effects of viscosity as a fluid flows over a body or through a duct. One approach seeks to control the boundary layer by reenergizing it with a small mass of high-momentum fluid blown through slots or jets in the wall boundary. Another uses suction to remove low-momentum boundary layer fluid from the flow through slots or a porous surface. Both of these types of boundary control are called active methods. Finally, passive devices such as vortex generators diminish boundary layer growth and discourage separation by enhancing the mixing of high-momentum fluid from the freestream with the low-momentum fluid in the boundary layer.

All of these methods have been tested extensively in straight or nearly-straight walled diffusers. Adkins (1977) provides a summary of the relative effectiveness of several boundary layer control (BLC) schemes when applied to these types of diffusers.

Blowing has several advantages over suction for application to a jet engine inlet diffuser. First, the engine is a ready source of high-pressure air to supply to the blowing jets. No energy conversion is required. Conversely, the use of suction may dictate that the engine somehow drive a suction pump to provide the pressure differential required to draw the low-momentum fluid out of the diffuser. Second, the blowing jets are less likely to become clogged by insects or other foreign particles, a problem which has been encountered by porous suction surfaces. Finally, an inlet/diffuser designed to use suction must be slightly oversized to account for the air which is captured but never reaches the engine. Blowing also offers certain advantages over solid vortex generators for this application. A solid vortex generator adds to parasite drag, cannot be turned off when it is not needed, and becomes a source for foreign object damage to the engine should it break

off in the inlet. The cost of blowing, though, is a roughly 1% increase in TSFC for each percent of inlet airflow that is bled off the compressor rather than continuing through the engine. Thus, it is important to minimize the mass flow rate requirements of any blowing boundary layer control system.

Ball (1983) and Tindell (1987) separately tested blowing and suction BLC schemes in two different highly-offset diffusers. Both studies found these methods capable of providing significant increases in diffuser performance. Tindell's results favored the use of suction as the most effective solution, with the caveat that blowing was "not done at mass flow levels sufficiently large to obtain peak performance" (Tindell, 1987:13). In this test, suction removed up to 2.5% of the diffuser throat mass flow, while the maximum blowing rate reported was approximately 1.0%. Tindell's study also investigated the effectiveness of one row of counter-rotating vortex generators, and found they "provided approximately one-half the recovery and distortion benefits achieved by the suction configuration" (Tindell, 1987:13). Ball concluded that:

Effective boundary layer control was achieved in a highly-offset diffuser with wall suction or slot blowing mass flow of approximately 2% of the primary entrance flow. It is reasonable to believe that further significant reductions in the amount of mass flow required for boundary layer control by blowing can be achieved by refinements of the blowing configuration concepts. (Ball, 1983:12)

Ball (1984) conducted a follow-on study which compared the effectiveness of seven different blowing schemes. This study showed that a combination of discrete blowing holes and solid vortex generators produced the best results, giving a total pressure recovery increase of approximately 1.0% with a blowing mass flow of only 0.4% of diffuser inlet mass flow. Thus, it appeared that some combination of high-momentum fluid injection and vortex generation held the most promise for improving the efficiency of a highly-offset diffuser while requiring a minimum expenditure of energy in return.

Vortex Generator Jets: Wallis (1952) first showed that a pitched, skewed blowing jet generates a streamwise vortex as it adds high momentum fluid to the flow. Johnston and Nishi (1989) dubbed this type of jet a 'vortex generator jet' (VGJ). They verified the existence of these vortices in a very low speed flow ($U_{ref} = 15$ m/s) and showed that these vortices are sufficiently strong, under the proper circumstances, to substantially reduce and nearly eliminate a large stalled region of turbulent separated flow over a flat plate. That study used jet-to-freestream velocity ratios near one, so the injected fluid added momentum to the flow mostly through the addition of mass.

Compton and Johnston (1991) compared the longitudinal vortex produced by a vortex generator jet to that produced by a solid vortex generator. While that study showed the vortices produced by the jets were weaker and decayed more quickly than those produced by solid vortex generators, they had an apparent advantage over solid vortex generators for inlet diffuser applications in that no core of low axial velocity was observed.

Selby et al. (1992) performed a parametric investigation to find the optimum combination of vortex generator jet geometric and flow properties to control separation on an aft-facing ramp in low speed (40 m/s) flow. This study showed the optimum inclination (pitch) angle to be between 15° and 25° relative to the surface, the optimum skew angle to be between 60° and 90° relative to the axial direction, and the optimum jet diameter to be the smallest possible, in order to maximize the jet-to-freestream velocity ratio. Velocity ratios $\left(\frac{U_j}{U_\infty}\right)$ of up to 6.8 were tested. Selby also found that VGJs retained significant separation-control effectiveness when located up to 40 boundary layer thicknesses upstream of the baseline (no blowing) separation point, but were most effective when located just upstream of the baseline separation point. Finally, the study

showed that a spanwise array of jets oriented to produce co-rotating vortices was more effective than an array of jets oriented to produce counter-rotating vortices.

Lin et al. (1992) performed a study comparing the performance of several passive and active methods for controlling separation on a similar aft-facing ramp, and found VGJs to be one of the most effective methods.

Thus, while the vortex generator jet concept has been fairly well documented, all cited studies located during a literature search were of external, incompressible, two-dimensional flows. Using VGJs for separation control in a highly-offset diffuser extended their application to a three-dimensional, compressible, internal flow regime. While the cited studies did consider turbulent flows, none investigated the effect of VGJs on turbulence levels by measuring turbulent flow properties with and without the VGJs operating, as was done in this study.

Objective

The objective of the research documented in this thesis report was to evaluate the effect of vortex generator jets on the performance of a representative short, highly-offset diffuser. Diffuser performance was quantified by measuring a number of properties of both the mean and turbulent flows at the diffuser exit plane with and without blowing vortex generator jets. This data could also be used as a check case for CFD models of geometrically-similar diffuser designs.

Outline

The chapters which follow detail the work performed to achieve the objective stated above. Chapter 2 discusses some of the flow phenomenon relevant to the problem

of boundary layer control in a highly-offset diffuser, surveys the results of previous experimental and numerical experiments, and introduces the measures used to quantify diffuser performance. Chapter 3 details the test facility, model, instrumentation, procedure, and conditions. Chapter 4 presents and interprets the results of the experiment. Finally, Chapter 5 summarizes the conclusions made from data and suggests areas for further study.

II. THEORY

Several aspects of the flow in a highly-offset diffuser make it difficult to analytically predict the flow behavior. The axial turning of the flow generates secondary flows, which make the motion three-dimensional. At typical operating conditions, the flow will almost certainly be turbulent and compressible. The adverse axial pressure gradient promotes rapid boundary layer growth and increases the likelihood of boundary layer separation. Analysis of a compressible, turbulent, three-dimensional flow in an adverse pressure gradient with a high probability of separation is no simple task.

Many researchers have modeled the flow in an S-duct using computational fluid dynamics (Ball, 1984; Tindell, 1987; Neumann et al., 1980; Fiedler and Gessner, 1972; Smith et al., 1992, and others). Indeed, numerical methods are the only non-empirical means to obtain a reasonably accurate analytical approximation of this flow. Though the development of a valid numerical solution for the flow inside the highly-offset diffuser tested experimentally was beyond the scope of this research program, insights provided by earlier numerical studies of similar geometries aided the interpretation of experimental data. The following discussion is limited to a qualitative discussion of the flow phenomenon expected to occur in the diffuser, definition of the performance parameters and flow properties measured experimentally, and a brief summary of the types and accuracies of CFD solutions obtained by others for similar flow problems.

Coordinate System

The physical description of boundary layer phenomenon which follows uses a coordinate system which is less precisely defined than the coordinates used to define the model geometry and reference test data. For the first part of this chapter, the x-direction points downstream, the y-direction points into the flow normal to a boundary, and the z-direction is defined by the right-hand rule. When these coordinates are applied to the specific geometry of the test diffuser, the origin is fixed at the left-hand lower corner of the diffuser entrance plane when looking downstream. Figure 1 shows the orthogonal coordinate system in reference to the diffuser.

Boundary Layer Growth, Transition, and Turbulence

In the flow of fluids of small viscosity, the influence of viscosity is confined to a thin layer adjacent to a boundary (Prandtl, 1904). The boundary layer thickens along a surface as the effect of viscosity propagates outward from the boundary while the flow moves downstream. The growth of a boundary layer along a solid wall is characterized by three flow regimes: an initial laminar region, a transition region, and a turbulent region. The boundary layers inside the diffuser were expected to be fully turbulent, since the inlet length was relatively long and the freestream was expected to contain a small level of turbulence.

Figure 2 shows a typical laminar boundary-layer profile, as determined by the Blasius solution of the Navier-Stokes equations, and a typical turbulent boundary-layer profile using Prandtl's $1/n$ power approximation with $n = 7$ (Hill and Peterson, 1992:100). The turbulent profile approximation is based solely on experimental results, and $n = 8$ has been found to fit the data better for high Re_x flows (Schetz, 1993), such as existed inside the test diffuser. The turbulent boundary layer is fuller but thicker than the laminar boundary layer because turbulent eddies facilitate the transfer of mass, momentum, and energy across the boundary layer (White, 1991).

Fluid motion in the turbulent boundary layer is disorderly and the instantaneous fluid velocity at a point varies significantly from the bulk (mean) values which would be calculated from a simple control volume analysis. In turbulent flows, the flow properties are usually modeled as the sum of a mean component, which reflects the overall bulk motion of the fluid, and a fluctuation component, which reflects the random variation of the property about its mean value. For example,

$$u = \bar{u} + u'$$

where the overbar represents the mean component and the primed term represents the fluctuation component. The time average of the fluctuation component is zero. However, even when the mean term is zero for a certain property (for example, \bar{w} in a two-dimensional mean flow), the instantaneous value of the associated fluctuation component need not be negligible ($w' \neq 0$). Thus, turbulent flows are inherently three-dimensional.

When these new representations of the fluid properties are inserted into the Navier-Stokes equations, using the concept of Reynolds averaging, the fluctuation components now appear in the equations of motion as additional shear stress components:

$$\tau_x = \mu \frac{\partial \bar{u}}{\partial y} - \rho \bar{u'^2} - \rho \bar{u'v'} - \rho \bar{u'w'} \quad (1)$$

When $u = \bar{u}$, the first term on the right-hand side of (1) is the usual definition for fluid shear stress. The additional terms on the right-hand side of (1) are referred to as the turbulent, or Reynolds, shear stresses (Schlichting, 1951). They greatly complicate the solution of Navier-Stokes equations for turbulent flow, since the inclusion of the fluctuation velocity components raises the number of unknowns without adding additional equations. These terms are typically modeled by semi-empirical relationships.

The situation becomes even more complicated when the mean flow is fully three-dimensional. Near separation, the component of velocity in the nominal streamwise direction may no longer be dominant. It is not rigorous to assume that some of the velocity fluctuation terms are negligible when compared to the others. All of the components of the turbulent shear stress must be considered. Flow at the exit plane of the highly-offset diffuser was expected to be three-dimensional, due to the presence of secondary flows and separation.

While the disturbance velocities in a turbulent boundary layer are very difficult to predict, the mean component can be described quite well. Evaluation of experimental data led to the division of the turbulent boundary layer into three distinct regions. In the outer region of the boundary layer, far from the wall, the velocity deficit $u - U_e$ collapses to

become a function of y/δ when it is scaled by a factor proportional to the square root of the coefficient of friction, C_f . The friction velocity u^* is defined as such a scale:

$$u^* = \left(\frac{\tau_w}{\rho} \right)^{1/2} \quad \text{or} \quad \frac{u^*}{U_e} = \left(\frac{C_f}{2} \right)^{1/2}$$

At the wall, $u' = v' = w' = 0$ due to the no-slip boundary condition. In the inner region nearest the wall, the presence of the boundary damps out the velocity fluctuations and the flow there is laminar. The velocity is a function of the distance from the wall in this laminar sublayer. It can be scaled to give:

$$u^+ = \frac{\bar{u}}{u^*} = y^+$$

y^+ is a Reynolds Number-like parameter resulting from the scaling of y by u^* :

$$y^+ = \frac{yu^*}{v}$$

In the overlap between these regions, a logarithmic function matches the different functional relationships in the inner and outer layers:

$$u^+ = \frac{1}{\kappa} \ln y^+ + B \quad \text{where } \kappa = 0.40 \text{ and } B = 5.0.$$

The outer region is also well described by the logarithmic law above, with the addition of Coles' wake parameter:

$$u^+ = \frac{1}{\kappa} \ln y^+ + B + \frac{2\Pi}{\kappa} \left(3 \left(\frac{y}{\delta} \right)^2 - 2 \left(\frac{y}{\delta} \right)^3 \right)$$

Π is an empirically-determined function of Clauser's parameter $\beta = \frac{\delta^*}{\tau_w} \frac{dP_e}{dx}$ and can be

determined from Figure 3 (White, 1991:452).

Collectively, these relationships for the inner, overlap, and outer regions are known as the law of the wall. Figure 4 (Schetz, 1993:209) shows a plot of the law of the wall for zero pressure gradient. Especially noteworthy is the small extent of the laminar sublayer. The formulation of the law of the wall for compressible flows is similar, but u^+ is replaced by u_{eq} . The equivalent velocity u_{eq} relates to the mean velocity component \bar{u} through a function which accounts for the effects of wall heat transfer and variable density. For the case of adiabatic walls, applicable to the test diffuser, the relationship is (White, 1991):

$$u_{eq} = \frac{U_e}{a} \sin^{-1} \left(\frac{a\bar{u}}{U_e} \right) \quad \text{with} \quad a^2 = 1 - \frac{T_e}{T_{aw}} .$$

To transform the law of the wall to the familiar scaled variables y/δ and u/U_e , it is necessary to estimate C_f so u^* can be evaluated. White (1991:430) recommends the following approximation:

$$C_f \approx 0.020 \text{ } Re_\delta^{1/2}$$

Fluctuation velocity components can be measured by devices with a high frequency response, such as a hot wire anemometer. Specifying the value of a disturbance quantity at one instant in time does not provide useful information, as the quantity varies at random. The time average of a fluctuation quantity is zero, since it is defined as the

deviation from the mean value. Fluctuation velocities are most useful when given as an RMS value, defined as:

$$u'_{rms} = \sqrt{\frac{1}{N-1} \sum_1^N (u - \bar{u})^2}$$

where $(u - \bar{u}) = u'$ and N is the number of sample points. Disturbance velocity measurements are usually nondimensionalized by the local mean velocity, \bar{u} , or the freestream velocity U. When nondimensionalized in this way, the quantities

$\frac{u'_{rms}}{\bar{u}}$ or $\frac{u'_{rms}}{U}$ are called turbulence intensities. They reflect the magnitude of the velocity fluctuation relative to the mean velocity.

Another useful way of representing the magnitude of the turbulence in a flow is through the turbulent kinetic energy, defined as:

$$K = \frac{1}{2}(\bar{u}'\bar{u}' + \bar{v}'\bar{v}' + \bar{w}'\bar{w}')$$

Turbulent kinetic energy is a measure of the energy stored in the turbulent motion. In a typical boundary layer without work interactions, conservation of energy dictates that an equivalent amount of energy must be lost from the freestream. In this way, turbulence contributes to the total pressure losses in the diffuser. When K is nondimensionalized by \bar{u}^2 , it represents the ratio of the kinetic energy held in the turbulent motion to the kinetic energy in the mean flow. Likewise, nondimensionalizing by U_∞^2 produces the ratio of turbulent energy to the energy initially in the flow.

Adverse Pressure Gradients, Secondary Flows, and Separation

Flow in a diffuser by definition encounters an adverse pressure gradient - an increase in pressure in the streamwise direction. As no work is done on an element of the fluid, only its momentum and the viscous shear stress applied to it by adjacent faster-moving elements keep it moving into the region of increased pressure. Skin friction and the retarding shear stress applied by slower-moving elements work to restrain the flow as well.

Boundary layer fluid has less momentum than the freestream due to its reduced velocity; eventually, the sum of the momentum and the propelling viscous force is not sufficient to overcome the resisting forces of pressure and skin friction, and the element of fluid cannot flow any farther (Kline, 1967). This typically occurs first along the solid boundary, since the fluid there has the lowest momentum. A stagnation line forms in the fluid itself; the streamlines nearest the wall must separate from the wall to follow the stagnation line. Recirculating eddies and reverse flow occur in the region downstream of the stagnation line, though often the flow rebalances and the pressure gradient downstream of the separation point goes to zero, leaving nothing to drive the reversed flow (Hill and Peterson, 1992). Figure 5 shows the stages of boundary layer growth leading up to separation of a two-dimensional flow; near separation the boundary layer profile takes on inflectional shape characteristic of boundary layer flow in a strong adverse pressure gradient (Schlichting, 1951). In a steady flow, the point where the streamline

leaves the wall to follow the stagnation line in the fluid is called the separation point. At the separation point, the flow near the wall is stagnant, thus $\frac{\partial u}{\partial y}$ is locally zero.

Three dimensional separation is more difficult to visualize, since the low momentum fluid now has the freedom to displace in the spanwise direction. Lines of separation are defined as lines that the surface streamlines approach but do not cross. Saddle points form where surface streamlines turn away from each other, while nodes form where they come together to a point. Focus points occur in pairs; they are a special type of node where the streamlines follow a spiral path to convergence, similar to a superimposed sink and vortex in potential flow. The two-dimensional picture of separation is more easily visualized, and, for a diffuser where the axial pressure gradient is expected to be nearly constant in the spanwise direction, it may be sufficient.

A separated flow may reattach to the wall if the adverse pressure gradient diminishes or if the geometry directs the flow back to the wall.

The S-duct diffuser experiences another phenomenon which accelerates boundary layer growth and separation along the surface on the inside of each bend. Along the outside of the bend, the flow experiences a local compression, resulting in a decrease in velocity and an increase in pressure. Along the inside of the bend, the effect is reversed and the flow senses a local expansion, with the resulting increase in velocity and decrease in pressure. This establishes a pressure gradient normal to the streamwise direction. Turning of the flow also generates centrifugal forces which tend to carry the high momentum fluid to the outside of the bend. The boundary layer fluid there has less

momentum attempting to carry it along in the initial flow direction, so it is more easily displaced. The high-momentum fluid moving to the outside of the turn displaces the low-momentum fluid, which then follows the transverse pressure gradient to the nearest sidewall and then around to the inside of the turn. A significant three-dimensional secondary flow is established. In a turbulent boundary layer the streamlines nearest the wall can be deflected up to 30° degrees away from the axial direction in this manner (Prandtl, 1952).

Along the surface at the inside of the bend, secondary streams of low-momentum fluid from each sidewall converge and accumulate. They meet near the centerline and tend to roll up into two counterrotating, spanwise vortices (Bansod and Bradshaw, 1972). These vortices act to lift the low-momentum fluid away from the lower surface, further promoting boundary layer growth and separation. In an S-duct diffuser, this effect is most pronounced just downstream of the first bend. The effect at the second bend is similar, but since the second bend is usually near the end of the diffuser, the adverse pressure gradient typically does not persist a significant distance downstream of this bend.

Separation is the worst-case flow condition a subsonic diffuser might encounter. Large quantities of energy are consumed by the turbulent recirculating eddies which form in the separated region. Within that region, the fluid has essentially no momentum in the nominal downstream direction. The separated-flow region effectively blocks part of the cross-sectional area of the duct, reducing the effective area ratio and decreasing the amount of diffusion achieved. Aft of the reattachment point, the separated flow region trails a turbulent, low-momentum wake. Skin friction and pressure drag are increased.

All of these loss mechanisms combine to decrease the efficiency of the flow process occurring within the diffuser.

Vortex Generator Jet Theory

The use of either blowing or vortex generation for control of boundary layer separation in a diffuser is not new (Adkins, 1977, Nicoll and Ramaprian., 1970, Fielder and Gessner, 1972). Streamwise blowing adds high-momentum fluid to the boundary layer, allowing the boundary layer to penetrate farther against the adverse pressure gradient. Vortex generators control separation by enhancing the mixing of boundary layer and freestream fluid. The vortex generator jet is a device which performs both of these functions.

While it has been well documented that a pitched and skewed jet generates a longitudinal (streamwise) vortex (Wallis, 1952; Johnston and Niishi, 1989; Compton and Johnston, 1991), little is known about the physical mechanism behind this (Compton and Johnston, 1991). A numerical study by Zhang and Collins (1993) solved the mass-averaged Navier-Stokes equations with a k- ϵ turbulence model for flow over a flat plate containing a VGJ using a 50 x 28 x 42 mesh. Their results suggested that the jet actually generates two counter-rotating vortices. These are apparently caused by viscous entrainment of the boundary layer fluid adjacent to the jet and the consequent motion induced in the rest of the flow to satisfy conservation of mass. One, on the freestream side of the jet (oblique angle between jet and surface when viewed in the streamwise direction),

is dominant (Figure 6). The other, on the wall side of the jet, is pinched between the jet and the surface. It is considerably weaker, and the dominant vortex engulfs it within two to five jet diameters downstream. The strong single vortex which remains moves laterally in the direction of the jet stream as it moves downstream, and persists for more than 40 jet diameters.

The same study evaluated the effects of jet velocity ratio and skew angle on vortex production and downstream skin friction coefficient. This information, along with information presented by Selby et al. (1992), Compton and Johnston (1991), and Johnston and Nishi (1989), was used to choose the VGJ configuration tested in this research program. Five parameters specify a VGJ configuration: velocity ratio, pitch angle, skew angle, spanwise spacing, and longitudinal location of the jets. The paragraphs that follow summarize the available information on the influence of each parameter and give the values chosen during this study.

Velocity Ratio (VR). The jet velocity ratio is defined as:

$$VR = \frac{U_j}{U_\infty}$$

While the studies of Johnston and Niishi and Compton and Johnston showed VGJs were effective with VR near 1.0, the results of Zhang and Collins and Selby et al. indicated that a higher velocity ratio was more effective. Zhang and Collins showed that, for $0.0 < VR < 1.2$, the jet did not penetrate far into the flow and the resulting vortex was imbedded in the boundary layer. In such instances, the vortex dissipated rather quickly and did not convect much kinetic energy across the boundary layer. For $1.2 < VR < 2.5$, the jet penetrated

farther into the flow and the vortex lay in the outer region of the boundary layer. Mixing of the freestream and the boundary layer occurred readily. For $2.5 < VR$, the jet penetrated deep into the freestream and the vortex lay outside the boundary layer. At this condition, the vortex persisted far downstream but was too far from the wall to significantly affect the boundary layer profile.

Data from the aft-facing ramp separation control experiment of Selby et al. showed VGJ effectiveness increased with increasing VR, all the way to $VR = 6.8$. It seems that the thickness of the upstream boundary layer and the pressure of the fluid in the jet would affect the penetration distance. Unfortunately, Zhang and Collins did not provide data for these factors. The experiment of Selby et al. was judged to be most similar to the present study, as it incorporated surface curvature, an adverse pressure gradient, and a near-separation flow. It was decided, then, to maximize VR subject to manufacturing and facility constraints. For choked flow with friction through the smallest obtainable jet diameter at the highest allowable blowing plenum pressure, the calculated velocity ratio was 1.57.

Pitch Angle (α). Only Selby et al. examined the influence of pitch angle. That test revealed that a value of about 25° gave the best pressure recovery, with effectiveness decreasing gradually as the angle was increased or decreased. Lower pitch angles imparted a greater spanwise velocity component to the fluid on the surface after reattachment. A pitch angle of 25° was selected for this study.

Skew Angle (β). Compton and Johnston found that a spanwise angle between 45° and 90° produced the maximum secondary velocities and axial vorticity, though the

effect at 45° was just slightly improved over the 90° case. Zhang and Collins confirmed this result, showing a rapid increase in the viscous skin friction coefficient between 0° and 45° , and only a slight change above 45° . Selby et al. found that maximum pressure recovery occurred between $\beta = 60^\circ$ and $\beta = 90^\circ$. Based on all three sets of data, a skew angle of 60° was initially chosen for this program, though it had to be reduced to 45° because of manufacturing limitations.

Jet Spacing (λ) and Relative Orientation. The vorticity field generated by one VGJ affects a limited spanwise extent of the flow. A spanwise array of VGJs, then, may be necessary to control the boundary layer over a large-span flow. No study has yet evaluated the effect of spanwise spacing on the effectiveness of an array of VGJs. Only Selby et al. and Johnston and Niishi used arrays of VGJs in their experiments. Johnston and Niishi's VGJs were spaced at $\lambda/d = 7$; the resulting data showed large spanwise regions at downstream planes where the jets had little effect. The VGJs employed by Selby et al. were spaced at $\lambda/d = 0.9$, and the results showed a relatively uniform spanwise effect. Thus, the spanwise spacing between jets for this experiment was intended to be about $\lambda/d = 1.0$, though precise determination was not possible because the boundary layer thickness at the jet location was not known.

In an attempt to generate counterrotating vortices, both Johnston and Niishi and Selby et al. examined configurations where the skew angle for adjacent jets alternated in sign. This approach was generally less effective than spanwise arrays where all jets had the same orientation, so the latter arrangement was used in the current study.

Location. Only Selby et al. examined the effect of jet axial location relative to the reference separation point. These results showed that the effectiveness varied little for jets located within 10δ of the reference separation point, and that significant improvements in C_p were achieved with wall jets located up to 40δ upstream of separation. With this data in mind, the jets were located in the test diffuser approximately 2δ to 4δ upstream of separation - as far upstream as could be practically implemented due to the location of the separation point and the small scale of the model. Again the lack of knowledge of the boundary layer thickness at the jet location made exact determination impossible.

Diffuser Performance Criteria

Several measures are commonly used to quantify the performance of a subsonic diffuser. They are useful for comparing the performance of one diffuser configuration to another. In this study, four parameters were used to characterize the performance of the test diffuser with and without vortex generator jets: static pressure coefficient, total pressure recovery, isentropic efficiency, and distortion. Taken together, these measures indicate how well the diffuser achieved the desired flow qualities introduced in Chapter 1.

Pressure Coefficient. The pressure coefficient, C_p , is a nondimensional measure of the static pressure rise in a diffuser, and as such is a valuable parameter for comparing the performance of different diffuser configurations. The pressure rise in a subsonic diffuser is accomplished mostly by the change in flowpath area between the entrance and the exit.

When the flow separates, the stagnation line becomes a new boundary for the

throughflow, effectively reducing the flowpath area. Thus, separation reduces the pressure rise achieved in the diffuser. Analysis of test data for this experiment used the definition of C_p for a diffuser with mass addition introduced by Nicoll and Ramaprian (1970):

$$C_p = \frac{(\dot{m}_d + \dot{m}_j) \Delta p}{\dot{m}_d \left(\frac{1}{2} \rho U_0^2 \right) + \dot{m}_j \left(\frac{1}{2} \rho U_j^2 \right)} \quad (2)$$

Equation 10 reduces to the familiar definition of C_p when $\dot{m}_j = 0$.

Pressure Recovery. The diffuser performance parameter most useful and familiar to propulsion system designers is pressure recovery, r_d . Pressure recovery is defined by

$$r_d = \frac{P_{T3}}{P_{T0}}$$

where P_{T3} is the total pressure at the diffuser exit, and P_{T0} is the freestream total pressure upstream of the diffuser entry. For an ideal, no-loss diffusion process, $r_d = 1$. Actual values of r_d , then, reflect the magnitude of the losses incurred in the flow process.

The face-averaged pressure recovery is the area-weighted average of all the total pressure recovery measurements taken across the diffuser exit plane. For the purpose of comparing different configurations of the same diffuser, the exact area-weighting scheme is not important so long as it is used consistently. For this study, then, each measured value of pressure recovery was weighted equally though the measurement stations near the

diffuser surfaces did not encompass the same area fraction as those stations located away from the walls.

In order to nondimensionalize static pressure measurements, static pressure recovery was defined as:

$$r_s = \frac{p_s}{p_{T0}}$$

Face-averaged static pressure recovery was calculated like the face-averaged total pressure recovery.

Isentropic Efficiency. The isentropic diffuser efficiency, η_d , as derived through a one-dimensional flow, perfect gas analysis is given by:

$$\eta_d = \frac{\left(1 + \frac{\gamma - 1}{2} M^2\right) (r_d)^{\frac{\gamma-1}{\gamma}} - 1}{\left[\frac{(\gamma - 1)}{2}\right] M^2} \quad (3)$$

which can be adopted to a three-dimensional flow by using the face-averaged value for r_d .

Distortion. Uniform flow is desired at the exit plane of a jet engine inlet diffuser, for then the loading of a compressor blade does not change as it rotates around the hub. Distortion of the pressure field decreases engine stall margin and causes cyclical loading and unloading of the compressor, leading to fatigue. Several methods of quantifying the deviation of the exit plane total pressure pattern from uniform have been developed. Two were used in this study.

Maximum/Minimum Method Distortion. This method is a percentage measure of how much the recovery at a point on the exit plane might differ from the face-averaged value (Mattingly et al., 1987:358). It is defined as:

$$D_{\min/\max} = \frac{(r_d)_{\max} - (r_d)_{\min}}{(r_d)_{\text{avg}}} \quad (4).$$

A high value of $D_{\min/\max}$ means that local values of pressure recovery deviate significantly from the face-average value. Max/min distortion gives no insight about the magnitude of the transverse pressure gradients existing on the exit plane.

Maximum Gradient Method Distortion. The maximum gradient method distortion is defined here as the maximum difference in measured pressure recovery between two adjacent measurement stations:

$$D_{\max \text{gradient}} = \max(r_{i \pm 1,j} - r_{i,j}) \text{ or } \max(r_{i,j \pm 1} - r_{i,j}) \quad (5).$$

In essence, this parameter is a measure of the spacing between contours of constant total pressure recovery. A high value of $D_{\max \text{gradient}}$ means that large gradients exist in the total pressure field at the exit plane, and contours would fall close together. As is, this method is not useful for comparison to test data from other facilities because the values calculated depend on the spacing between measurement stations and the scale of the model. Perhaps a better formulation would divide the difference above by the spacing between stations nondimensionalized by some characteristic dimension of the exit plane.

Turbulence. While not specifically defined as diffuser performance parameters, turbulence intensity, turbulent kinetic energy, and turbulent shear stress can all be used as indicators of the general character of the flow in the diffuser. Turbulence intensity

measurements quantify the level of turbulence present in the flow; a low level of turbulence is desirable at the diffuser exit. Turbulent kinetic energy and turbulent shear stress quantify mean flow energy losses to the turbulent motion. Those quantities, then, are relative indicators of the efficiency of the overall flow process

Summary of Related Numerical Work

Several researchers have modeled the flow in highly-offset diffusers using computational fluid dynamics (CFD). While all surveyed results fail to fully resolve the separated regions of the flowfield, a great deal of insight into the gross features of the flow may be garnered from their work. Further, a survey of this literature provided a basis for identifying the types of experimental measurements deemed most useful to the numerical analyst.

In the early 1970's, Fiedler Gessner (1972) and Nicoll and Ramaprian (1970) computed the flowfield inside a two-dimensional straight-walled diffuser using a finite difference approach. Nicoll obtained fairly good agreement with experiment for C_p upstream of separation, while Fiedler was able to accurately model the influence of tangential blowing measured by experiment. In 1980, Neumann et al. modeled the HiMAT S-duct diffuser as a segment of an annular diffuser. Centerline geometry and overall area ratio were modeled, but no attempt was made to model the axial variation of cross-section area or shape. Even with these simplifications, the method predicted separation, and gave a reasonable approximation for the exit plane total pressure and wall

static pressure distributions measured experimentally. These results suggest that qualitatively accurate results could be obtained by two-dimensional CFD analysis.

In the 1980's, several three-dimensional solutions for highly-offset diffusers were published. Ball (1983, 1986) used a two-dimensional boundary layer code to predict separation point location, and a three-dimensional potential flow (inviscid) code to predict the ideal axial static pressure distribution. Tindell (1987) used a subsonic low-order panel method to predict axial static pressure variation and separation point location. It produced results which, in his words, were "well suited to preliminary design applications." For detailed internal flowfield analysis, Tindell solved the three-dimensional Navier-Stokes equations. This solution predicted separation and the formation of counter-rotating streamwise vortices, but did not accurately model the total pressure distribution in the lower section of the duct, aft of the separated flow region. Vakili et al. (1984) compared the results obtained using a three-dimensional, turbulent, compressible Parabolized Navier- Stokes solver to experimental data. The CFD solution showed the presence of the streamwise vortices embedded in the flow, but underpredicted the flow distortion resulting from the secondary flows. Anderson and Gibb (1992) used a three-dimensional Reduced Navier-Stokes code to model the influence of vortex generators inside an S-duct.

Finally, in what is at the time of this publication likely the most current published work in the area, Smith et al. (1992) evaluated the ability of the three-dimensional Full Navier Stokes code PARC3D to model the flow in a subsonic compressible S-duct diffuser. The model used the Baldwin-Lomax turbulence model on two grids: a 75 x 33 x

33 H-grid or a $65 \times 49 \times 26$ O-grid. Results were compared to the experimental data of Vakili (1987). Separation was predicted, though the predicted separation point was 1/2 duct diameters farther downstream than seen in the experiment. Predicted static pressure contours were in poor agreement with the experimental data, especially downstream of separation. The magnitude of the static pressure was consistently over-predicted. Total pressure contours, on the other hand, agreed quite well with the experiment, though accuracy worsened as the flow progressed downstream. Their simulation underestimated the magnitude of the secondary flows, though the orientation of the velocity vectors was qualitatively similar to the experimental data. Predicted boundary layer growth was also qualitatively accurate but reflected the under-prediction of the secondary flows.

One common thread tied together most of the reports on CFD simulations of S-duct flows. Nearly every author recognized the need for improved turbulence models, and the need for more compressible-flow data for highly-offset diffusers in order to better evaluate the accuracy of CFD solutions.

III. TEST APPARATUS, INSTRUMENTATION, AND PROCEDURE

Tests conducted during this program used a subscale rectangular cross-section diffuser installed in the AFIT Subsonic Diffuser Test Facility, Area B, Building 640, Room 148, Wright-Patterson AFB, OH. As configured for this study, the facility allowed testing at Mach numbers up to 0.79 and freestream $\frac{Re}{x}$ of approximately 1.2×10^7 per centimeter.

A rectangular cross-section was chosen because it was the simplest to build and instrument. Ball (1983) found that data from a rectangular cross-section diffuser demonstrated the same general trends as that from a more representative round cross-section duct, so it was deemed suitable for the investigative nature of this study.

Facility

The AFIT Subsonic Diffuser Test Facility (Figure 7) used a multi-purpose compressed air supply source. Two Atlas-Copco GAU-08 compressors located in the basement of Building 640 supplied 0.45 kg/sec of air at a nominal pressure of 687 KPa (100 psi). Each compressor passed its output air through a Pioneer model R500A refrigeration-type air dryer before entering the building compressed air storage/supply system. Air was delivered to Room 148, roughly 150 meters away, through 7.62 cm (3 inch) iron pipe. Once in the room, the air passed through a shutoff valve, a centrifugal moisture and particle separator, and a 20.32 cm (8 in) diameter filament-reinforced paper filter before reaching a solenoid-controlled pneumatically-actuated shutoff valve. The air

then flowed through approximately 5 m of heavy-duty flexible hose to reach a Leslie pressure-regulating valve. This gate-type valve used feedback delivered by a small neoprene hose from the settling chamber just upstream of the test section to regulate the pressure to the value set on a Fairchild Instruments control regulator. After exiting this valve, the air passed through two 90° bends, a 45° bend, a final shutoff valve, and another 90° bend, each separated by short lengths of 5.08 cm (2 in) iron pipe, before entering the straight section which led to the test section.

The flow system immediately upstream of the test apparatus consisted of 1.85 m (73 in) of 5.08 cm (2 in) iron pipe, a 5.08 cm long expansion to 7.62 cm (3 in) diameter, a 15.24 cm (6 in) length of 7.62 cm diameter iron pipe which served as a settling chamber, a 10.16 cm (4 in) long contraction/transition section which transformed the flowpath to a 2.54 cm x 1.679 cm rectangle, and a 15.24 cm (6 in) long inlet tube. The test section bolted to the end of the inlet tube.

A flow straightener was installed in the 7.62 cm (3 in) diameter settling chamber. It consisted of 6.35 cm (2.5 in) of 0.635 cm (0.25 in) element stainless steel honeycomb sandwiched between layers of fine mesh screen. The settling chamber held approximately 6.95×10^{-4} m³ of fluid. The flow velocity here was estimated at 20 m/s, or about M = 0.05. A K-type thermocouple inserted into the settling chamber measured the approximate stagnation temperature. Its output was read off a QE Omega Model 400B1A-0JC Digicator™ indicator, accurate to ± 1.0 K. A Matheson PN 63-3112 0 - 687 KPa gage (0 - 100 psig) analog pressure gage fitted to the settling chamber was used for

quick reference when setting test conditions, but was not used for data acquisition or analysis.

The contracting round-to-rectangular transition section was specially designed and fabricated for this program. The contraction was accomplished in 7.62 cm (3 in) length. The contraction ratio was 10.7:1. The wall contours followed parabolic arcs. This section was machined from aluminum in halves by the AFIT model shop using a CNC mill. Though the internal surfaces were polished, the seam between the halves was barely perceptible to touch when they were mated together.

The inlet tube consisted of a 13.97 cm (5.5 in) length of rectangular cross-section tube constructed from four pieces of 0.635 cm (0.25 in) thick aluminum plate fastened together by small bolts. A 0.635 cm thick mating flange was bolted to each end. The butt joints between the tube section and the flanges were not airtight, particularly at the downstream end. Modeling clay was used to eliminate some of the leakage, but an airtight seal could not be attained due to the high pressures and the thinness of the aluminum plate. Additionally, there was some play in the alignment of the flowpath openings in the flanges with the tube section. Extreme care was necessary to obtain a satisfactory fit and minimize the height of any forward- or aft-facing steps which might be created.

Downstream of the test section, the flow passed through a variable-throat area diffuser used to control mass flow and test section Mach Number. The converging section began 11.43 cm (4.5 in) downstream of the test section exit (16.51 cm downstream of the diffuser exit plane), and continued to the throat location, 15.24 cm (6 in) further downstream. The flexible upper flowpath surface was positioned by a crank attached to a

fine screw threaded through the fixed upper surface. After passing through the throat, the air was gradually expanded and dumped into the room through a 2.54 cm x 5.08 cm (1 in x 2 in) nozzle. Figure 8 shows the test section installed in the facility.

When the vortex generator jets were installed, a neoprene tube delivered high pressure air taken from between the particle separator and the filter to the blowing plenum. An Airco pressure regulator on the neoprene tube controlled the pressure in the plenum.

Test Diffuser Geometry

Figure 9 shows the diffuser flowpath. The diffuser flow passages were sized to allow continuous operation at 515 KPa (75 psi) gage supply pressure with an airflow of 0.45 kg/s - nearly the full capacity of the air supply system. After oversizing by 15% to account for blockage by the boundary layer and losses in the flow straightener, the required throat size was determined to be $4.2886 \times 10^{-4} \text{ m}^2$ (0.661 sq in). This allowed near-choked flow at the diffuser entry, simulating high-subsonic speed flight. Achieving typical engine inlet diffuser exit conditions of $M = 0.4$ to $M = 0.5$, required an area ratio $A_e/A_i = 1.5$; so the exit plane area was $A_e = 6.4329 \times 10^{-4} \text{ m}^2$ (1.0 sq in). The dimensions of the exit plane were then set to 2.54 cm x 2.54 cm (1 in x 1 in) to give a square cross-section. For reference to circular cross-section diffusers, the equivalent diameter, equal to that of a circle with the same cross-section area, was $D_{eq} = 2.882 \text{ cm}$ (1.135 in). To

maintain constant width throughout the diffuser, the inlet plane dimensions were then 2.54 cm x 1.679 cm (1 in x 0.661 in).

Two other geometric parameters are needed to define the basic geometry of a highly-offset diffuser. The length parameter L/D_{eq} specifies the axial distance over which the diffusion must occur, and, along with the area ratio, determines the axial pressure gradient. The centerline offset parameter $\Delta y/D_{eq}$ is an indirect measure of the curvature required, which determines the strength of the secondary flows produced. Values for these parameters were selected to represent a highly-offset diffuser configuration tested extensively by McDonnell Aircraft Company during the USAF Wright Aeronautical Laboratories Subsonic Diffusers for Highly Survivable Aircraft program (Lee and Price, 1986). Table 1 summarizes the key geometric parameters of the test diffuser:

Table 1
Test Diffuser Geometric Reference Values

D_{eq}	2.882 cm
A_e/A_i	1.51
L/D_{eq}	2.07
$\Delta y/D_{eq}$	0.81

The cross-section area variation and the centerline shape must be defined to complete the diffuser design. The cross-section area of the test diffuser increased linearly from the beginning of the divergence until the exit area was achieved. The centerline curvature was determined by a third-order curve fit:

$$\frac{y}{h_e} = -0.142253\left(\frac{x}{h_e}\right)^3 + 0.501307\left(\frac{x}{h_e}\right)^2 - 0.00098192\left(\frac{x}{h_e}\right)$$

where h_e is the height of the diffuser flowpath at the exit plane. Closely grouped clusters of points were used to constrain the centerline to zero slope at the entrance and exit planes.

The AFIT model shop machined the curved upper and lower surfaces (Figure 10) from aluminum block using a CNC mill. Three identical lower surfaces and two identical upper surfaces were produced. These sections were machined with 5.08 cm (2 inches) of straight wall upstream and downstream of the curved diffusing section. Flowpath surfaces were polished until smooth to the touch. Sideplate frames were fabricated from 2.54 cm (1 in) thick aluminum with 2.286 (0.90 in) thick Plexiglas inserts to allow viewing of the internal flowpath. Silicone RTV sealed the Plexiglas into the frames to prevent leakage. All mating surfaces were fitted with rubber O-rings for an airtight seal. The entire diffuser test section was bolted together with 10/32 Allen head bolts spaced approximately 3.175 cm apart around the perimeter. Table 2 gives the dimensions of the test section:

Table 2

Test Section Dimensions

Dimension	cm (in)
Overall Length	16.129 (6.35)
Length of Diffusing Section	5.969 (2.35)
Centerline Offset	2.334 (0.919)
Inlet Height	1.679 (0.661)
Exit Height	2.54 (1.0)
Width (constant)	2.54 (1.0)

Figure 11 shows the assembled test section.

A spanwise array of three vortex generator jets were installed in one of the lower surfaces. The jets were constructed by drilling oversized pitched and skewed holes into the flowpath surface, then inserting 0.0572 cm (0.0225 in) inner diameter thin-wall tubing through the holes. The tubes were filed and sanded until flush with the surface of the diffuser. Small gouges left by the drill were filled with epoxy and sanded until smooth. The jet exit plane was located 1.27 cm (0.5 in) downstream of the beginning of the curved, diffusing passage, or 6.35 cm (2.5 in) downstream of the beginning of the test section. At this location, the tangent to the lower surface formed an angle of -25° with the x-axis in the xy-plane, so that when the jets were pitched at 25° they blew along the x-axis. The

jets were canted 45° in the direction of decreasing z, so that they blew towards the left sidewall when looking downstream. A plenum milled into the underside of the lower surface held high-pressure air for the jets. The perimeter of the plenum was sealed with rubber O-rings and silicone RTV. The passage connecting each jet exit with the plenum was 0.762 cm (0.3 in) long.

Measurement Planes and Instrumentation

Measurement Planes. To obtain inlet measurements out of the influence of the duct curvature, and to allow the probes to reach as much of the cross section as possible, the inlet plane was defined in the straight, constant area portion of the test section 1.65 cm (0.65 in) upstream of the beginning of the divergence and curvature (Figure 9). The diffuser exit plane was defined as the axial station where curvature and divergence ended and the test section flowpath resumed a straight, constant-area cross section. The distance between the inlet and exit planes was 7.66 cm (3.01 in).

Instrumentation. The model design incorporated several features which allowed simple and flexible data collection. Static pressure ports in the lower surface allowed measure of the axial pressure distribution. Pitot pressure, static pressure, and hot wire probes were inserted through the upper surface to measure flow properties across the inlet and exit planes. A stepper motor controlled the location of the traversing probes. All data was captured and recorded by a Nicolet Multipro data acquisition system.

Surface Static Pressure Measurement. Six 0.159 cm (1/16 in) ports on the centerline of the baseline (no blowing) lower surface measured static pressure along the test section floor. These were located at the inlet plane and the exit plane, and at four stations in between: 2.3368 cm (0.92 in), 3.493 cm (1.375 in), 5.334 cm (2.10 in), and 6.198 cm (2.44 in) downstream of the inlet plane. The lower surface with VGJs installed was instrumented with static ports at the inlet and exit planes only. An additional transducer measured the static pressure in the plowing plenum. The lower surface block was thick enough to allow for direct mounting of the transducers.

Pitot Pressure Measurement. The pitot rake entered the test section through 0.159 cm (1/16 in) slots cut completely across one of the test section upper surface blocks, allowing the probe to be relocated to any spanwise position without disassembling the model. The slots were sealed by 0.635 cm (0.25 in) thick aluminum plates and rubber gaskets held tightly over the slots by clamps bolted to the sideplate frames. When tightened, this arrangement produced an airtight seal except for a very small amount of leakage around the probe where it passed through the aluminum plate. The disturbances caused by the slots were deemed acceptable since the flow region of main interest was near the lower surface, which was to the inside of the first bend. Probes were aligned in the axial direction using geometric references. Estimated accuracy of this alignment was ± 3 degrees, within the standard tolerances for pitot probe alignment.

The pitot rake itself was manufactured from 0.14732 cm (0.058 in) outside diameter thin-wall steel tubing. 1.27 cm (0.5 in) projected upstream from the shaft into the flow. The edges around the opening were beveled to present less of a blunt edge to

the stream. The 90° bend between the shaft and the port section was of small radius, allowing the probe to reach all the way from the lower surface to within 0.254 cm (0.1 in) of the upper surface. Flexible plastic tubing connected the shaft exit to a transducer mounting block.

Static Pressure Rake. This probe entered the test section through the same slots as the total pressure rake. The static probe was also fashioned from 0.14732 cm (0.058 in) outside diameter thin-wall steel tubing. The 1.524 cm (0.6 in) section containing the ports was bent 90° to the shaft to point into the flow. The open end of this segment was sealed shut with solder, and four tiny holes drilled into the tube walls 1.27 cm (0.5 in) ahead of the shaft. This put the static orifices at the same axial location as the end of the pitot tube. Flexible plastic tubing connected this probe to a transducer mounting block.

Upstream Total Pressure Measurement. A fixed pitot probe located on the centerline of the inlet tube 11.049 (4.35 in) upstream of the inlet plane measured the freestream total pressure used to nondimensionalize all test data. This probe extended 0.635 cm (0.25 in) into the flow from the upper surface. The hole where it penetrated the surface was sealed with epoxy. Flexible plastic tubing connected the shaft to a transducer mounting block.

Pressure Transducers. Endevco Model 8510B-100 piezoresistive pressure transducers and their associated Endevco Model 4423 signal conditioners were used for all pressure measurements. These transducers had an operating range of 0 to 687 KPa (0 to 100 psig) gage pressure and a guaranteed accuracy of $\pm 0.5\%$ of the full-scale output.

The signal conditioner gain was guaranteed to within $\pm 0.5\%$ full-scale output, and the maximum noise level guaranteed to less than 5 mV peak-to-peak.

Each transducer was calibrated with its designated signal conditioner and cable using an Ametek pneumatic pressure tester. All transducers were initially calibrated over their complete operating pressure range, with a signal conditioner gain setting of 20. To improve sensitivity to small pressure changes, all were recalibrated from 0 to 345 KPa (0 to 50 psig) with a gain setting of 50. The full-range calibration was used only for the blowing plenum pressure transducer, as the pressure at all other measurement stations was below 345 KPa during the tests. The calibration curves resulting from either type of calibration were very linear. Recalibration of several transducers late in the test program showed negligible shift in sensitivity.

During the calibration process, a set screw on the signal conditioner was used to zero the output when no pressure was applied. Setting the output to exactly zero proved difficult, but extreme precision was not required because small biases could be canceled out easily by the data acquisition system. The zero-applied pressure reading did drift slightly with changes in temperature, but resetting the zero reading daily via the data acquisition system eliminated most of this effect.

Hot Film Probes. Hot film probes measured components of fluid mass flux at frequencies high enough to allow determination of mean and turbulent flow properties. The probes entered the test section through 0.4826 cm (0.19 in) diameter holes drilled in the second test section upper surface. Three holes were located 12.446 cm (4.9 in) aft of the beginning of the test section at $z = 0.762$ cm (0.3 in), $z = 1.27$ cm (0.5 in) (centerline),

and $z = 1.778$ cm (0.7 in), to allow measurement at three spanwise positions on the exit plane. An additional hole was positioned to allow measurement on the centerline at the inlet plane, but this was not used during these tests. The holes were sealed in a manner similar to that described for the pressure rakes.

TSI Model 1218-20 normal film boundary-layer probes (Figure 12) were initially used for measurement of streamwise flow properties. These probes had one $51 \mu\text{m}$ (0.002 in) diameter platinum film held between 2 gold-plated support pins. The sensing region was 1 mm (0.04 in) long. TSI Model 1243-20 and 1243-AN-20 cross-wire boundary layer probes (Figure 13) were used to measure the xy - and xz -components of flow properties, respectively. Each held two wires in the measurement plane, at $\pm 45^\circ$ to the x -direction. Wire dimensions were the same as for the normal wire probes. Boundary layer probes incorporate a large radius bend to position the sensing wires upstream of the influence of the shaft. Interference between this bend and the test section upper surface limited the region of the test section accessible for hot film measurements. The probes were able to reach from near the lower surface to just over halfway across the exit plane in the y -direction.

Hot Film Anemometer. The hot film anemometry setup consisted of a TSI Intelligent Flow Analyzer (IFA) 100 system serial number 339C with 3 IFA 150 constant-temperature anemometers installed. Single wire probes were connected to channel 3 of the IFA 100 system, while cross-wire probes connected to channels 2 and 3. Operating resistance was set for each probe to the value recommended by the manufacturer when this data was available. This typically resulted in an overheat ratio around 1.57. For

repaired probes with no factory data, an overheat ratio of 1.5 was chosen and the appropriate operating resistance calculated from the measured cold resistance. System frequency response was tuned for each probe while installed in the test section using the procedure given in the IFA 100 System Instruction Manual (TSI, 1987). Estimated frequency response was 200 KHz.

Hot Film System Calibration. Each probe was calibrated in the anemometer, probe holder, and connection cable configuration used during actual testing. Calibrations were performed using a TSI IFA 1125 multi-orifice calibration rig, accurate to $\pm 2.0\%$ for velocities above 3.0 m/s. The air total temperature was equal to that in the test section, but the density was reduced by about one-half. Since the hot film heat transfer is sensitive to the mass flux ρU rather than the velocity U , a valid calibration could be obtained at reduced density if the calibration velocity was increased. Thus, calibration data took the form of ρU vs V , and gave calibration curves of the form:

$$V^2 \approx Nu = a\sqrt{Re} + b = a\sqrt{\frac{\rho Ud}{\mu}} + b$$

Total temperature in the test section varied by $\pm 1^\circ K$ ($\pm 2^\circ F$), and the total temperature at the calibrator was equal to that in the test section, so it was not necessary to account for the effect of temperature on the hot film probe calibrations.

Data Acquisition System. A Nicolet Multipro data acquisition system with four Model 120 boards collected, synchronized, and recorded data from the pressure transducers and the hot film anemometry system. Each board could acquire up to 256000

points of data at sample rates up to 1 MHz. Each board had 12-bit resolution and a maximum static error of $\pm 0.25\%$ full-scale. The timebase was accurate to 0.01%. Other error specifications are given in the Nicolet Multipro Data Acquisition System Operations Manual (Nicolet, 1991). Though the system was capable of collecting 16 channels of data (4 channels per board), only 8 channels were needed for pressure data runs, and only 4 channels were needed for hot film data runs.

The Nicolet system was controlled by Nicwin interactive software loaded on a Zenith 386-type personal computer. The software displayed channel traces of test data immediately post-test, and allowed great flexibility in data acquisition. Calibration sensitivities were input to give pressure transducer output in pressure units rather than volts. Calibration offsets were updated before each set of runs to cancel out the temperature-related zero shift. Board input magnitude limits were adjusted to improve sensitivity. Sampling rate and duration were adjusted as needed.

Data Reduction. Basic data reduction functions, such as determining the average of a signal over a specified time interval or dividing a pressure measurement by the upstream total pressure, were performed by the Nicwin software. Static and total pressure sweep data were reduced using code written in the Matlab command language on a Sun Systems Sparc 20 workstation. Reported pressure measurements were the average of at least 60 samples of data. Hot film data was preprocessed in Matlab and then reduced by a FORTRAN code called MSHEAR, provided by Dr Rodney D. W. Bowersox

(Bowersox, 1992). This code was also run on the Sparc 20. Hot film mean and RMS data was calculated from 10000 samples per station.

Uncertainty Analysis. Appendix A details an analysis which estimated the uncertainty in each quantity measured directly or calculated directly from measured data. The analysis considered the cumulative effect of the accuracy of each component of the data measurement, acquisition, and reduction process. Table 3 summarizes the results.

Table 3

Uncertainty Analysis Summary

Quantity	Estimated Uncertainty (% of reading)	Estimated Uncertainty (units)
Upstream Total Pressure	± 1.0	$\pm 2.5 \text{ KPa (} 0.364 \text{ psi)}$
Rake Total Pressure	± 1.3 to 1.5	$\pm 3.30 \text{ KPa (} 0.478 \text{ psi)}$
Total Pressure Recovery	± 1.8 to 2.0	± 0.018
Rake Static Pressure	± 1.0	$\pm 2.11 \text{ KPa (} 0.307 \text{ psi)}$
Static Pressure Recovery	± 1.0	± 0.012
Surface Static Pressure	± 1.0	$\pm 2.08 \text{ KPa (} 0.303 \text{ psi)}$
Pitot-Static Mach Number		± 0.03
Hot Film Mean Velocity	± 6.3	
Turbulence Intensity	± 11.9	
Turbulent Kinetic Energy	± 20.0	
Turbulent Shear Stress	± 17.0	

The uncertainty analysis showed that the largest error components were due to imprecise placement of the probes in the flow. Total pressure and hot-film measurements were very sensitive to position as significant velocity and pressure gradients existed in the measurement planes. The effect of random errors was essentially eliminated by the large number of samples which combined to form each data point.

Flow Visualization. Surface flow visualization was performed by placing arrays of small dots or thin lines of viscous oil-based dye on the internal surfaces of the test section. The dye was applied through a thin, flat-tipped piece of plastic tubing attached to a small syringe. Dots were tried first but it proved hard to achieve a sufficiently small dot size. Thin lines were more easily made, and were used for most flow visualization runs. All pressure transducers downstream of the locations where the dye was applied were removed for these tests. Results were documented through sketches, still photographs, and video footage.

Test Procedures and Conditions

Experimental Procedure. The test facility was designed for continuous operation and the data system had ample capacity, so data collection did not need to be hurried and enough time could be spent at each test point to ensure good data. Operation of the facility for each type of test followed a similar procedure, though flow visualization runs

required some special consideration to insure that valid surface streaklines were produced right at startup.

General Operating Procedures. After verifying all air supply valves were closed and all instrumentation was connected and operating, one short-duration (10 seconds typical) sample of data was acquired. Each pressure transducer signal in the set was averaged to determine the calibration offset required to cancel out the zero shift. The relative magnitude of the offset required to zero each transducer was very repeatable, and the component of the zero shift due to temperature was less than 1.3 KPa. The appropriate offsets were entered into the Nicwin software, and the system was ready for test.

The control pressure regulator was then set to give the desired pressure in the settling chamber, and the air valves were opened to allow air to flow through the test section. At this point, it was necessary to manipulate an air dump valve in order to keep the supply pressure from spiking whenever the compressors turned on or off.

The compressors were set to charge the air supply system to 689 KPa (100 psig), but their controller allowed the pressure in the system to drop to approximately 579 KPa (84 psig) before turning on the first compressor. Usually, one compressor was sufficient to recharge the system to 689 KPa, at which point the compressor would shut off and allow the supply pressure to drop back down to 579 KPa before repeating the process. If

the pressure in the system stayed low for approximately 5 minutes, the second compressor would come on and remain on until the pressure reached 689 KPa.

Initial tests showed that the pressure transients which occurred when the compressors cycled on and off were not damped out by the pressure regulator valve and produced unwanted fluctuations in the data. It was necessary to adjust the dump valve to maintain a supply pressure of around 551 KPa (80 psig) with first one and then both compressors operating. This amounted to dumping overboard the entire mass flow of the compressors which did not flow through the test section. In practice, it was difficult to set the dump valve to hold exactly 551 KPa, but the pressure regulator valve could damp out a slow drift in supply pressure. Typically, it was necessary to adjust the dump valve only twice during an 10 minute run.

Air was supplied to the blowing plenum once the supply pressure was near 551 KPa on those runs where it was required.

With the supply pressure stabilized, the data system was triggered and then, 5 seconds later, the probe traverse system activated. Before beginning each new set of runs, a brief set of data was acquired to check the test section inlet Mach number, and the variable diffuser throat was adjusted as necessary. Test section inlet Mach number was repeatable to within ± 0.1 M, and test section inlet total pressure was repeatable to within ± 2.07 KPa (+0.3 psig).

Flow Visualization Operating Procedure. The only runs that did not follow this procedure were those conducted as part of the flow visualization study. Then, a different procedure was needed to insure that the supply pressure and blowing plenum pressure, when applicable, were at their normal operating values when the flow through the test section was initiated. To achieve this, the dump valve was opened first, to lower the supply pressure to well below 551 KPa and bring both compressors on line. The dump valve was then closed to the approximate position needed to maintain 551 KPa when air was flowing through the test section. As the pressure recovered to 551 KPa, the valve to the test section was opened and the supply pressure stabilized at the desired value very quickly. For flow visualization runs with the blowing VGJs active, the blowing plenum pressure regulator was set to give the desired pressure in the plenum during a preceding run and left open until the test run was complete.

Test Conditions. Though the model was designed to operate at supply pressures up to 515 KPa (75 psig), satisfactory flow conditions were obtained at significantly lower pressures. The supply pressure was then regulated to approximately 199 KPa (29 psig) by the Leslie valve for all data runs. In hindsight, this proved to be a wise choice; one compressor was inoperative for a substantial portion of this program, and the remaining compressor could not have provided sufficient mass flow if the tests had been performed at the higher pressure. Decreasing the operating pressure decreased the mass flow requirement to less than half of the original value.

Data was collected for two diffuser inlet Mach number conditions: $M_1 = 0.6$ and $M_1 = 0.8$. The $M_1 = 0.6$ case was the primary test condition, and a full set of data was collected for that inlet condition. Extreme vibration at the $M_1 = 0.8$ case shortened the life of the hot-film probes and led to the abandonment of that test condition after only blowing-off total pressure recovery data had been acquired. Table 4 details the test matrix.

Table 4

Test Matrix

Test Type\Condition	$M_1 = 0.6$	$M_1 = 0.8$	$M_1 = 0.6$
	Blowing Off	Blowing Off	Blowing On
Inlet Plane Total Pressure Survey	X	X	
Exit Plane Total Pressure Survey	X	X	X
Exit Plane Static Pressure Survey	X		X
Exit Plane Normal-Film Survey	X		
Exit Plane Cross-Film Survey	X		X
Flow Visualization	X	X	X
Lower Surface Static Pressure	X	X	X

IV RESULTS AND DISCUSSION

Data was collected during several series of runs conducted between July and October 1994. Appendix B details the purpose and date of each run. All reported pitot-static data is the average of at least 60 data samples at each measurement location. Inlet plane data was sampled at 20 Hz, while exit plane data detailed in this chapter was sampled at 50 Hz. The traversing rake dwelled at each measurement station for approximately 10 seconds to eliminate lag. To correlate data from successive runs, measured pitot-static data was normalized to reflect an ambient atmospheric pressure of 98.5 KPa (14.28 psi) and an upstream total pressure of 259.1 KPa (37.58 psi).

Normal-film probe data reported here was acquired at 200 KHz. 0.25 seconds of normal-film data was collected at each measurement location, from which 20000 data samples were extracted for reduction. Cross-film data was collected at 100 KHz, with 0.1 seconds of data recorded at each station. All 10000 data samples were reduced to produce each data point.

Measurement station cross-sectional locations (spanwise and vertical) were nondimensionalized by the width of the diffuser, b .

From the data, it was possible to characterize the performance of the test diffuser without blowing and for one blowing-on case, and to gain some insight about the flow processes which drive the performance. The results are logically divided into two categories: mean flow properties, the overall, time-averaged behavior of the fluid which determines the bulk measures of performance such as pressure coefficient, pressure

recovery, and efficiency; and turbulent flow properties, which help understand the flow processes and the performance by quantifying the amount of energy which is lost to random motion.

Mean Flow Properties

Inlet Plane Measurements. Data taken at the inlet plane verified the assumption that the boundary layers were turbulent at that point and showed that relatively uniform, undisturbed flow existed across most of the inlet plane. No inlet plane data was collected with the VGJs operating. It was assumed that the VGJs, located well downstream, would have an insignificant effect on the flow properties at the inlet plane.

Inlet Plane Pressure Recovery. Figure 14 shows a map of the total pressure recovery $\frac{P_{01}}{P_0}$ at the diffuser inlet plane for $M_1 = 0.6$. Figures 15 and 16 show 2 of the 9 total pressure recovery profiles used to generate the contours in Figure 14. These three figures display several noteworthy qualities of the flow at this location.

First, though there was a large region in the center of the cross-section where the flow was relatively undisturbed from freestream conditions, the wall boundary layers were quite thick compared to the dimensions of the test section - approximately 10% of the span of the test section along the lower surface, and 20% of the span on the other three walls. The boundary layer was even thicker in the corner regions, where the sidewall and

upper or lower surface boundary layers came together. The difference in the apparent thickness of the upper and lower surface boundary layers may be due to the effect of the first bend propagating upstream to the inlet plane. In the first bend, the flow along the lower surface experiences a local acceleration, while the flow along the upper surface experiences a local deceleration. The influence of these features can work upstream in a subsonic flow, and this may partially explain why the upper surface boundary layer appears to be twice as thick as the lower surface boundary layer at the inlet plane.

The effect of the wake of the reference pitot probe also appears in the inlet plane total pressure recovery data. On Figure 14, it appears as the region above $y/b = 0.35$ between $z/b = 0.4$ and 0.6 where the maximum total pressure recovery is reduced but the minimum total pressure recovery is increased. Comparison of Figures 15 and 16 shows this even more clearly. The centerline-station data in Figure 15 shows the total pressure recovery drops from nearly 1 to approximately 0.99 around $y/b = 0.35$. Then, it maintains 0.99 until above $y/b = 0.5$. This behavior did not appear in data taken before the installation of the upstream pitot probe. Off-centerline data in Figure 16 does not exhibit the same behavior; there is no intermediate decrease in pressure recovery, and the pressure recovery begins dropping off due to the presence of the upper surface at $y/b = 0.4$.

Figure 17 shows the total pressure recovery map for $M_1 = 0.8$. The flow behavior at this condition displayed features similar to those observed at $M_1 = 0.6$.

Inlet Plane Static Pressure. One vertical sweep of the centerline at $M_1 = 0.6$ showed that the static pressure varied by less than 3.46 KPa (0.5 psi) (approximately 1.6%) across the height of the test section. Based on this information, the pressure

measured at the tap located on the lower surface centerline was used as the value of the static pressure everywhere on the inlet plane.

Inlet Plane Mach Number. Figures 18 and 19 show Mach number contours at the inlet plane for the two inlet conditions. Mach number was calculated from measured values of P_t and P_s through isentropic flow relationships. The nominal $M_1 = 0.6$ condition gave a maximum Mach number of 0.605. Maximum flow through the variable diffuser produced a maximum inlet plane Mach number of 0.78, slightly short of the desired $M_1 = 0.8$ condition. These figures also show the presence of wall boundary layers and the wake of upstream reference pitot probe.

Inlet Plane Boundary Layer Profile. Using the total temperature measured in the settling chamber, isentropic flow relationships, and the perfect gas law, velocity profiles were generated for the lower surface boundary layer (Figures 20 and 21) at $M_1 = 0.6$. The boundary layer thickness, edge velocity, and Reynolds Number were determined as given in Table 5:

Table 5
Inlet Plane Boundary Layer Measurements

Quantity	Value
Boundary Layer Thickness (δ_{99})	0.272 cm (0.107 in)
Edge Velocity (U_e)	200 m/s (656 ft/sec)
Reynolds Number (Re_δ)	3.18×10^6

Comparison with the four theoretical models for the turbulent boundary layer plotted on Figures 20 and 21 - the 1/7 power law, the 1/8 power law, the incompressible law-of-the-wall, and the compressible law-of-the-wall - indicated that the lower surface boundary layer at the inlet plane was turbulent. Due to the small size of the model, no data was collected in the inner region of the boundary layer. The 1/8 power law, recommended for high-Reynolds Number flows over the more common 1/7 power law, and either form of the law-of-the-wall fit the data quite well. At $M_1 = 0.6$, compressibility effects were small.

For this analysis, the Coles wake parameter Π was kept at its zero pressure gradient value of 0.4 since the inlet plane was upstream of the diffusing section. Perhaps even better agreement with the data would have been achieved if it were reduced slightly to reflect the locally favorable pressure gradient felt near the lower surface because of the acceleration around the first bend.

Flow Visualization and Separation Point Determination. Surface flow visualization and shadowgraph photography provided the only direct indication of the flow processes occurring between the inlet and the exit planes. Data acquired through these techniques with the blowing off indicated that the flow along the lower surface of the diffuser was massively separated. The location of the blowing-off lower surface separation point as found by surface flow visualization was used to determine the placement of the vortex generator jets. The extent of the separated flow region was greatly reduced and the

character of the separated flow region was significantly altered when the VGJs were activated.

Shadowgraphs. Shadowgraphs taken at $M_1 = 0.6$ and $M_1 = 0.8$ without blowing show evidence of highly-turbulent, massively separated flow on the lower surface of the diffuser, beginning just downstream of the crest of the first bend. An additional area of separated flow appears along the upper surface just downstream of the second bend. The $M_1 = 0.8$ shadowgraph (Figure 22) showed a weak normal shock occurring in the flow near the lower surface just downstream of the first bend. This gave an indication of the magnitude of the acceleration occurring near the lower surface through the first bend - for the shock to exist the flow must have accelerated from $M_1 = 0.8$ to $M > 1.0$. The shock occurred as the flow then decelerated in the adverse pressure gradient. The large, jagged, dark lines extending diagonally across the aft third of the test section are scratches on the outside of the Plexiglas sidewall, not features of the flow.

Information gleaned from the shadowgraphs must be interpreted carefully. The images are a composite of the flow behavior occurring across the entire span of the test section, and therefore reflect the presence of the sidewall boundary layers. Areas of turbulent or separated flow seen in a shadowgraph may actually be confined to regions of small spanwise extent. Due to this limitation, the location of the separation point had to be verified by other means.

Surface Flow Visualization. Oil-droplet flow visualization on the test section lower surface at $M_1 = 0.6$ without blowing showed that the separated flow region began roughly 3.4 cm (1.35 in) downstream of the inlet plane, engulfed the entire span of

the diffuser, and persisted until a reattachment line just upstream of the exit plane. The geometry of the test section, its small size, and the difficulty of disassembling it made photography of the lower surface oil streak patterns very difficult; the sketch in Figure 23 is based on observed results and shows the patterns more clearly than photographs did.

The leading line of separation described a flattened U-shape, with the base pointing downstream. It connected two counter-rotating focus points, located at roughly $x = 3.5$ cm and $z/b = 0.2$ and 0.8 , and a saddle point located on the centerline at $x = 4.5$ cm. No fluid crossed this line. The fluid on the line itself was not stagnant, as would be expected for two-dimensional separation, but had significant spanwise and reverse components of velocity. The actual locus of points with no x -component of velocity traced out more of a V-shape and was located slightly upstream of the leading line of separation.

Two other reverse-flowing lines of separation joined the leading separation line at the focus points. These divided the completely reverse-flowing area around the center of the span from regions near the sidewalls where the fluid had a small component of velocity in the downstream direction. The direction of the flow near the sidewalls was surprising; since the floor boundary layer was thickest near the corners at the inlet plane, it was logical to expect that separation would begin in the corners and propagate towards the middle. The observed behavior was attributable to the secondary flows generated by the curvature of the duct, which swept fluid from the upper surface and sidewalls down the lower surface and then in toward its centerline. The boundary layer fluid along the upper surface and sidewalls was not separated and maintained a small component of velocity in

the downstream direction. As the secondary flow moved this fluid towards the center of the lower surface, the downstream velocity component diminished and then reversed.

Surface flow visualization revealed the behavior of the secondary flows. In the vicinity of the first bend, upper surface streaklines were deflected toward the sidewalls, sidewall streaklines (Figure 24) were deflected toward the lower surface, and lower surface streaklines were deflected toward the centerline of that surface. Farther aft, the second bend induced secondary flows of an opposite sense to those produced by the first bend, and the sidewall streaklines were inclined toward the upper surface. While the secondary flow produced by the first bend promotes separation of the lower surface boundary layer, the secondary flow produced by the second bend seemed to promote reattachment along that surface.

The lower surface boundary layer reattached near the apex of the second bend. Relief from the adverse pressure gradient as the duct resumed a constant cross section worked in concert with the secondary flows from the second bend to promote reattachment there.

Lower surface flow visualization provided information needed to finalize the placement of the VGJs. The proximity of the leading line of separation to the beginning of the curved, diffusing section left little room for the jets to be located upstream of the separation point. The location of the jet orifices was approximately 0.762 cm (0.3 in) upstream of the leading edges of the focus points. The jets were canted 45° toward $z/b = 0$, and pitched 25° relative to the local surface tangent. Lower surface flow visualization

was repeated at three different blowing rates: $\frac{\dot{m}_j}{m_d} = 0.002, 0.0025, 0.003$, and 0.0048 ,

corresponding to blowing plenum pressures of 172 KPa (25 psig), 241 KPa (35 psig), 310 KPa (45 psig), and 551 KPa (80 psig), respectively. Flow through the VGJs was choked at all but the lowest blowing mass flow rate, giving $VR = 1.57$.

Operation of the vortex generator jets greatly altered the lower surface flow pattern. The sketches in Figures 25 and 26 show the major surface flow features with the VGJs operating. The two foci observed during blowing-off flow visualization continued to mark the upstream limit of separation; they were located at approximately the same axial positions as for the blowing-off case. Between the foci, the leading line of separation was positioned much farther downstream than with blowing off. The leading line of separation traced out a V shape, with the apex located slightly upstream of the exit plane near the $z/b = 0$ sidewall. Inside the V, the streaklines pointed nearly straight down the diffuser, bending only to merge with the line of separation. The flow along the line of separation was directed toward $z/b = 0$, so that it maintained a downstream component of velocity across most of the width of the diffuser.

Increases in the blowing rate had two major effects on the surface flow pattern. The reattachment location on the $z/b = 1.0$ side of the lower surface moved upstream, decreasing the size of the reverse-flow region feeding the $z/b = 0.8$ focus. The amount of fluid traveling upstream along the $z/b = 0$ arm of the line of separation decreased, until

that section of the line of separation collapsed to form a recirculating whorl near the exit plane at $\frac{m_j}{m_d} = 0.0048$.

The maximum blowing rate was chosen for further study, since it caused the most dramatic changes in the surface flow patterns but yet required a relatively low mass flow (Ball, 1984). At this condition, it appeared that nearly all the lower surface flow was directed to the recirculating whorl on the left side near the exit plane. Attached flow was maintained over a much larger area of the lower surface than without blowing. Surface flow visualization made it clear that the vortex generator jets definitely altered the flow structure in the highly-offset diffuser, but could not quantify their impact on the diffuser's performance or lend much insight on the processes by which the VGJs modified the flow.

Lower Surface Static Pressure. The only measurements taken between the inlet and exit planes were of the lower surface static pressure. Lower surface static pressure was measured at six locations along the centerline without blowing. Figure 27 shows the pressure coefficient along the diffuser lower surface centerline as a function of axial distance from the inlet plane. The taps were spaced too far apart to provide detailed information on the behavior of the axial pressure gradient, but some important trends were visible. The blowing-off data clearly showed the local favorable pressure gradient caused by the expansion in the first bend, in the vicinity of $x = 2.5$ cm, followed by an adverse pressure gradient through the diverging section of the duct. The adverse pressure gradient was very strong immediately aft of the first bend, but decreased in the region of separated

flow. The data did not appear to level off through the separated flow region, as seen by other researchers (Vakili et al., 1987; Rehman et al., 1990; Wellborn et al., 1992), though this behavior may have been hidden by the large axial distance between measurement stations. The persistence of the adverse pressure gradient aft of the separation point is consistent with the reverse flow observed on the lower surface of the duct.

Hill and Peterson (1992) state that, as a general rule-of-thumb, a turbulent boundary layer can flow against an adverse pressure gradient to attain an increase in C_p of 0.4 to 0.8 before it will separate. For the test diffuser, the change in C_p between the separation point and point of minimum pressure was just less than 0.4. This suggests that the secondary flows cause the lower surface boundary layer to grow faster than it would in a nominally two-dimensional flow, leading to earlier separation.

The test section lower surface with VGJs installed had pressure taps at only the inlet and exit planes, so similar data was not collected for the blowing-on case. The exit plane C_p is a valid measure of overall diffuser performance, and comparison of exit plane C_p values between the blowing-off and blowing-on cases gives an indication of the relative performance of each diffuser configuration. The exit plane C_p was 0.343 for the blowing

off case, and 0.524 for blowing at $\frac{\dot{m}_j}{\dot{m}_d} = 0.0048$. These values were computed using

equation (2), which accounted for the energy added by blowing. The increase in C_p between the blowing-off and blowing-on configurations, then, represents a real improvement in performance and indicates that more diffusion was occurring in the duct when the VGJs were operating. However, both values may have been artificially inflated

due to the location of the surface pressure tap with respect to the second bend. The tap was located just aft of the apex of the curve, on the lower surface where the flow experiences a local compression. The pressure measured at that point was higher than the mean static pressure across the duct exit plane. Pressure coefficient results for comparison to other diffuser geometries are better obtained using the face-averaged static pressure computed from measurements taken across the diffuser exit plane. This data will be presented in a later section.

Exit Plane Total Pressure Recovery. Total pressure recovery is the performance measure most commonly used for aircraft engine inlet diffusers, since it quantifies the amount of energy lost during the diffusion process. Comparison of exit plane pressure recovery data collected with and without blowing showed that activation of the VGJs increased the face averaged pressure recovery, increased the diffuser isentropic efficiency, decreased the level of distortion as calculated by the min/max method (equation (4)), but increased the level of distortion calculated by the maximum gradient method (equation (5)).

Total pressure is proportional to the momentum of the fluid, and thence to the velocity. The pitot probe was aligned with the x-axis, so the measured total pressure was sensitive only to the +u component of velocity. Spanwise and reverse flows could not be detected by the probe. Thus, the total pressure measurements reported here related to the component of the fluid momentum directed along the axis of the diffuser. In practice, this is the component available to do useful work, for the energy contained in the other

velocity components is not recovered unless the device to which the diffuser leads is specifically designed to use the swirl.

Figure 28 shows the exit plane total pressure map without blowing at $M_1 = 0.60$. The blowing-off map clearly showed that a large amount of energy was lost in the separated lower surface boundary layer. The total pressure was significantly reduced from its nominal freestream value over nearly the entire lower half of the diffuser exit plane. Total pressure losses were greatest near the lower surface around $z/b = 0.2$ and $z/b = 0.8$, essentially straight downstream of the location of the focus points which marked the upstream limit of separation. Corner-flow effects from the upper surface/sidewall junctions caused losses which created local regions of reduced total pressure in the upper corners. The face-averaged total pressure recovery was 0.9298, which gave an isentropic diffuser efficiency of 0.693.

The total pressure contour pattern was similar to that presented by Ball (1983) for a rectangular cross-section highly-offset diffuser. For a circular cross-section duct, the region of lowest total pressure would be centered around the lateral centerline, slightly above the duct floor (Vakili et al., 1987; Bansod and Bradshaw, 1972; Wellborn et al., 1992), and the recovery would increase in any direction.

Though it was depressed significantly from its freestream value, the total pressure field varied smoothly over the exit plane. The y-component of the total pressure gradient in the lower half of the duct was quite uniform, and total pressure gradients in the z-direction were significant only near the sidewalls and in the corner regions near the upper

surface. The distortion calculated by the maximum/minimum method was 0.170, while the distortion calculated by the maximum gradient method was 0.055.

For comparison, Figure 29 shows the exit plane total pressure map for the $M_1 = 0.8$, blowing-off case. It exhibits the same trends as discussed for the $M_1 = 0.6$ case.

Figure 30 shows the exit plane total pressure recovery map for $\frac{\dot{m}_j}{\dot{m}_d} = 0.0048$.

Compared to values measured without blowing, blowing increased the pressure recovery on the right side of the diffuser quite substantially, but an accumulation of low-momentum fluid near the left sidewall actually reduced the total pressure recovery at some locations on that side of the diffuser. The lowest pressure recovery values were measured near the lower surface at $z/b = 0.3, 0.5$, and 0.7 - directly downstream of the jet locations.

Between those stations, the near-surface pressure recovery was increased by nearly 5% over the blowing-off values. In the upper half of the exit plane, the total pressure contours appeared virtually unchanged by blowing. The overall face-averaged total pressure

recovery for blowing at $\frac{\dot{m}_j}{\dot{m}_d} = 0.0048$ was 0.9425, and the isentropic diffuser efficiency

was 0.750. The min/max distortion decreased to 0.152, but the maximum gradient distortion increased to 0.082. Table 6 compares total pressure-based diffuser performance parameters for the blowing-on and blowing-off cases.

Table 6
Total Pressure-Based Diffuser Performance Comparison

	r_d	η_d	min/max distortion	max gradient distortion
Blowing Off	0.9298	0.693	0.170	0.055
Blowing On	0.9425	0.750	0.152	0.082
% change with blowing	1.37	8.22	-10.6	49.1

The preceding comparison highlights the difference between the two methods used to calculate distortion. The min/max distortion decreased for the blowing-on case since the minimum total pressure and the face-averaged total pressure measured at the exit plane were both higher than without blowing. The maximum gradient distortion increased with the blowing on, because the gradients in the total pressure field were larger. The total pressure gradient in the y-direction was no longer uniform, and significant total pressure gradients existed in the z-direction in the lower half of the duct. On the whole, then, the use of VGJs for flow control decreased the energy losses in the diffuser, as evidenced by increased pressure recovery and isentropic efficiency, at the expense of a less uniform total pressure field, evidenced by the increased maximum gradient method distortion.

With the blowing on, the fluid with the lowest total pressure, and hence the lowest momentum, passed through the lower left ($z/b = 0$) quadrant of the exit plane. This is consistent with the behavior observed during surface flow visualization, which showed that virtually all of the flow near the lower surface was directed towards that corner of the exit plane. This feature of the flow is further evidenced by the total pressure profiles plotted in Figures 31 - 39.

Similar features are apparent in the total pressure recovery profiles at each spanwise station for the blowing-off condition. The inflectionary profile in the lower half of the duct was characteristic of flow under the influence of an adverse pressure gradient. Near the bottom of the duct, the slope of each of the blowing-off profiles approached infinity. Comparison to static pressure measurements taken across the exit plane (Figures 40 - 44) found that the static pressure and the total pressure were nearly equal below $y/b = 0.1$, implying that the flow in that region had a very small $+u$ velocity component. Flow visualization indicated that the reattachment point was just upstream of the exit plane, so it is not surprising that the flow through the exit plane near the lower surface has little streamwise momentum. The lower portion of the exit plane was in the wake of the separated-flow region. The profiles were fullest near the center of the duct, away from the influence of the sidewall boundary layers. Near the sidewalls, the thickness of the separated regions reached to almost $y/b = 0.2$, and the maximum total pressure was reduced as well.

The increased spanwise variation of the total pressure field is evident in the total pressure profiles measured with blowing on. At $z/b = 0.1$, the effect of blowing is minimal. When plotted alongside the blowing-off total pressure profile measured at that location (Figure 31), it is seen that greater total pressure losses are incurred in the upper half of the boundary layer than without blowing. The profile at $z/b = 0.2$ is similar, except that the effect of the plume of the jet can be seen very near the lower surface. This effect is even more evident at $z/b = 0.3$, and it is centered slightly farther above the lower surface. The near-floor total pressure recovery increased, but the increased-loss region

above the plume persisted between $y/b = 0.25$ and $y/b = 0.5$. The trend established by the preceding two stations continued at $z/b = 0.4$: the center of the plume was still higher off the floor, the near surface pressure recovery increased, and the region above the plume was of lower momentum than without blowing. The thickness of the low-momentum layer above the plume was decreased from $z/b = 0.3$.

The profile at $z/b = 0.5$, the diffuser centerline (Figure 35), appeared quite different than those to the left of it, but the changes followed the trends established through the preceding discussion. It appeared that the jet plume lifted higher off the floor so that it merged with the high-momentum fluid in the top half of the duct, producing a full profile. The profile below the center of the jet plume was not inflected. The pressure recovery across most of the height of the diffuser was greater than 0.98. A substantial increase in pressure recovery was obtained over the entire lower half of the duct.

The total pressure recovery profiles followed a different trend from $z/b = 0.6$ toward the $z/b = 1.0$ sidewall. At these stations, the effect of the jet plume was not discernible, and a point of inflection reappeared in the lower section of the profile. The slope near the lower surface again approached infinity, though comparison to measured values of static pressure indicated that the flow maintained a component of velocity in the $+x$ direction. The pressure recovery over the entire lower half of the duct was increased over the blowing off case, though the magnitude of this increase diminished with proximity to the $z/b = 1.0$ sidewall.

Figures 33, 35, and 37 give some indication of the effect of blowing rate on total pressure recovery, as data for all four blowing rates is plotted on those figures. In all

three figures, the pressure recovery measured near the lower surface increased with the blowing rate, due to the energy added by the blowing and the more efficient diffusion achieved as the boundary layer blocked less of the cross-section area. Surprisingly, changes in the blowing rate affected the total pressure recovery profile only along the centerline. At the other stations, all blowing rates tested produced nearly identical profiles.

At $z/b = 0.3$ (Figure 33), the region of increased losses and decreased momentum between $y/b = 0.2$ and $y/b = 0.5$ was evident at all blowing rates. Through that region, increases in the blowing rate had no effect on the measured total pressure recovery. Between that region and the lower surface, the effect of the jet plume was not discernible at $\frac{m_j}{m_d} = 0.0020$, and the slope of the profile was nearly infinite as it approached its near-surface value. As the blowing rate increased, the effect of the plume became discernible, and its center moved closer to the lower surface.

On the centerline (Figure 35), the fullness of the lower half of the profile increased with blowing rate. For the lowest blowing rate, there was a small region between $y/b = 0.325$ and $y/b = 0.5$ where the pressure recovery with blowing was less than that without, but this area disappeared as the effect of the plume became discernible at the higher blowing rates. Above the diffuser centerline, the pressure recovery at all blowing rates was the same as that without blowing.

Figure 37 shows the data measured at $z/b = 0.7$. Below the centerline, increasing the blowing rate only affected the value of pressure recovery near the surface; all blowing

rates produced a substantial gain in pressure recovery elsewhere in the lower half of the diffuser. Above the centerline, increases in the blowing rate seemed to decrease the measured values of pressure recovery slightly.

While total pressure measurements give a useful indication of the way blowing redistributes momentum in the diffuser, they do not lend much understanding of how the redistribution occurs. Obviously, the VGJs do more than just add high-momentum fluid to the flow. The decrease in momentum in the lower left corner of the exit plane is counterintuitive, since the high-momentum fluid from the jets is directed towards that location as it leaves the jet orifices. Other measurements, then, are necessary to attempt to deduce the flow processes occurring in the diffuser with the VGJs blowing.

Exit Plane Static Pressure. The static pressure field was measured across the diffuser exit plane for the blowing off and $\frac{\dot{m}_j}{\dot{m}_d} = 0.0048$ cases. These measurements confirmed the result suggested by the lower surface static pressure measurements: blowing significantly increased the amount of diffusion occurring in the highly-offset diffuser. Contour plots of static pressure recovery are shown in Figures 45 and 46, while static pressure recovery profiles were shown in Figures 40 through 44.

With the blowing off (Figure 45), the static pressure decreased smoothly from its maximum at the lower surface to its minimum value at the upper surface. The overall face-averaged value of $\frac{P_s}{P_0}$ was 0.823. The static pressure gradient in the y-direction was

nearly uniform, and there was essentially no static pressure gradient in the x-direction. The vertical pressure gradient resulted from the local acceleration occurring in the upper half of the duct and the local deceleration in the lower half of the duct due to the axial curvature. The pressure gradient drove the secondary flows, which, in turn, caused boundary layer fluid from all surfaces to migrate toward the surface on the inside of the curve.

Compared to the results of Vakili et al. (1987), the static pressure distribution resembled that for a region near the center of the cross section of a circular duct. Near the walls, the contour lines for a circular duct bend to take on the curvature of the wall.

Blowing modified the exit plane static pressure field only slightly (Figure 46). The face-averaged value of static pressure recovery was significantly increased, to 0.845, and the magnitude of the pressure difference between the upper and lower surfaces appeared to be nearly the same. Pressure gradients still existed primarily in the y-direction, though the gradient was steeper near the lower surface, and local regions of lateral pressure gradient were more prevalent.

While the highest value of static pressure was measured near the lower surface centerline, the entire lower corner near the $z/b = 1.0$ sidewall exhibited the greatest overall increases in static pressure recovery compared to the blowing-off case. This result was consistent with the results of surface flow visualization and the total pressure survey, which suggested that high momentum fluid reached the closest to the lower surface between $z/b = 0.4$ and the $z/b = 1.0$ wall. Less energy was lost to the boundary layer, so more was available for conversion into pressure energy. Because the fluid in the lower

right quadrant of the test section had higher momentum than that in the lower left, it experienced a greater compression due to the curvature of the diffuser.

Figures 45 and 46 clearly show that a value for the overall duct C_p based upon a static pressure measurement taken on the lower surface would be artificially elevated due to the local effect of the curvature of the diffuser. A more appropriate value is based on the face-averaged static pressure. Table 7 shows these values and compares them to the lower surface static pressure-based values presented previously:

Table 7
Diffuser Exit Plane Pressure Coefficient

Configuration	C_p (based on face-averaged static pressure)	C_p (based on lower surface static pressure)
Blowing Off	0.239	0.343
Blowing On	0.378	0.524
% increase with blowing	58	53

The data in Table 7 shows that using the lower surface static pressure to compute the overall pressure coefficient for a curved diffuser led to inaccurate results, but that the percent increase in C_p due to blowing was roughly the same no matter how it is calculated. More importantly, it also shows that blowing, as implemented in this diffuser, increased the static pressure rise achieved in the diffuser by over 50%. This suggests that implementation of a boundary layer control system using vortex generator jets could permit short, highly-offset diffusers to achieve the same pressure rise currently obtained by

longer or less-offset ducts. The increased distortion of the exit plane static pressure field, like that of the total pressure field, is not a desirable result, and its effects must be considered relative to the gain in pressure recovery.

Exit Plane Mach Number. Exit plane Mach number information was available from three separate sources: from total and static pressure measurements via isentropic flow relationships, from cross-film probe measurements, and from normal film data. Each source measured a slightly different quantity. The values computed from pressure measurements represented the +x component of Mach number only, since the total pressure probe was sensitive to only the +u component of velocity. The normal film data, available for the blowing off case only, represented the x and y components of Mach number since the film was not sensitive to velocity components which were tangential to it. By combining data from probes oriented in the xy- and xz-planes, the cross-film data accounted for all three components of velocity. Mach number information from each source confirmed the trends introduced in the total pressure recovery data.

Figures 47 - 48 show Mach number contours computed from measured total and static pressure information at five spanwise stations with the blowing off and with

$$\frac{m_i}{m_d} = 0.0048,$$
 while Figures 49 - 53 show the Mach number profiles which were combined to produce the contour plots. The profiles exhibit the same trends observed from the total pressure profiles. At each station, the maximum Mach number for blowing on is considerably less than for blowing off. The peak Mach number with blowing off was near 0.54, while with blowing this decreased to just below 0.50. This was due to the

increased diffusion achieved with blowing on. For an equivalent total pressure, the increase in exit plane static pressure translated to a lower flow Mach number.

Blowing did increase the Mach number in the vicinity of the lower surface. The minimum Mach number measured with blowing on was just above 0.1, compared to 0.0 for blowing off. Consistent with observations based upon total and static pressure data, this indicated that the near-surface flow maintained some $+x$ momentum only with blowing on. Mach numbers measured in the lower left quadrant of the exit plane with blowing on were lower than those measured there with blowing off, again indicating that blowing somehow reduced the momentum of the fluid passing through that region.

Exit plane Mach number profiles generated from hot-film probe data appear in Figures 54 - 56 (cross-wire data) and 57 - 58 (normal wire data). This data is limited to below $y/b = 0.5$, since the hot wire probes were confined to the lower half of the test section due to geometrical constraints. These figures confirm the general trends found in the Mach number profiles derived from pressure data. Interestingly, the minimum Mach number values measured by the hot-film probes was not as low those calculated from pressure data.

Figure 59 compares the Mach number derived from each of the above sources at the exit plane centerline with the blowing off. Through the heart of the boundary layer, the values computed from each source are in good agreement. Near the surface and near the boundary layer edge, however, significant discrepancies exist. Near the surface, the cross-film probe data gave the highest indicated Mach number, followed by the normal-film. As \bar{u} decreases in that region, the magnitudes of \bar{v} and \bar{w} become more significant

in comparison to \bar{u} , though \bar{u} is still dominant. Since the cross-film probe sensed both of these components, and the normal-film probe sensed one of them, it follows that data from those sources should indicate a higher Mach number than the pitot-static data. In a strongly three-dimensional boundary layer, the contribution of any velocity component cannot be neglected. At the outer regions of the boundary layer, as $M \Rightarrow 0.5$, hot-film sensors become dependent on Mach number, reducing the accuracy of the data.

Exit Plane Mean Velocity and Flow Angularity. Cross wire probes provided information on the three mean velocity components, \bar{u} , \bar{v} , and \bar{w} . The local flow angle may be determined from their relative magnitude at a point. Analysis of this data showed that activation of the VGJs substantially altered the secondary flow structure which favored separation along the lower surface.

Figures 60 - 62 show the measured velocity components for the blowing-off case, while Figures 63 - 65 show similar data for $\frac{\dot{m}_j}{\dot{m}_d} = 0.0048$. The corresponding mean flow angles are plotted in Figures 66 - 71. Angles are measured from the x-axis, which faces downstream, and are defined as positive in the xy-plane towards the upper surface, and positive in the xz-plane toward the $z/b = 0.0$ sidewall. While data for \bar{u} , \bar{v} , and the angle they form in the xy-plane confirmed the observations made from pitot-static data discussed earlier, data in the xz-plane provided valuable insight into the rotational behavior of the flow.

Exit Plane xz-plane Rotational Behavior. The spanwise component of mean velocity, \bar{w} , and hence the xz-plane flow angle, was strongly affected by the blowing. Without blowing, the spanwise velocity component at either off-centerline station showed that the flow near the surface was moving towards the centerline. At $z/b = 0.7$ (Figure 62), the \bar{w} component changed sign near $y/b = 0.13$ and reached a local maximum at $y/b = 0.2$. The xz-plane flow angle at that station (Figure 68) reflected this behavior, showing that the flow near the surface was directed toward $z/b = 0$, and the flow above $y/b = 0.12$ was directed toward $z/b = 1.0$. This behavior suggests the existence of a clockwise-rotating (when viewed looking downstream) vortex centered at about $y/b = 0.13$ somewhere between $z/b = 0.5$ and $z/b = 1.0$.

On the other side of the centerline, at $z/b = 0.3$ (Figures 60 and 66), the near-surface flow was similarly deflected toward the centerline when the blowing was off. Although \bar{w} did not conclusively change sign within the measurement region, its profile did exhibit local maximums and minimums like those observed at $z/b = 0.7$. If the flow angles measured at $z/b = 0.3$ were shifted by $+25^\circ$, the flow angle profile would resemble the mirror image of that measured at $z/b = 0.7$. The flow angle and spanwise velocity profiles would change sign between $y/b = 0.3$ and $y/b = 0.4$. This suggests the existence of a counterclockwise vortex on the $z/b < 0.5$ side of the duct, with its axis angled slightly towards the centerline.

Data from the centerline of the exit plane (Figures 61 and 67) indicated the presence of a counterclockwise vortex even more clearly. Near the surface, \bar{w} was

positive and the flow was deflected slightly towards the $z/b = 1.0$ sidewall. At $y/b = 0.35$, the profiles changed sign and the spanwise flow component was now directed towards $z/b = 0$. Thus, when the blowing was off, there were two counterrotating streamwise vortices present at the exit plane: one clockwise-rotating vortex centered low in the boundary layer nearest the $z/b = 1.0$ sidewall, the other counterclockwise-rotating and centered on the other side of the centerline and higher above the diffuser floor. Based on the relative magnitudes of the flow angles these structures produced, the clockwise vortex appeared stronger but the counterclockwise vortex appeared to influence more of the cross-section.

Other researchers have documented the existence of a pair of counter-rotating vortices embedded in the flow near the lower surface of a diffusing S-duct (Wellborn et al., 1992, Bansod and Bradshaw, 1972; Vakili et al., 1987; Tindell, 1987). These vortices are formed by the secondary flows generated in the first bend; they convect fluid along the lower surface toward the centerline before lifting it away from the surface and turning it back outboard. Based on the above interpretation of the limited flow angularity data available from this test, this test diffuser also contained a similar pair of counterrotating vortices when VGJs were not used for control of the lower surface boundary layer.

Activation of the VGJs effectively eliminated this structure at the exit plane and replaced it with a pair of vortices of opposite rotation to those which existed with the blowing off. At $z/b = 0.3$ (Figures 63 and 69), the flow was directed toward the $z/b = 0$ sidewall below $y/b = 0.28$. This was consistent with the results from surface flow visualization. Above $y/b = 0.28$, \bar{w} changed sign and the flow angle pointed toward the

center of the diffuser. This pattern is characteristic of a clockwise-rotating vortex, as opposed to the counterclockwise vortex which existed in that area of the diffuser with the blowing off. At $z/b = 0.7$ (Figures 65 and 71), the surface flow angle pointed toward $z/b = 1.0$. The xy -plane flow angle changed sign at about $y/b = 0.35$ and faced toward the center of the section above that point. This suggests the existence of a counterclockwise vortex in that area of the exit plane, again opposite in rotation to the one which existed there without blowing. The flow angle did not go to zero at the edge of the boundary layer (approximately $y/b = 0.5$) but maintained a small deflection towards the center of the section.

The near-surface segment of the xy -plane flow angle profile at the centerline (Figure 70) appeared to be influenced by the counterclockwise vortex, but here too the flow remained deflected toward the $z/b = 0$ sidewall near the edge of the boundary layer.

While the flow angularity data at the exit plane with the blowing on is not sufficient to determine conclusively the relative orientation of the vortices at that point, it can be construed to support one possible arrangement which is compatible with both VGJ experience and other behavior observed during this experiment. Recall from Chapter 2 that VGJs generate vortices through entrainment of adjacent fluid, and that the vortex on the freestream side of the canted jet becomes dominant. In this installation, the jets were canted toward the $z/b = 0$ sidewall, and the dominant vortex would then rotate clockwise. Formation of such a structure inside the test diffuser would tend to sweep low-momentum fluid from the lower surface toward the $z/b = 0$ sidewall, and then lift it up along that sidewall. This would then account for deflection of the lower surface streaklines toward

the $z/b = 0$ corner observed during flow visualization, and for the low-momentum region measured along that wall seen in the pitot-static data.

Recall from the total pressure profiles that the jet plume was located at approximately $y/b = 0.2$ at $z/b = 0.2$ on the exit plane, and rose to $y/b = 0.4$ at the centerline. If the clockwise-rotating vortex lifted off the surface with the jet plume, a weaker, counterrotating vortex would be likely to form from the wash of the primary vortex. Compton and Johnston (1991) observed the formation of such a secondary vortex in their study. If this process occurred in the test diffuser, the two vortices would be arranged as shown in Figure 72. The dominant clockwise vortex would be shifted up and toward the $z/b = 0$ sidewall, and the weaker counterclockwise vortex would be beneath it in the $z/b = 1.0$ corner. Such an arrangement would explain the small positive xz -plane flow angle measured near the edge of the boundary layer at $z/b = 0.5$ and $z/b = 0.7$.

Regardless of whether the above hypothesis is proved out by more detailed experiments, the data of this study showed that the use of vortex generator jets substantially altered the secondary flow structure which favored separation along the lower surface. This potential benefit is countered by the increase in the magnitude of the flow angles measured at the exit plane with blowing on. Increased and irregular flow angularity is undesirable, since the blades of a turbine engine compressor must operate at a relatively constant angle of attack to prevent stall.

Mean Velocity. While the \bar{w} data provided the most significant findings, measurement of the other components also gave some noteworthy results. The blowing-off \bar{u} data shown in Figures 60 - 62 confirmed the observations made earlier from the

total pressure profiles. In the near-wall region, \bar{u} was small but positive with the blowing off. This region, where \bar{u} was nearly constant, represented a wake trailing behind the separated flow region. The lower surface boundary layer without blowing extended to approximately $y/b = 0.5$ - half the height of the diffuser. The boundary layer thickness varied only slightly in the spanwise direction. The inflectionary nature of the boundary layer profile suggested the existence of an adverse pressure gradient even at the exit plane, where the diverging section ended. Though the duct cross section was constant downstream of the exit plane, the wake behind the separated flow region dissipated as it moved downstream, opening more of the cross-sectional area to high-momentum flow and allowing more diffusion.

The blowing-on data for \bar{u} (Figures 63 - 65) also confirmed observations made earlier. With the VGJs operating, the lower surface boundary layer thickness was a function of spanwise position. It was thinnest at the centerline, thickened gradually toward the $z/b = 1.0$ sidewall, and thickened more rapidly toward the $z/b = 0.0$ sidewall. The boundary layer profile for $z/b = 0.3$ displayed a local velocity maximum near the lower surface, where the presence of the jet plume was discernible. Above the plume, \bar{u} decreased to a value less than that measured at the same station with the blowing off before increasing again.

The \bar{v} component of velocity was only slightly altered by operation of the VGJs. At all conditions, there was a small downward component of velocity resulting from the

curvature of the duct and the reattachment of the flow. As the separated-flow region ended, flow from above the separation bubble moved down to the surface.

Each figure displays two sets of \bar{u} data - one from the uv-film probe, and one from the uw-film probe. Generally, the data sets agree very well and the individual traces are not discernible. However, between $y/b = 0.125$ and $y/b = 0.5$ on Figure 64, the two traces gave values for \bar{u} differing by up to 20 m/s. Since the jet plume crossed the exit plane in this region, and the data sets agreed well above and below this region, the discrepancy is attributed to a small difference in blowing mass flow rate between the two runs. As stated in Chapter 3, the air supply pressure occasionally varied a small amount. Changes in supply pressure fed directly into the blowing plenum pressure and affected the blowing flow rate. Results of a test of hot-film repeatability are contained in Appendix C.

Mean flow measurements showed that the vortex generator jets induced major changes in the structure of the primary and secondary mean flows. While the changes generally resulted in improvements in the bulk measures of diffuser performance, they increased the distortion of the total pressure, static pressure, and flow angle fields at the exit plane.

Turbulent Flow Properties

As the mean flow analysis considered the steady-state distortion of the exit plane flowfield, measurement of the turbulent properties determined the time-dependent

distortion of the flowfield and quantified the energy lost to random motion and increased shear stress.

Turbulence Intensity. Turbulence intensity was measured at three spanwise stations on the diffuser exit plane. Comparison of data collected for the blowing-off and blowing-on cases showed that blowing significantly reduced the level of turbulence in the flow at the exit plane.

Figures 73 - 75 show the three components of turbulence intensity measured at each spanwise station by cross-film probes without blowing. Figures 76 - 77 show the single component of turbulence intensity measured by the normal-film probe at the same conditions. In each set, the local mean velocity component \bar{u} is used as the nondimensionalizing parameter.

The cross-wire data shows that the u'_{rms} component was the largest, but that v'_{rms} and w'_{rms} were significant. As expected, u'_{rms} and v'_{rms} were decreasing over the last few measurement stations approaching the wall. Somewhere near the middle of the exit plane boundary layer, u'_{rms} and v'_{rms} reached a maximum value. At its maximum, u'_{rms} was equal to nearly 40% of the mean component, \bar{u} . The fluctuating component v'_{rms} reached a maximum value of nearly 30% of \bar{u} . Inspection of the data for \bar{u} and \bar{v} from Figures 60 - 62 showed that \bar{v} was never as large as 30% of \bar{u} , so at its maximum v'_{rms} exceeded \bar{v} . The magnitude of w'_{rms} was only slightly less substantial, reaching to about 25% of \bar{u} at its maximum near the lower surface. At the edge of the boundary layer,

known to be near $y/b = 0.5$ from the mean flow analysis, all three components of turbulence intensity converged to a freestream value between 0.05 and 0.10.

Figures 76 - 77 show the streamwise turbulence intensity measured by the normal-film probe at the same operating conditions. They are included for comparison only, since this was a measure of the turbulence intensity in a direction defined by the local flow angle in the xy -plane. Mean flow data showed that the z -component of velocity was non-negligible at the exit plane. The turbulence intensity profile computed from normal-film data was similar in shape to that measured by the cross-film probes, though the magnitude was greater. The increased magnitude was expected because this type of probe sensed the vector sum of the u'_{rms} and v'_{rms} components measured by the cross-wire probe.

Figures 78 - 80 show the turbulence intensity profiles measured for $\frac{\dot{m}_j}{\dot{m}_d} = 0.0048$.

Blowing reduced the maximum value of each component of turbulence intensity, and the shape of the turbulence intensity profiles varied with spanwise position. At $z/b = 0.3$ (Figure 78), maximum values of turbulence intensity were measured around $y/b = 0.4$, far above the lower surface but in the region of low momentum fluid documented in the mean flow analysis. The maximum value of u'_{rms} was about 25% of \bar{u} . At the centerline (Figure 79), where the boundary layer profile was the fullest, all components of turbulence intensity were nearly equal. The maximum value was less than 0.20. At $z/b = 0.7$ (Figure 80), the turbulence profile looked similar to that observed in the absence of blowing, but the peak magnitude of u'_{rms} was reduced to 30% of \bar{u} .

Part of the apparent reduction in turbulence intensity with the blowing on was due to the increased mean velocity at that condition. The local mean velocity was chosen as the nondimensionalizing quantity so that turbulence intensity would be a measure of the magnitude of the local fluctuation velocity component relative to the local mean velocity component. While this was useful, \bar{u} changed across the boundary layer, making it difficult to determine the behavior of the fluctuating components themselves. Turbulence intensity can also be defined as nondimensionalized by some reference velocity; the freestream velocity is commonly used. For comparison, Figures 81 and 82 show the turbulence intensity nondimensionalized by the inlet plane freestream velocity at $z/b = 0.5$ with the blowing off and on. Figure 81 shows one significant feature which was misrepresented by the initial choice of a nondimensionalizing quantity - the maximum value of w'_{rms} occurred at the same vertical position as the maximums for u'_{rms} and v'_{rms} rather than adjacent to the surface as previously suggested. The maximum values were measured almost exactly at the midpoint of the boundary layer. Each fluctuation component dropped off rapidly towards the wall. The blowing-on profile did not change significantly when nondimensionalized in this way. With either choice of a nondimensionalizing parameter, blowing significantly reduced turbulence intensity.

Turbulent Kinetic Energy. Turbulent kinetic energy is a measure of the kinetic energy of the turbulent fluctuations; it represents energy which is lost from the mean flow. When nondimensionalized by \bar{u}^2 , it represents the ratio of the kinetic energy in the local turbulent motion to the kinetic energy of the local downstream mean motion. Comparison

of blowing-on and blowing-off data showed that activation of the VGJs reduced turbulent kinetic energy by 6% to 10%, implying that blowing reduced energy losses and increased the efficiency of the flow process in the diffuser.

Figures 83 - 85 show profiles of turbulent kinetic energy computed from the measured fluctuation velocity components with the blowing on and off. At the edge of the boundary layer, where the fluctuation velocities were small, the energy drained by the turbulence is less than 1% of that held in the flow. With the blowing off, this value increased as the lower surface was approached. It reached a maximum of 12% to 14% of the directed energy around $y/b = 0.15$, then decreased as the fluctuations diminished near the wall. Like the turbulence intensity profiles, the turbulent kinetic energy profiles with the blowing off were relatively independent of spanwise location.

With the blowing on, the turbulent kinetic energy became more dependent upon spanwise position. At $z/b = 0.3$, turbulent kinetic energy was at its maximum relative to the local mean velocity in the low-momentum region above the jet plume. At stations nearer the wall, blowing reduced the turbulent kinetic energy by 8%. At $z/b = 0.5$, the freestream level of turbulent kinetic energy was retained much closer to the wall than for the blowing- off case, and the maximum value measured was 3% of the local mean flow kinetic energy, as opposed to 13% without blowing. At $z/b = 0.7$, the blowing-on turbulent kinetic energy profile was of similar shape to that measured with the blowing off, though the value of the turbulent kinetic energy was typically 6% to 8% less.

To investigate the effect the choice of the nondimensionalizing parameter had on the comparison of blowing on and blowing off values of turbulent kinetic energy, the

centerline data was again replotted with the freestream velocity as the nondimensionalizing quantity (Figure 86). The plot showed that a true reduction in turbulent kinetic energy was attained by blowing.

Turbulent Shear Stress. Values for the $\overline{u'v'}$ and $\overline{u'w'}$ components of turbulent shear stress were computed from measured quantities. This data showed that activation of the VGJs decreased the magnitude of the turbulent shear stress, again indicating that blowing reduced losses and improved the efficiency of the flow process in the diffuser.

Blowing-off data (Figures 87 - 89) showed that the turbulent shear stresses were near zero at the outer edge of the boundary layer. They increased to a maximum near $y/b = 0.2$, then decreased toward zero approaching the lower surface. The $\overline{u'v'}$ term was definitely dominant, but the $\overline{u'w'}$ term was of the same order of magnitude when it was at its maximum. This is not surprising, given the highly three-dimensional nature of the flow. The profiles were similar for all three spanwise stations.

With the VGJs activated, the turbulent shear stress was greatly reduced but the profiles became more dependent upon spanwise position. The maximum value for the $\overline{u'v'}$ term decreased from around -0.08 to -0.02 at $z/b = 0.3$ (Figure 90). The $\overline{u'w'}$ term was of the same order of magnitude as the $\overline{u'v'}$ term throughout the boundary layer at that spanwise location. At the centerline station (Figure 91), blowing nearly eliminated the turbulent shear stresses; the $\overline{u'v'}$ term became significant only at $y/b < 0.1$. At $z/b = 0.7$ (Figure 92), the profiles retained some of the characteristic shape seen without blowing,

but the y-position where they became measurable decreased from $y/b = 0.45$ to $y/b = 0.3$, indicative of a thinner boundary layer. The maximum magnitude of the $\overline{u'v'}$ term decreased from -0.9 to -0.4. At this station, the $\overline{u'w'}$ term was not negligible when the blowing was on.

As seen for the turbulence intensity and turbulent kinetic energy data, nondimensionalizing the turbulent shear stress with the freestream velocity (Figures 93 and 94) altered the shape of the profiles slightly, but the magnitude of the turbulent shear stress components was still reduced with blowing on.

From the data discussed here, it appears that activation of the VGJs reduced the magnitude of the turbulent velocity fluctuations in the diffuser. Less energy was lost to turbulent shear or turbulent kinetic energy, improving the efficiency of the diffusion process. With respect to the level of turbulence at the exit plane and the turbulent losses incurred during the diffusion process, VGJs definitely improved the performance of this highly-offset diffuser.

V. CONCLUSIONS AND RECOMMENDATIONS

Conclusions

The following conclusions resulted from this study of the performance of a highly-offset diffuser with and without boundary layer control by means of blowing vortex generator jets.

1. The lower surface boundary layer in the baseline diffuser without blowing was massively separated over most of the length of the diffusing section. Strong secondary flows and a strong local adverse pressure gradient produced by the curvature of the diffuser surfaces combined to create conditions favorable for flow separation along the lower surface of the diffuser. The lower surface boundary layer occupied nearly half of the duct cross section at the exit plane. Diffuser performance, as characterized by total pressure recovery and static pressure coefficient, suffered as a result. A significant amount of energy was lost to turbulence. This conclusion was substantiated by observations from surface flow visualization and from measured static pressure, total pressure, and turbulence data.
2. The use of blowing vortex generator jets for boundary layer control on the lower surface of the diffuser with a blowing mass flow rate equal to 0.48% of the diffuser inlet mass flow rate resulted in improved overall performance. The static pressure coefficient increased 50% from the value measured without blowing, while face-averaged pressure recovery increased 1.3% and the diffuser isentropic efficiency increased 8.22%.

The extent of the separated flow region on the lower surface decreased, and the surface flow patterns were altered so that most reversed flow was eliminated. The exit plane boundary layer thickness was reduced at most locations, particularly near the centerline.

3. With the vortex generator jets operating, low-momentum fluid accumulated near the sidewall towards which the jets were canted. The momentum of the fluid on the other side of the diffuser was increased over measurements taken without blowing. This redistribution of the flow momentum resulted in increased distortion of the total pressure static pressure, and flow angle fields at the exit plane.

4. The level of turbulence present in the flow at the exit plane was reduced when the vortex generator jets were operating, particularly near the centerline. The magnitude of the turbulent velocity fluctuation components was reduced, resulting in less energy being transferred from the mean flow to the turbulent motion. A reduction in the turbulent kinetic energy accounted for some of the increase in efficiency realized when the vortex generator jets were operating. The turbulent shear stress component were found to decrease when blowing was employed. In addition, the data indicated that three-dimensional turbulence models should be used when modeling this highly non-isentropic flow.

5. Use of vortex generator jets greatly altered the structure of both the primary and secondary flows within the diffuser. The streamwise momentum distribution was altered, and the direction of rotation of the secondary flows was reversed at the exit plane. The mechanism by which the VGJs accomplished those changes was not determined.

Recommendations

While this study showed that useful performance gains could be achieved through the use of blowing vortex generator jets for boundary layer control in a highly-offset diffuser, further study is needed to optimize the implementation of such devices. Several areas are recommended for further study.

1. Characterization of the effect of blowing through jets aligned with the diffuser axis would show whether vortex generator jets produce a greater performance increase per unit blowing mass flow than more conventional blowing schemes. Data from the present study suggests so when compared to data from other studies of blowing methods in highly-offset diffusers, but geometric differences between studies makes such comparisons somewhat ambiguous.

2. Flowfield measurements taken at several axial locations between the vortex generator jets and the exit plane may allow determination of the mechanisms by which the VGJs altered the flow structure in the diffuser. If this information were known, the VGJ installation could be adjusted to produce greater improvements in the performance of the diffuser.

2. Basic research into the effect of a blowing vortex generator jet in a three-dimensional, turbulent, compressible flowfield is needed. All literature surveyed for this study concerned implementation of VGJs in two-dimensional, low-speed applications, and the results of those studies were used to select the VGJ configuration used during this

research. Values optimized for two-dimensional, low-speed flow may not provide the best results in a three-dimensional, compressible flow.

3. A parametric study encompassing multiple diffuser operating conditions and VGJ configurations would greatly increase the knowledge base for this type of flow beyond the one diffuser inlet condition and one VGJ orientation considered during this test.

4. A study of the influence of vortex generator jets on the flow in a highly-offset diffuser of circular cross-section would provide valuable information. Most aircraft inlet diffusers transition to a circular cross-section before the exit plane, so data from such a study would be more realistic. In the current study, it remained undetermined whether the accumulation of fluid along one sidewall resulted from jet impingement on the sidewall causing its boundary layer to separate, or by a rotational flow established by the VGJs. This problem would be avoided in a circular cross-section duct. Also, more data is available in the literature for circular ducts, giving a wider base of comparison and experience from which to draw.

5. The secondary flows produced in a highly-offset diffuser appeared to be a significant factor behind the losses incurred in such a duct. A study employing a boundary layer control scheme designed specifically to nullify the secondary flow may produce outstanding results for very little energy input, if such a scheme can be devised.

6. It is important that VGJs be placed upstream of the flow separation point. An analytical study which tested the accuracy of several flow separation prediction methods when applied to a highly-offset diffuser would be of some value. If a reliable, accurate method were found, the design process would be accelerated since the separation point would not have to be determined experimentally before placing the VGJs.

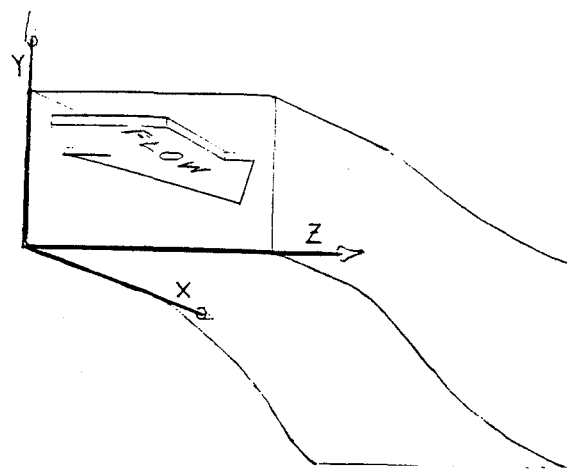


Figure 1. Coordinate System With Respect to Diffuser

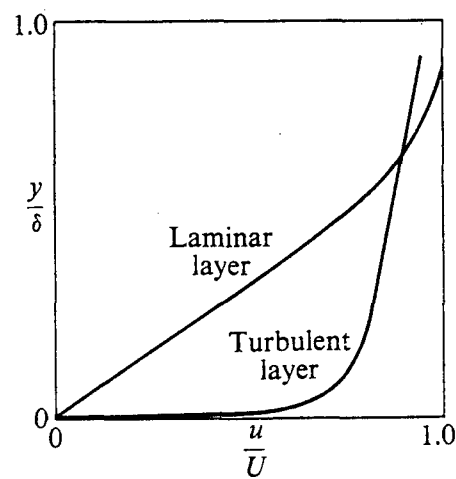


Figure 2. Laminar and Turbulent Boundary Layer Profiles (Hill and Peterson, 1992:100)

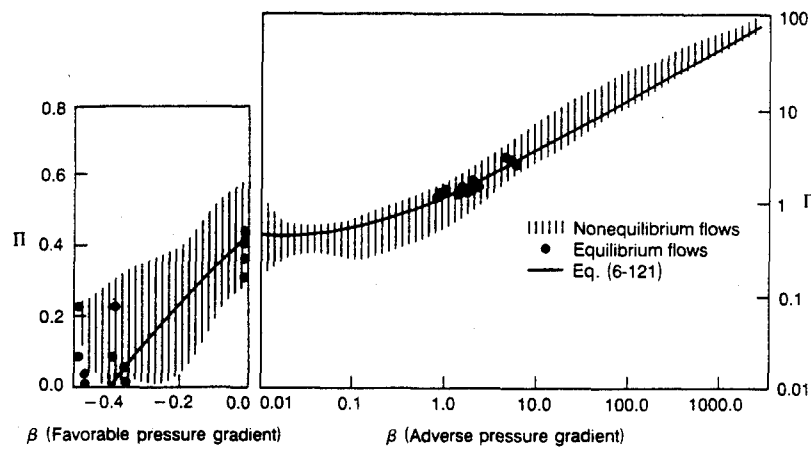


Figure 3. Coles' Law of the Wake Parameter Π (White, 1991:452)

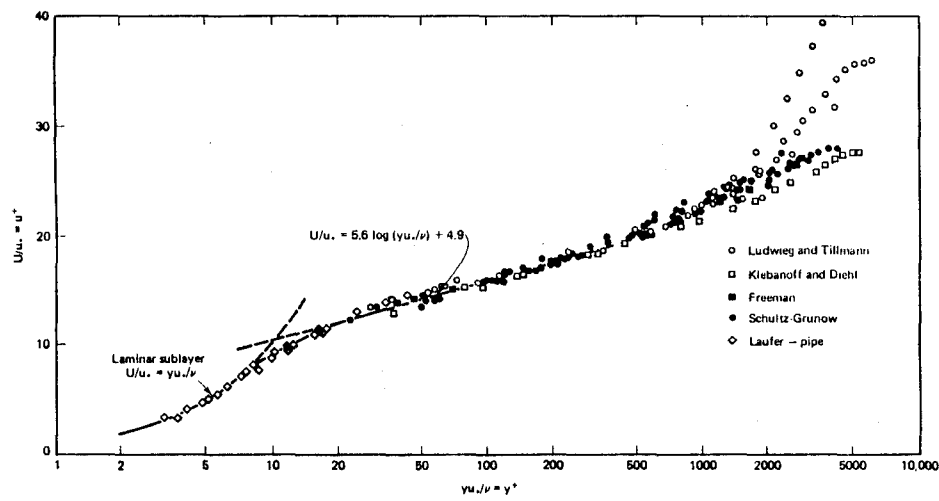


Figure 4. Law of the Wall Velocity Profile (Schetz, 1993:209)

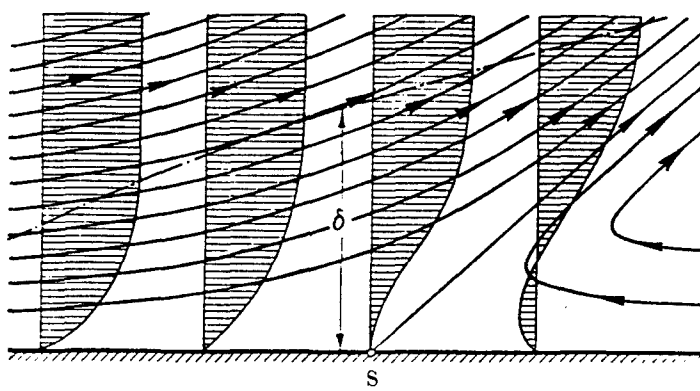


Figure 5. Boundary Layer Growth to Separation (Schlichting, 1951:34)

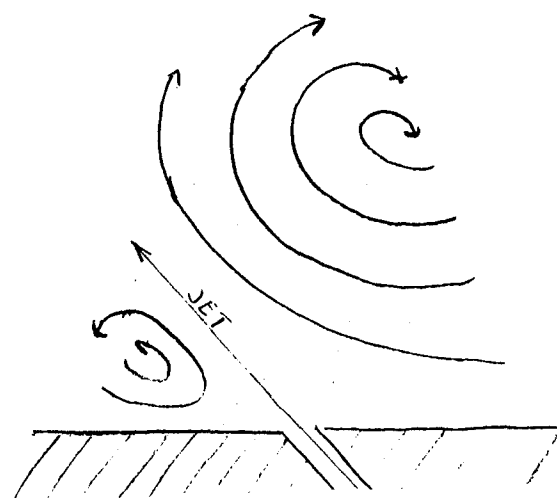


Figure 6. Jet-Induced Vortices (after Zhang and Collins, 1993)

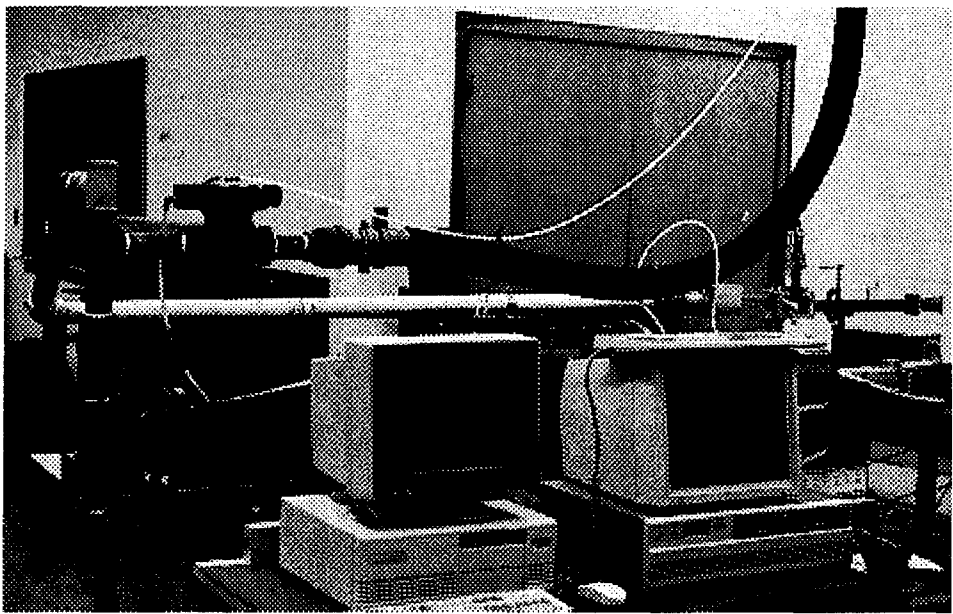


Figure 7. AFIT Subsonic Diffuser Test Facility

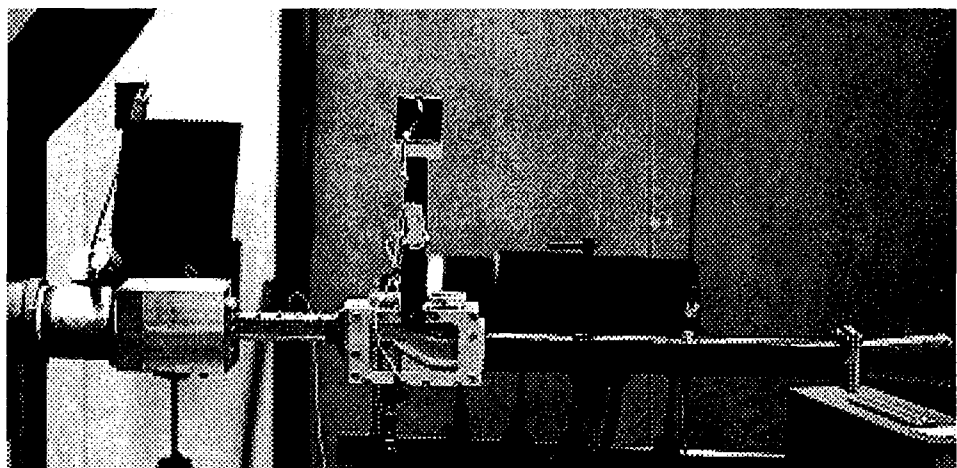


Figure 8. Diffuser Installed in Test Facility

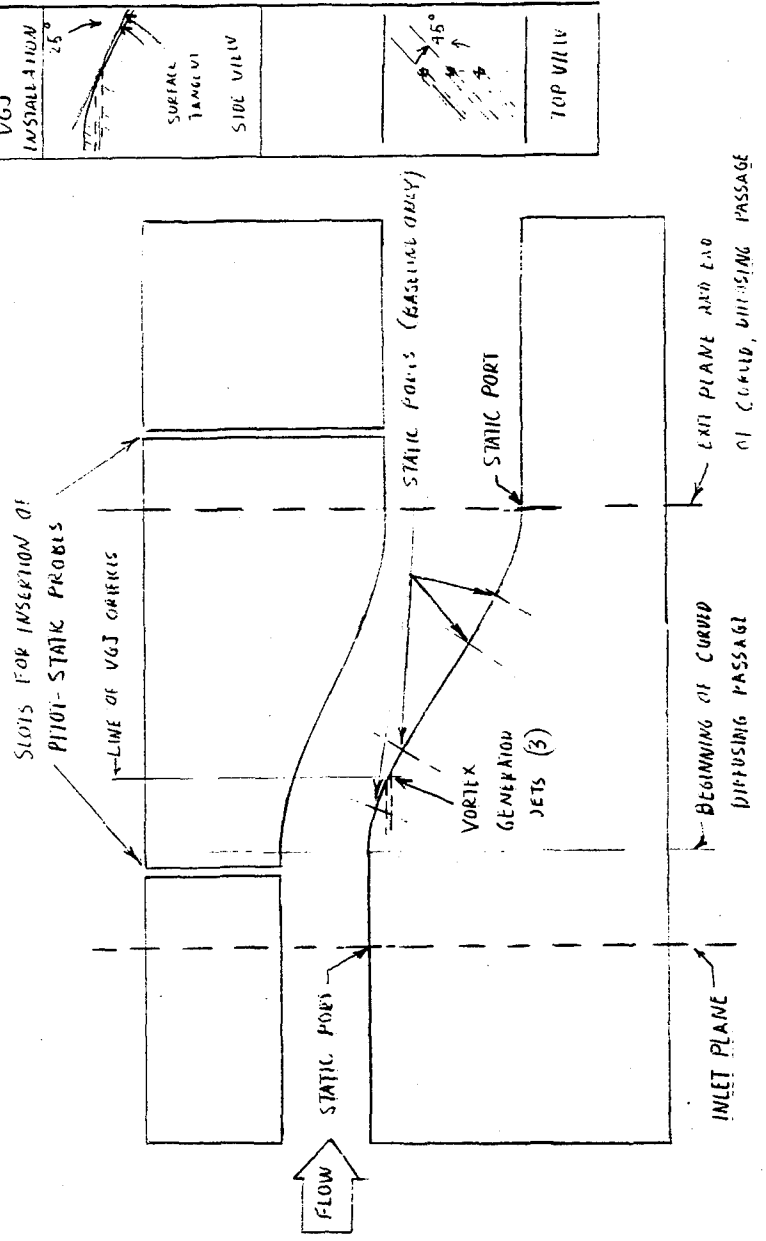


Figure 9. Diffuser Flowpath Details

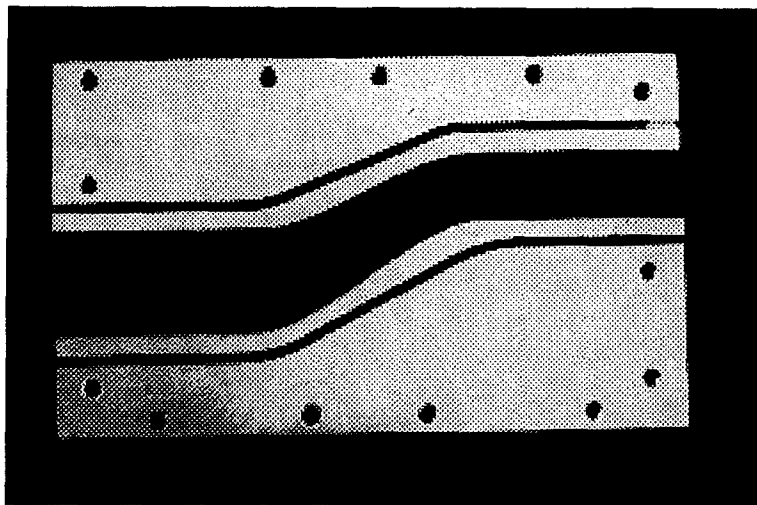


Figure 10. Test Section Upper and Lower Surfaces

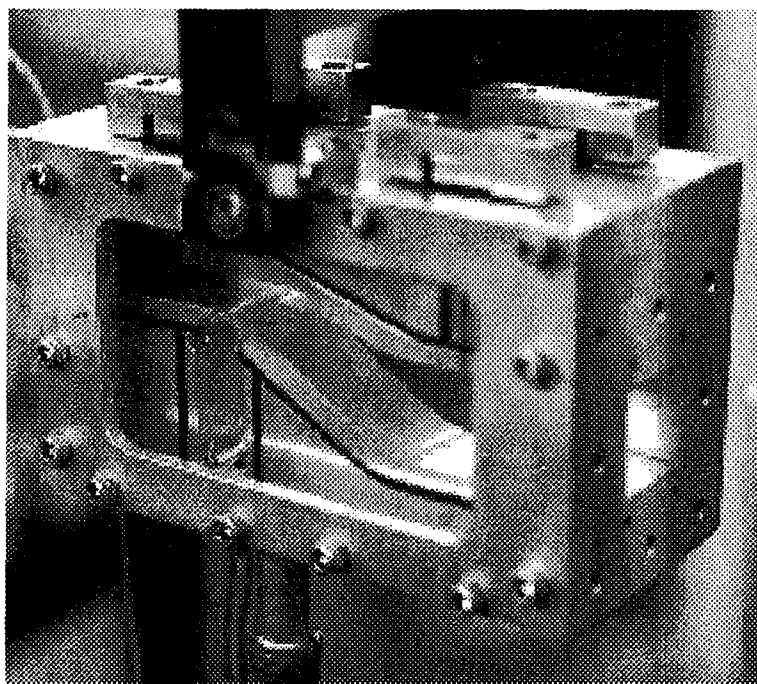


Figure 11. Assembled Test Section

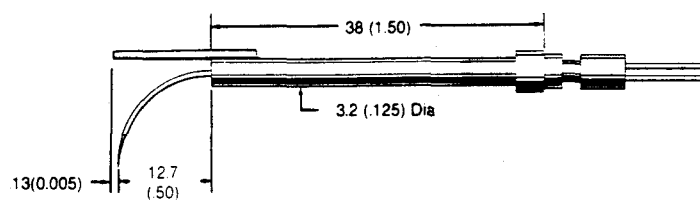


Figure 12. TSI Model 1218 Normal-Film Probe (TSI, 1987)

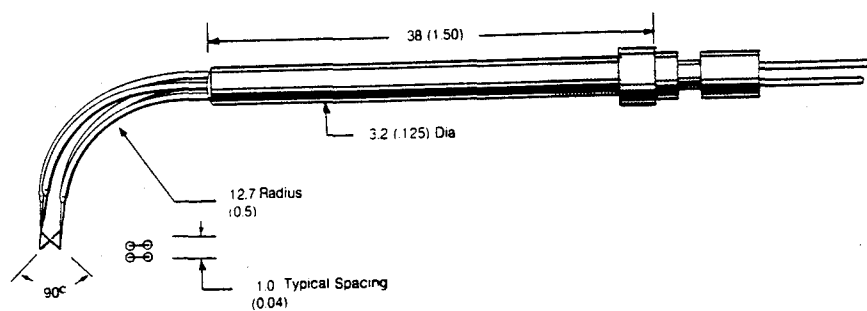


Figure 13. TSI Model 1243 Cross-Film Probe (TSI, 1987)

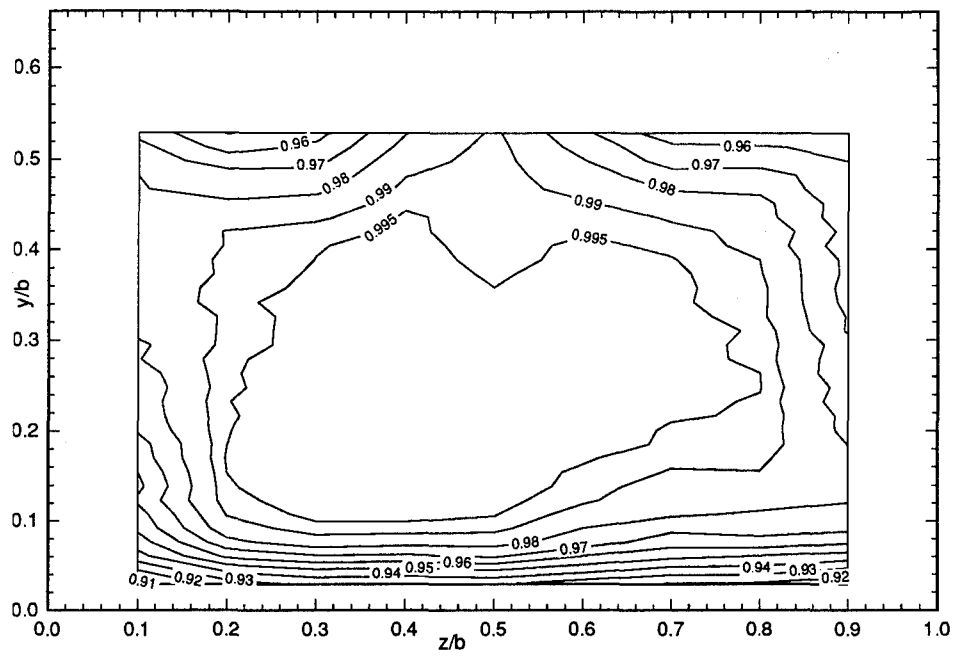


Figure 14. $M_1 = 0.6$ Inlet Plane Total Pressure Recovery Map

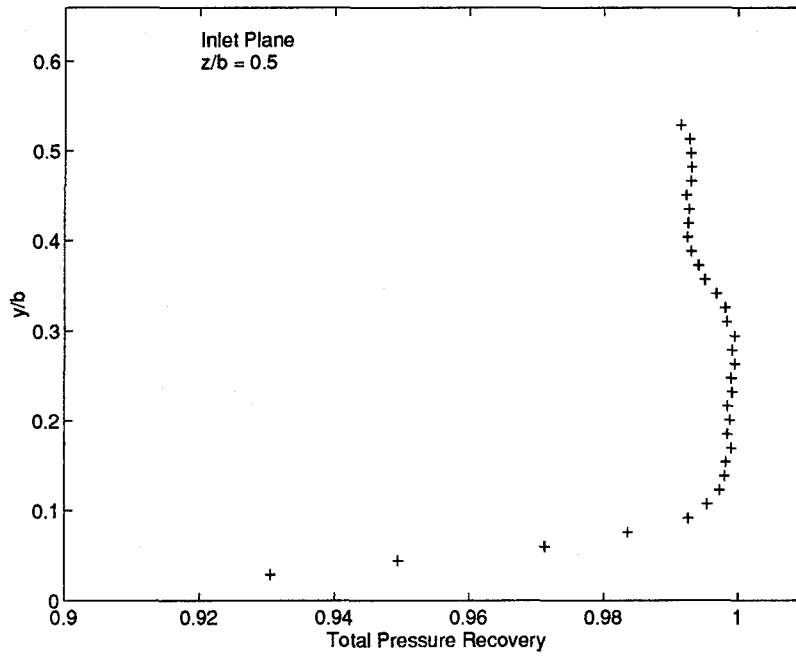


Figure 15. $M_1 = 0.6$ Inlet Plane Total Pressure Recovery Profile @ $z/b = 0.5$

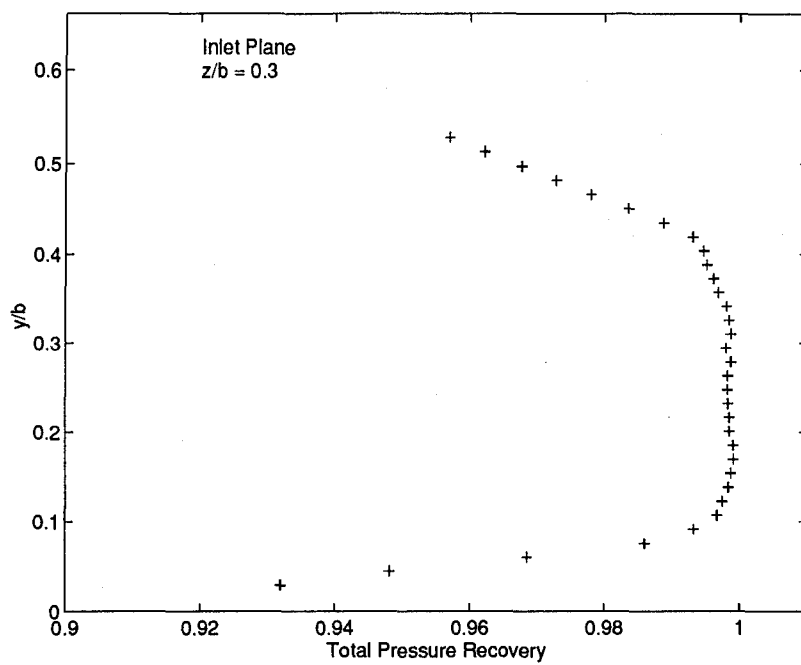


Figure 16. $M_1 = 0.6$ Inlet Plane Total Pressure Recovery Profile @ $z/b = 0.3$

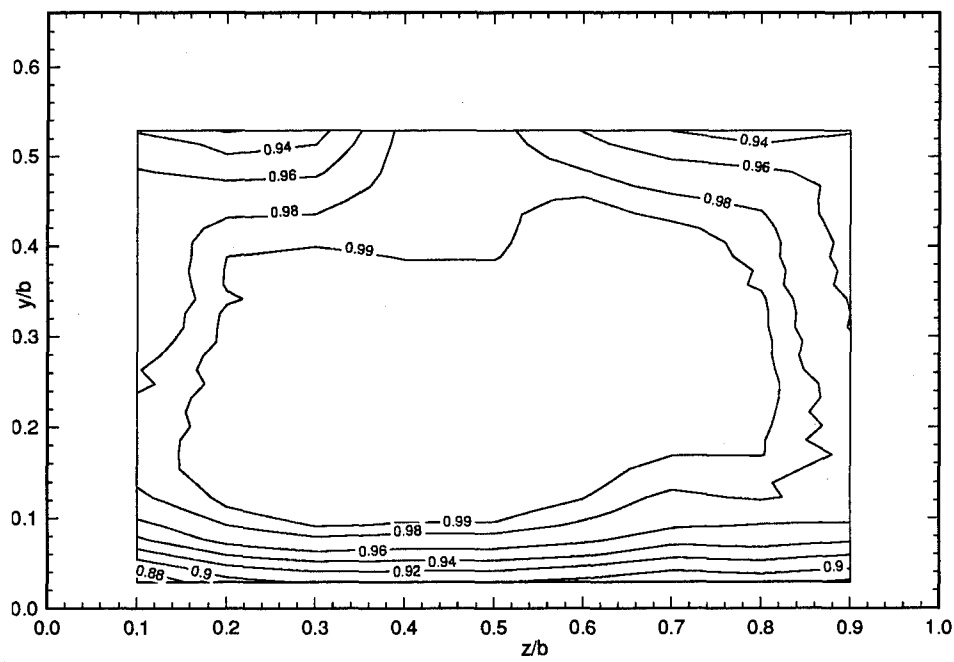


Figure 17. $M_1 = 0.8$ Inlet Plane Total Pressure Recovery Map

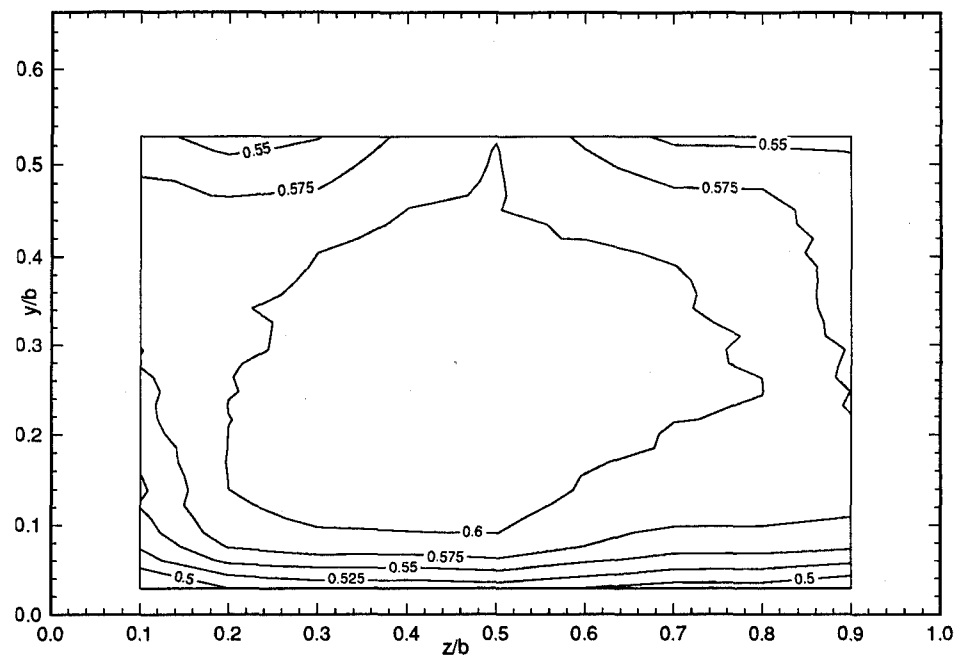


Figure 18. $M_1 = 0.6$ Inlet Plane Mach Number Map

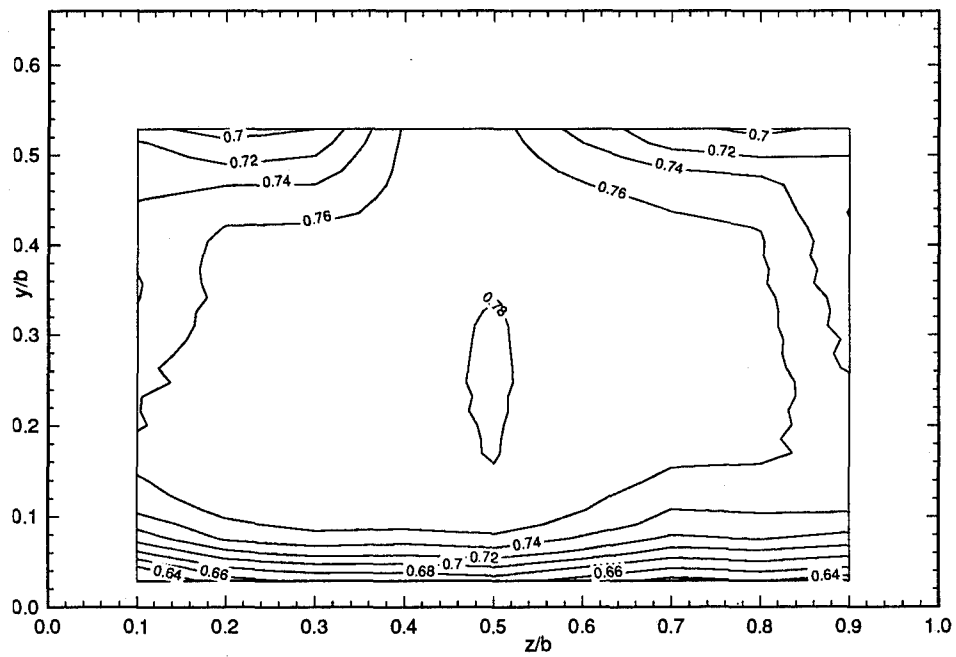


Figure 19. $M_1 = 0.8$ Inlet Plane Mach Number Map

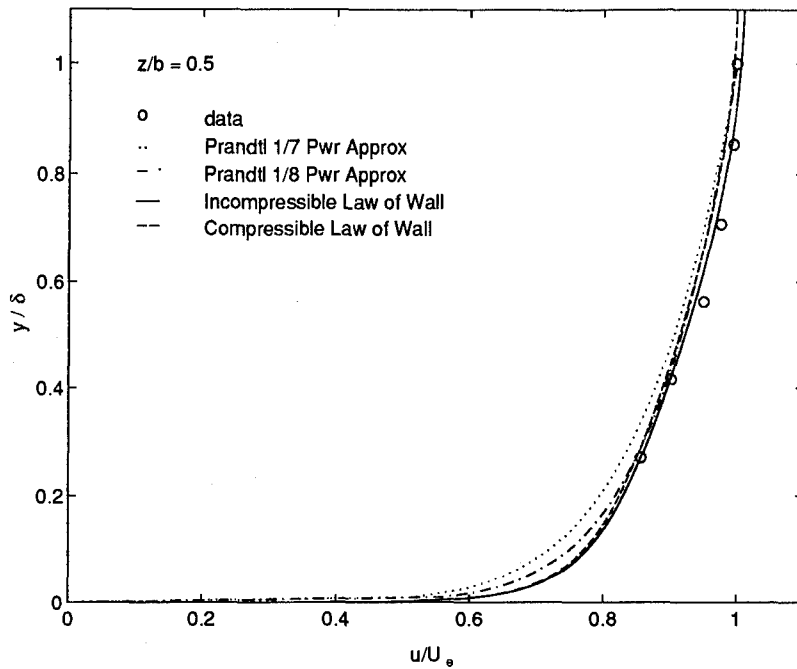


Figure 20. $M_1 = 0.6$ Inlet Plane Lower Surface $\frac{y}{\delta}$ vs $\frac{\bar{u}}{U_e}$ @ $z/b = 0.5$

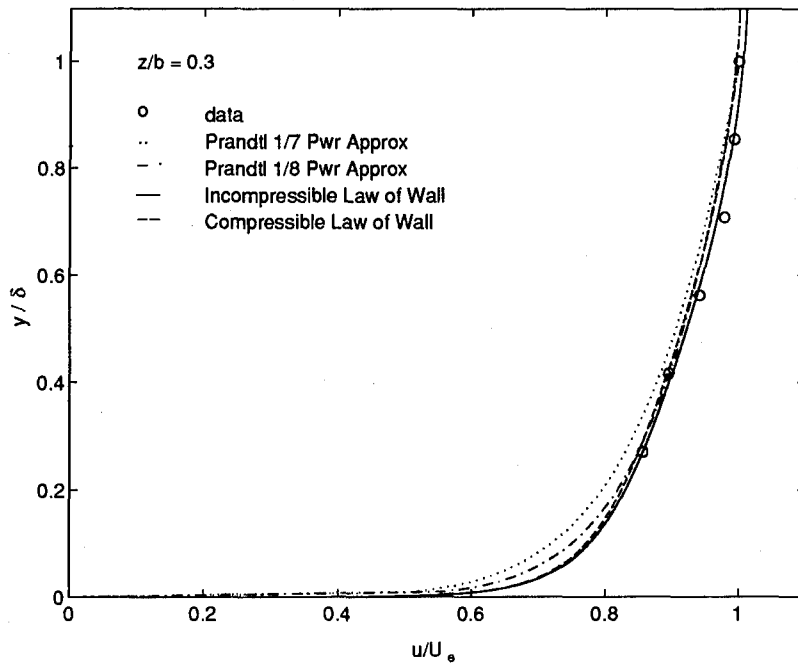


Figure 21. $M_1 = 0.6$ Inlet Plane Lower Surface $\frac{y}{\delta}$ vs $\frac{\bar{u}}{U_e}$ @ $z/b = 0.3$

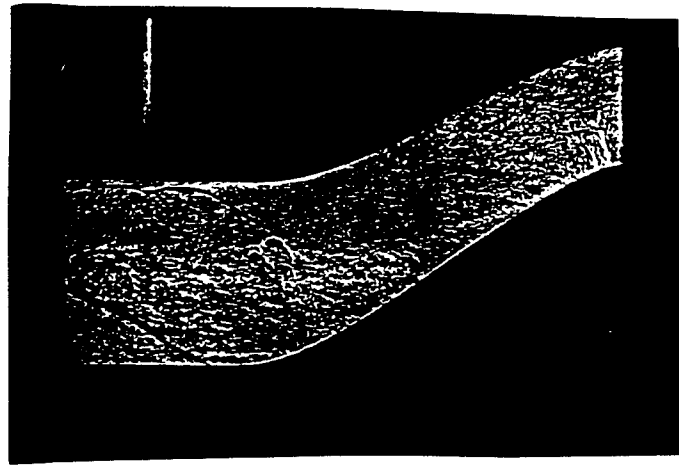


Figure 22. $M_1 = 0.8$ Shadowgraph

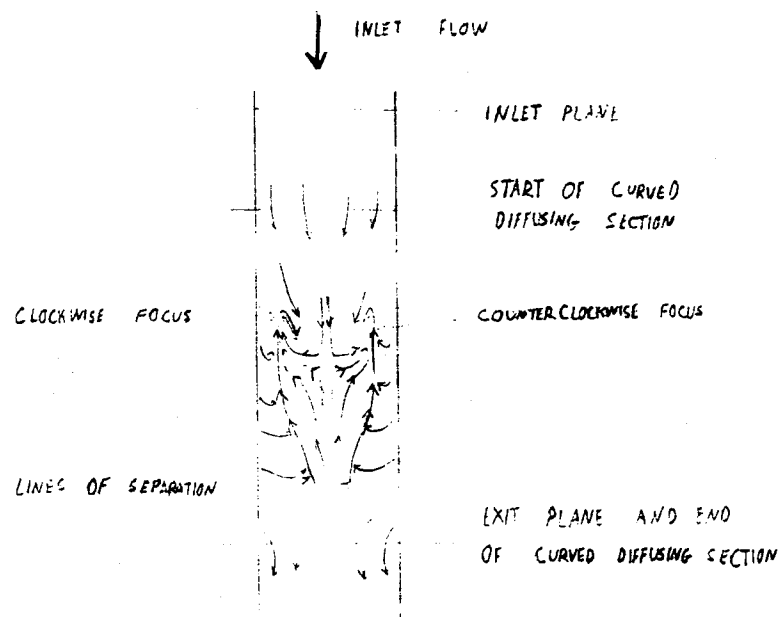


Figure 23. Sketch of Lower Surface Flow Pattern Without Blowing

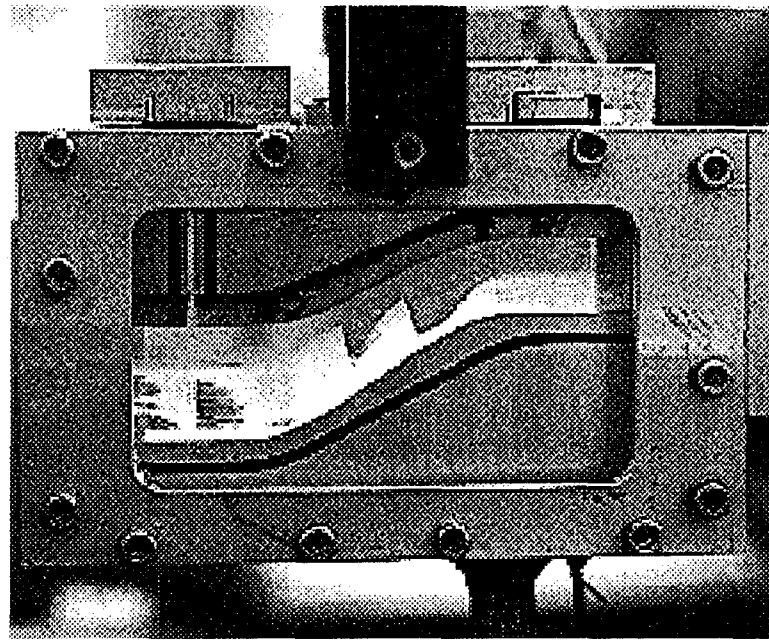


Figure 24. Photograph of Sidewall Streaklines Showing Secondary Flow Direction

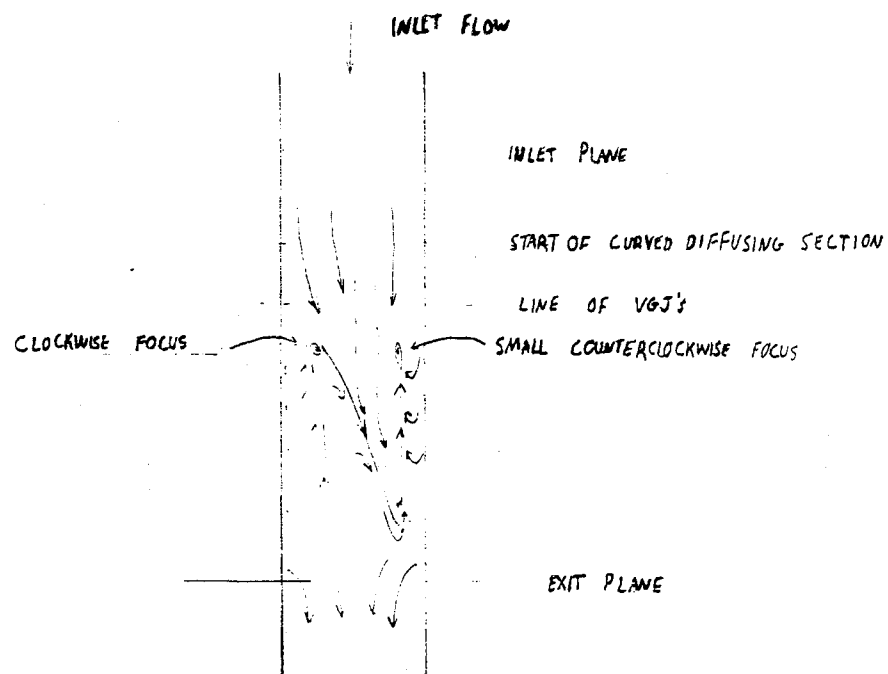


Figure 25. Sketch of Lower Surface Flow Pattern at $\frac{m_j}{m_d} = 0.0025$

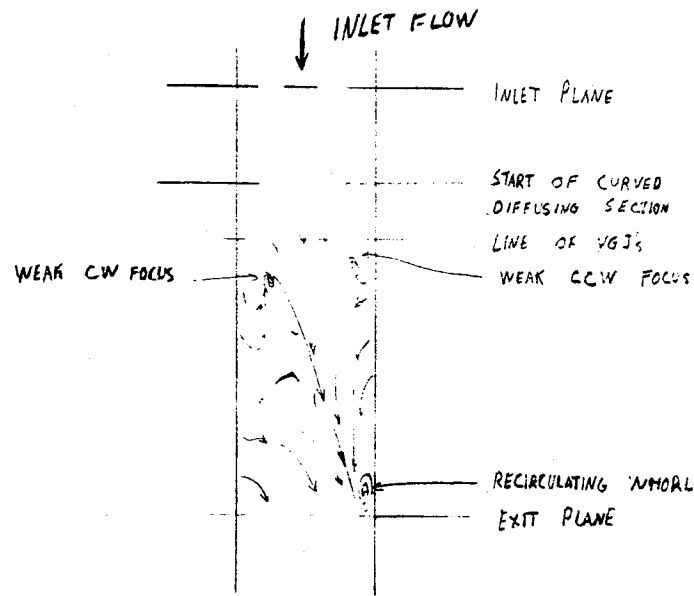


Figure 26. Sketch of Lower Surface Flow Pattern at $\frac{\dot{m}_j}{\dot{m}_d} = 0.0048$

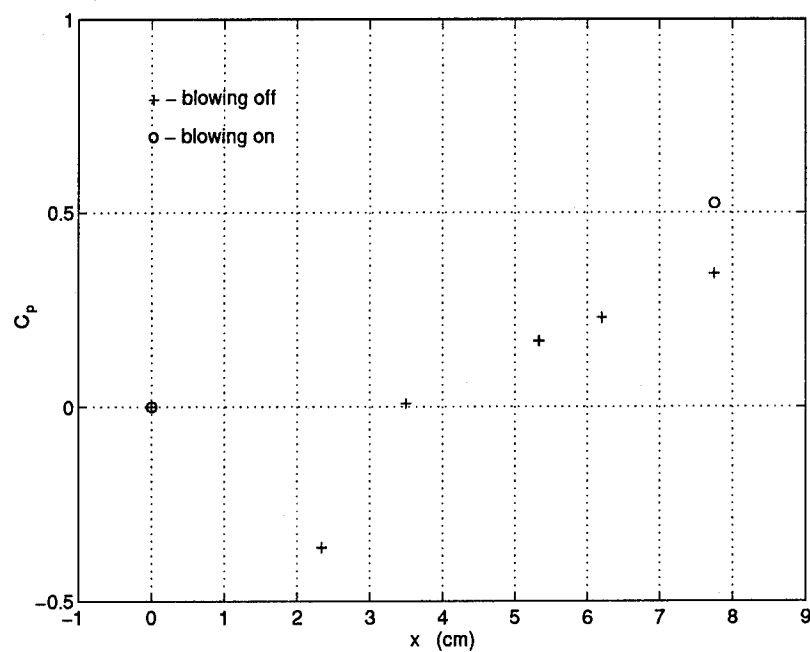


Figure 27. Lower Surface Static Pressure Coefficient vs x

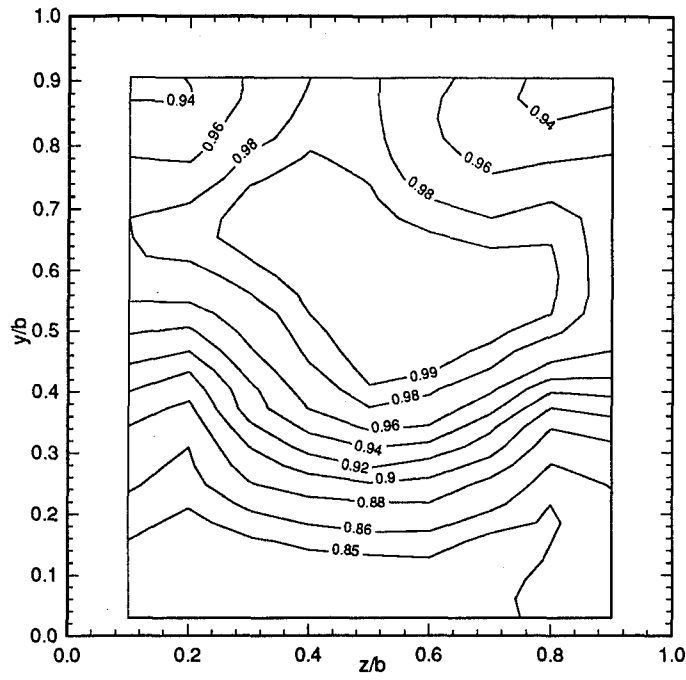


Figure 28. $M_1 = 0.6$ Exit Plane Total Pressure Recovery Map with Blowing Off

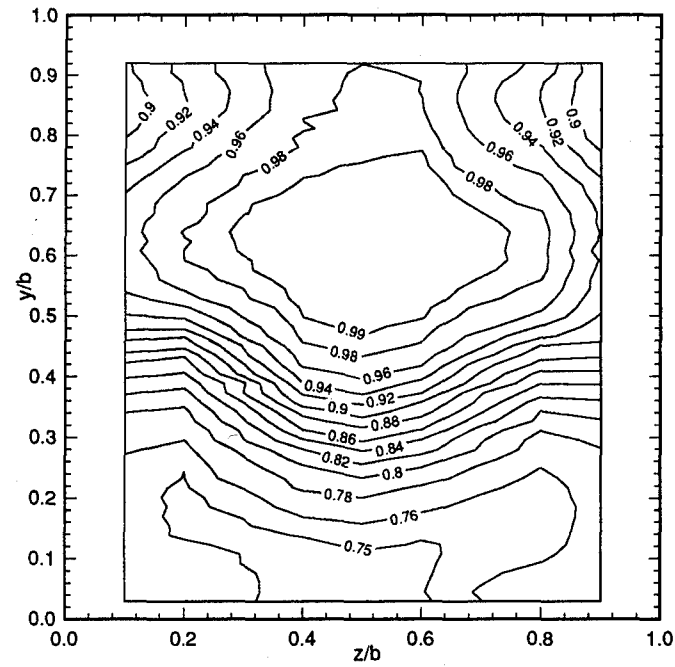


Figure 29. $M_1 = 0.8$ Exit Plane Total Pressure Recovery Map with Blowing Off

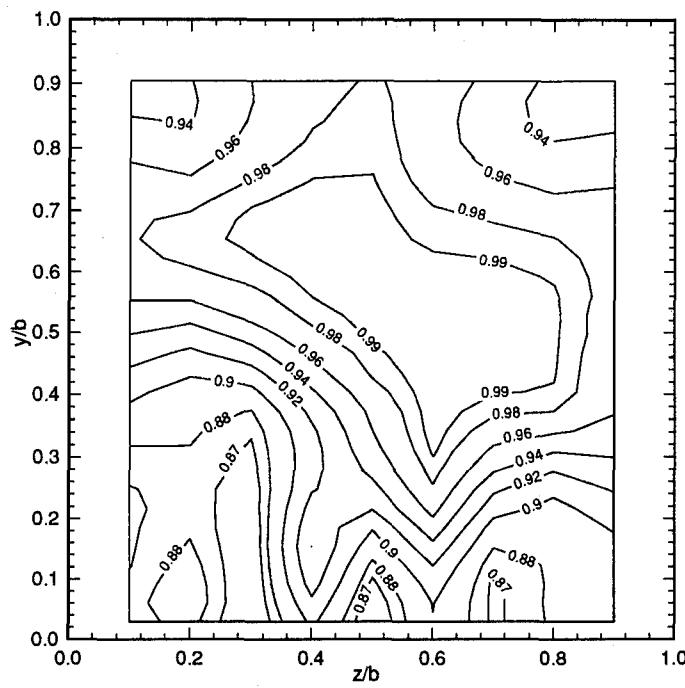


Figure 30. $M_1 = 0.6$ Exit Plane Total Pressure Recovery Map with $\frac{\dot{m}_j}{\dot{m}_d} = 0.0048$

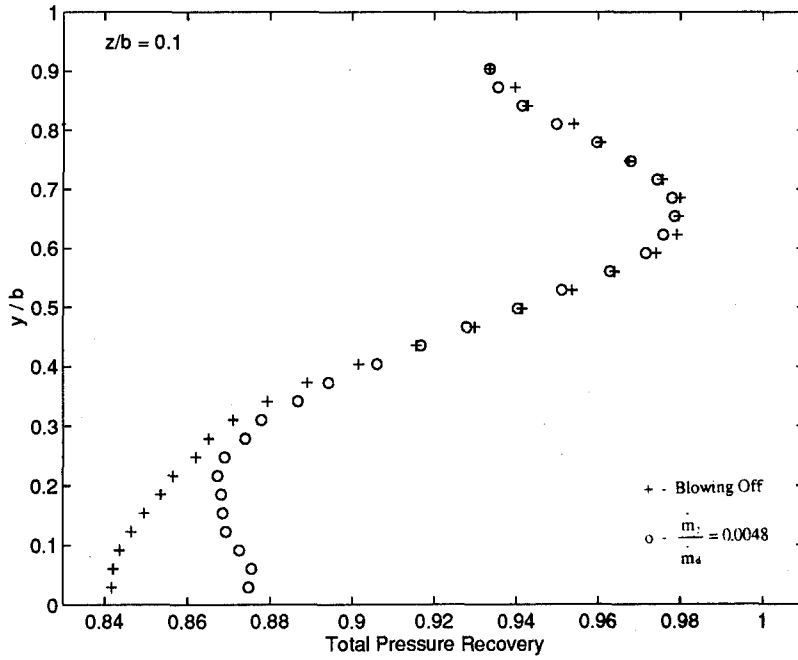


Figure 31. Total Pressure Recovery Profiles @ $z/b = 0.1$

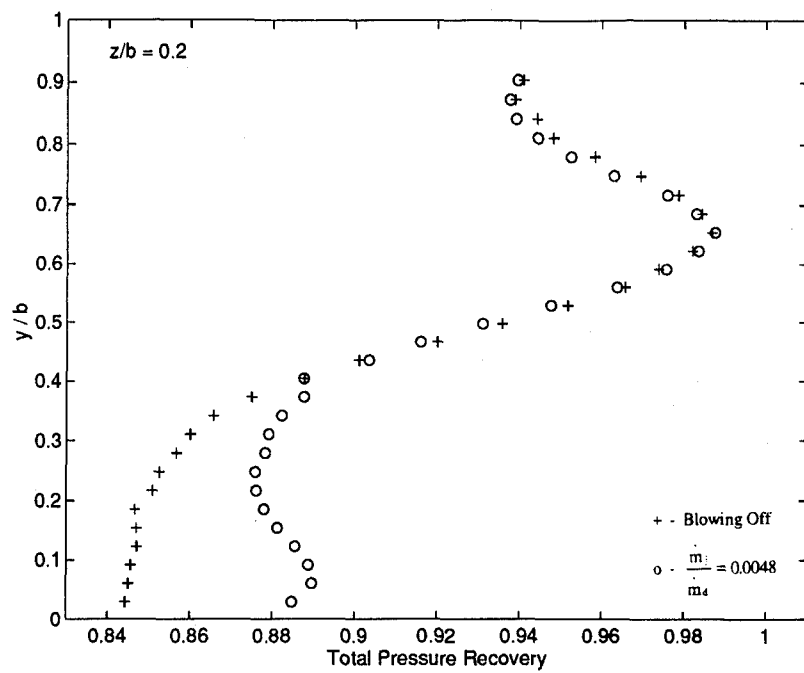


Figure 32. Total Pressure Recovery Profiles @ $z/b = 0.2$

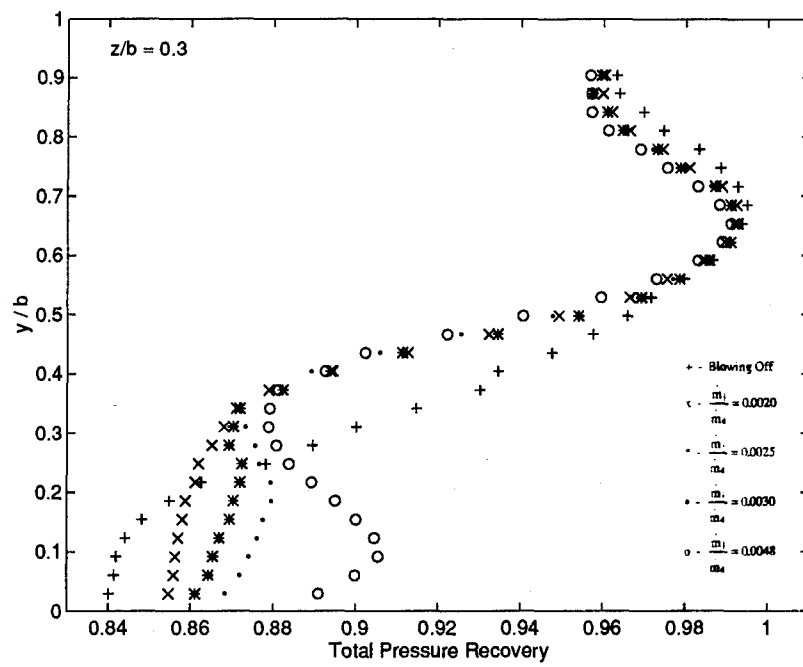


Figure 33. Total Pressure Recovery Profiles @ $z/b = 0.3$

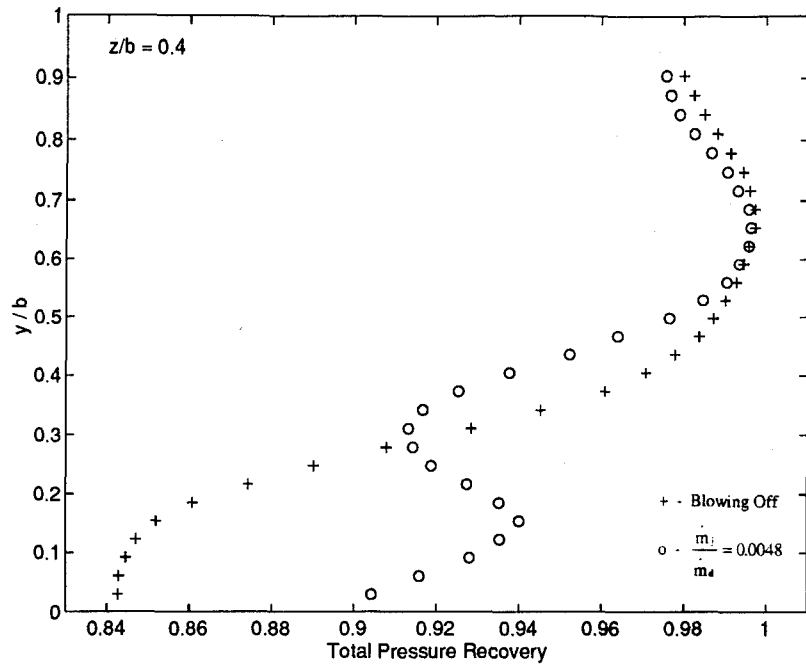


Figure 34. Total Pressure Recovery Profiles @ $z/b = 0.4$

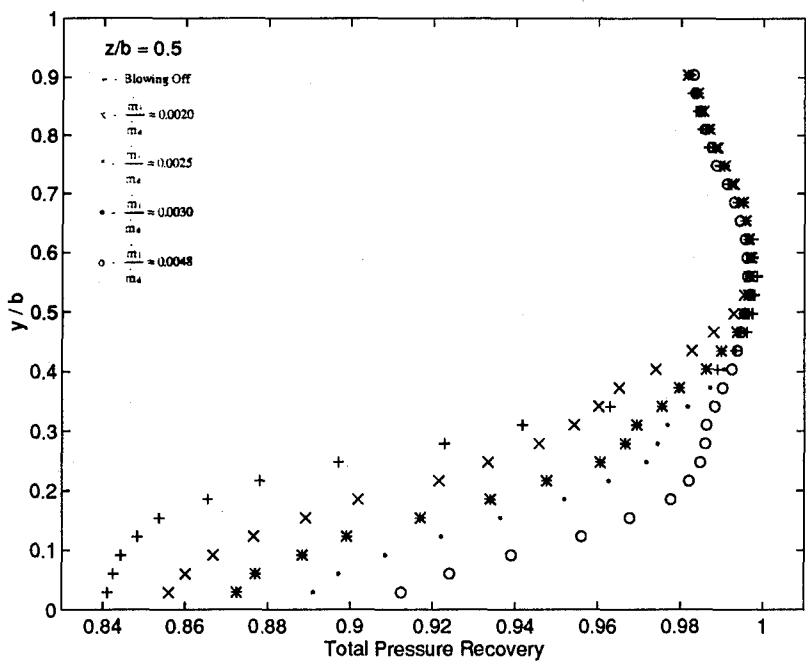


Figure 35. Total Pressure Recovery Profiles @ $z/b = 0.5$

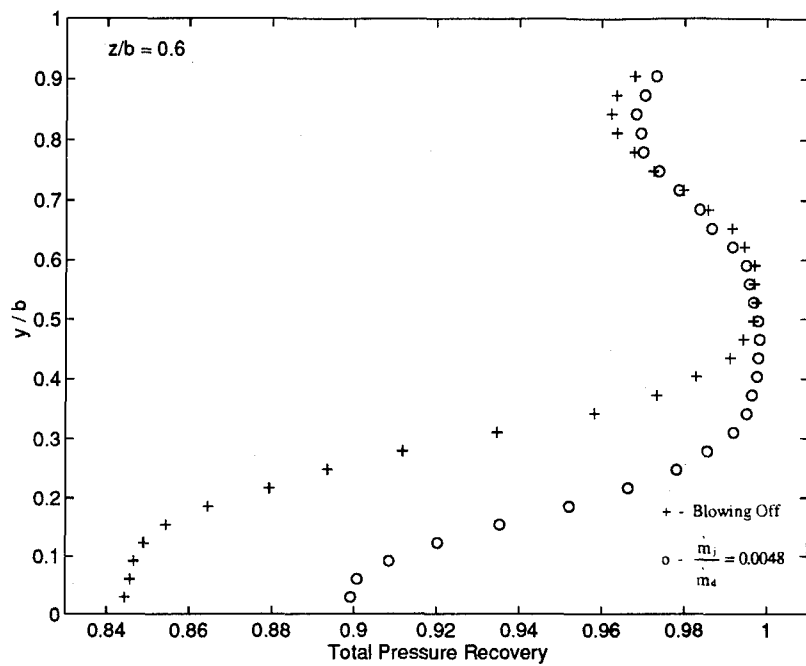


Figure 36. Total Pressure Recovery Profile @ $z/b = 0.6$

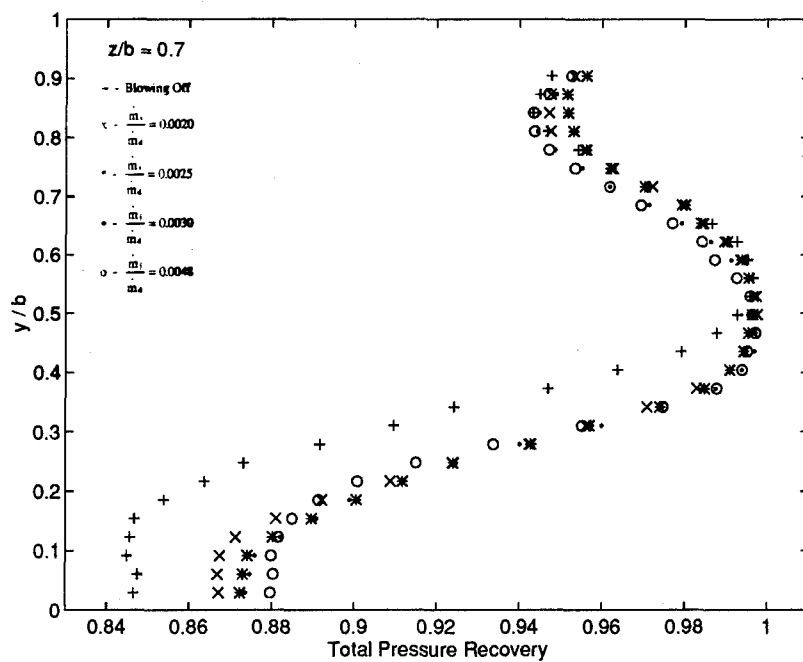


Figure 37. Total Pressure Recovery Profile @ $z/b = 0.7$

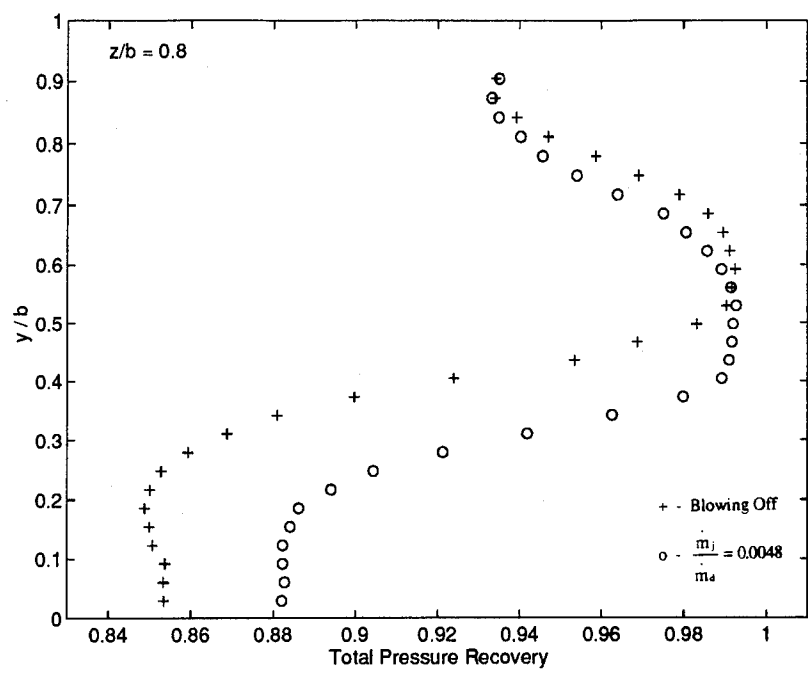


Figure 38. Total Pressure Recovery Profile @ $z/b = 0.8$

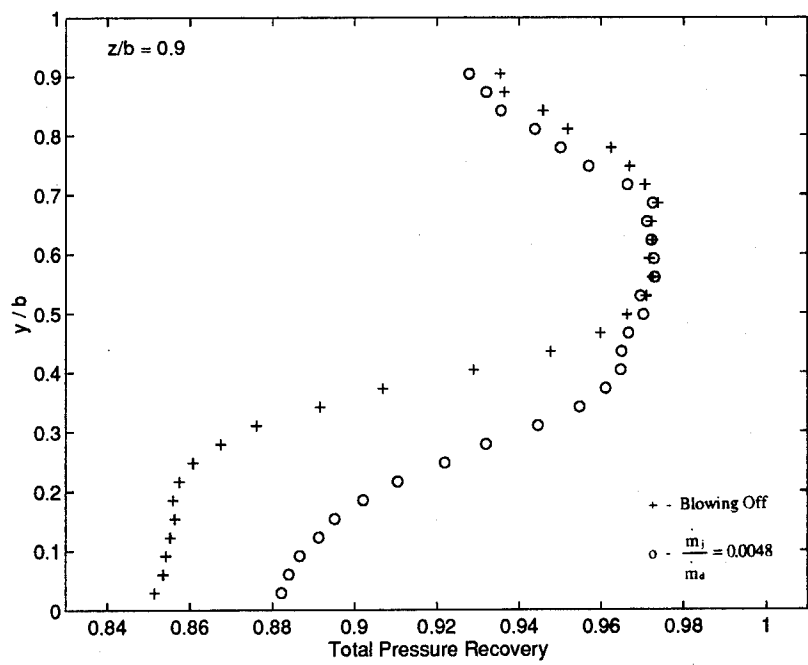


Figure 39. Total Pressure Recovery Profile @ $z/b = 0.9$

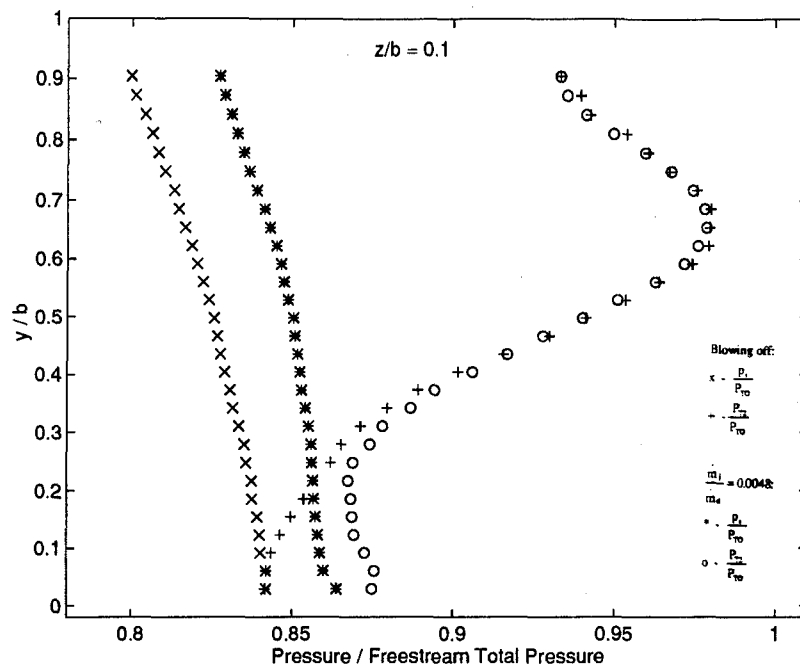


Figure 40. Total and Static Pressure Recovery Profiles @ $z/b = 0.1$

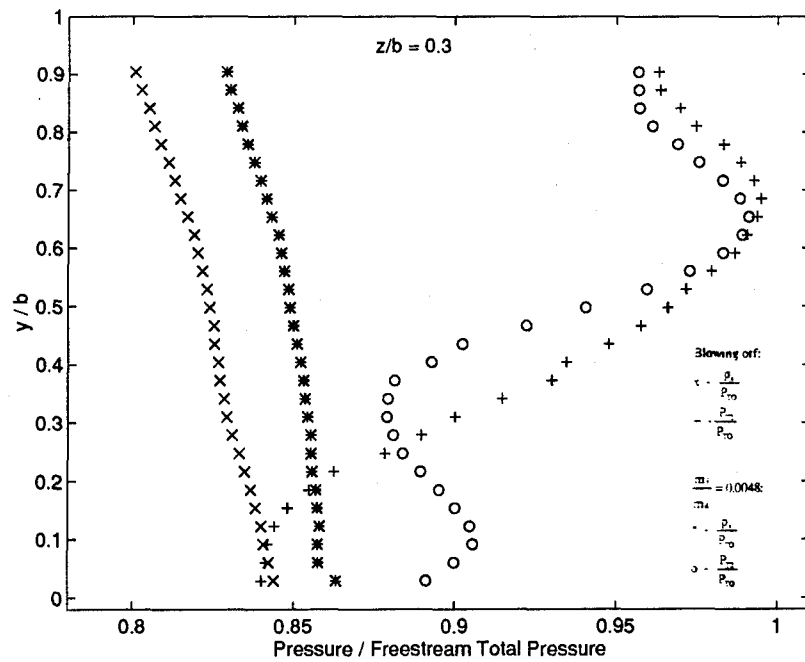


Figure 41. Total and Static Pressure Recovery Profiles @ $z/b = 0.3$

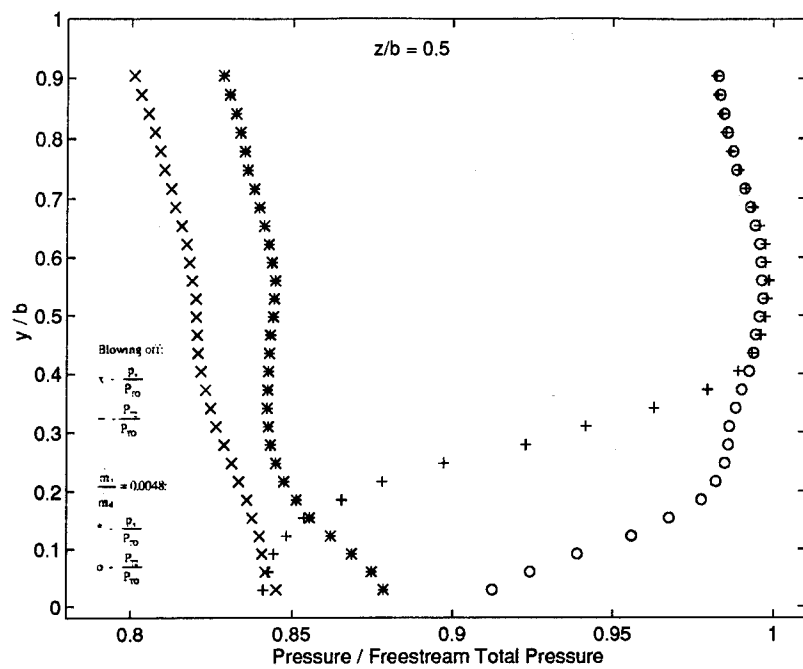


Figure 42. Total and Static Pressure Recovery Profiles @ $z/b = 0.5$

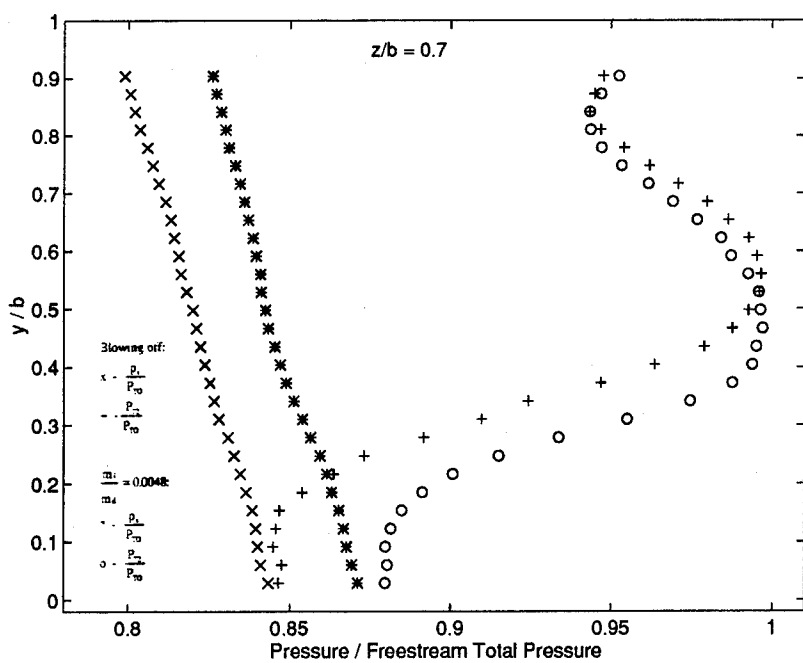


Figure 43. Total and Static Pressure Recovery Profiles @ $z/b = 0.7$

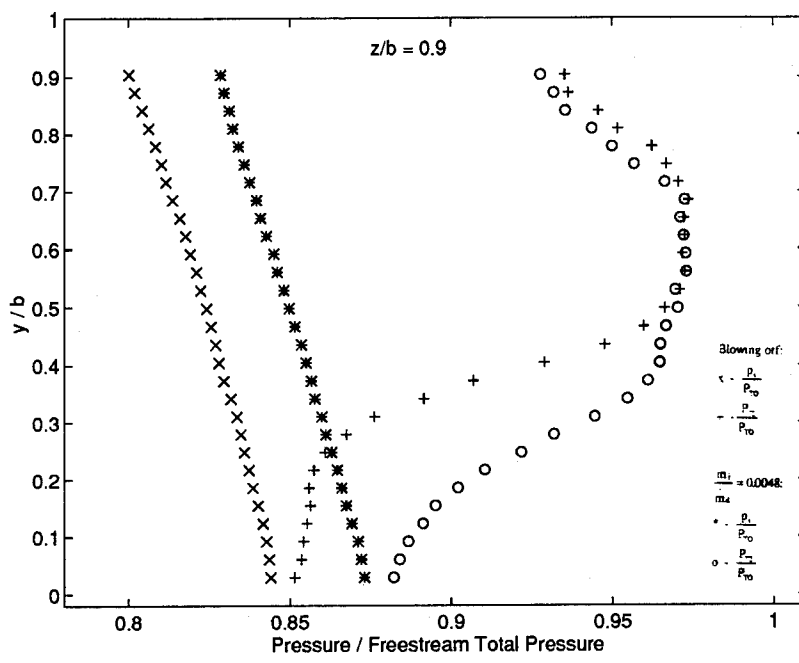


Figure 44. Total and Static Pressure Recovery Profiles @ $z/b = 0.9$

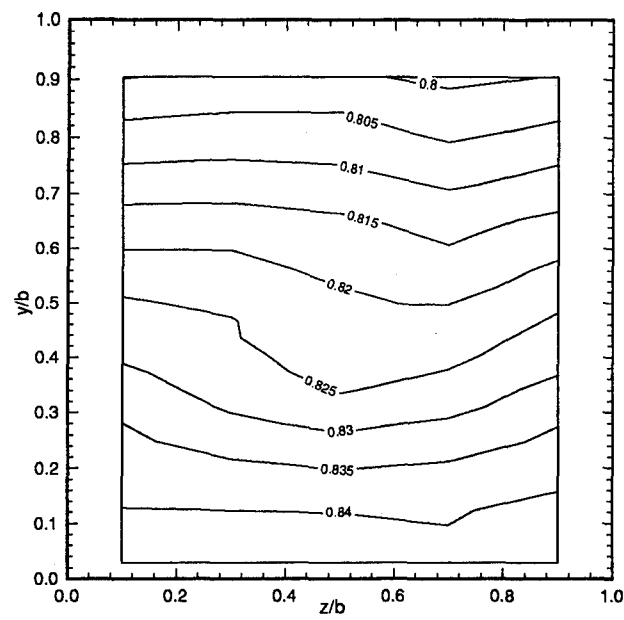


Figure 45. $M_1 = 0.6$ Exit Plane Static Pressure Recovery Map with Blowing Off

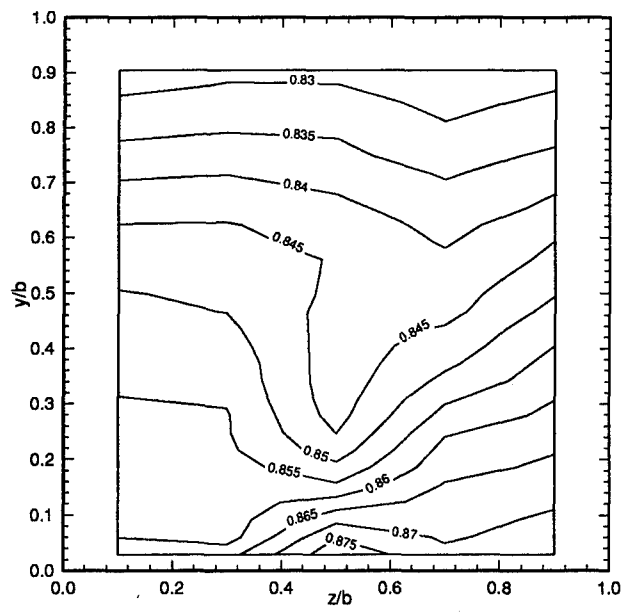


Figure 46. $M_1 = 0.6$ Exit Plane Static Pressure Recovery Map with $\frac{\dot{m}_i}{\dot{m}_d} = 0.0048$

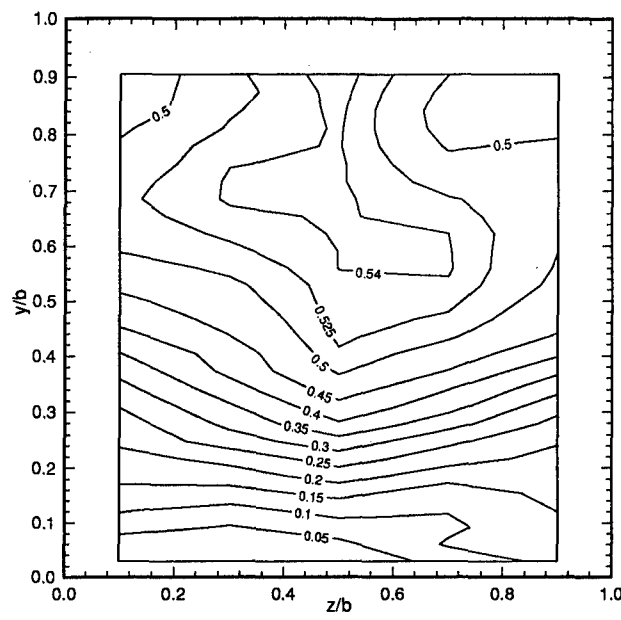


Figure 47. $M_1 = 0.6$ Exit Plane Mach Number Map with Blowing Off

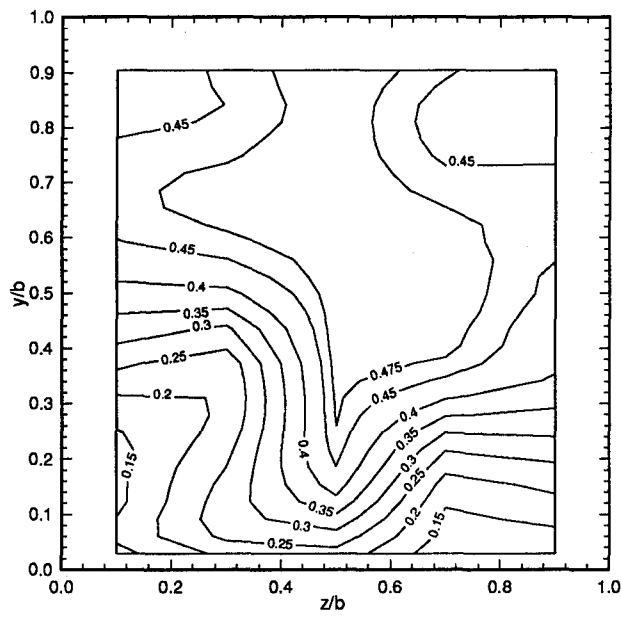


Figure 48. $M_1 = 0.6$ Exit Plane Mach Number Map with $\frac{\dot{m}_i}{\dot{m}_d} = 0.0048$

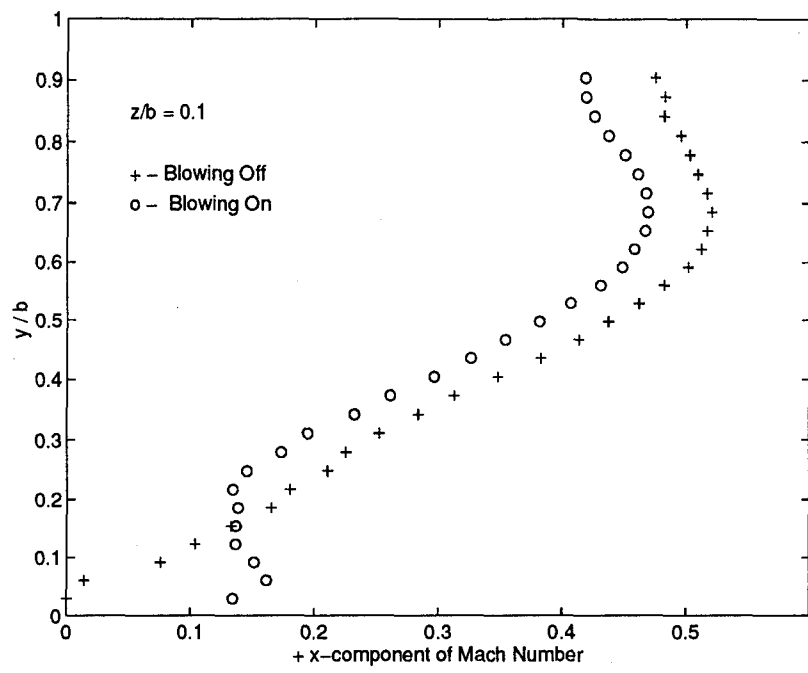


Figure 49. Mach Number Profiles Computed From Pitot-Static Data @ $z/b = 0.1$

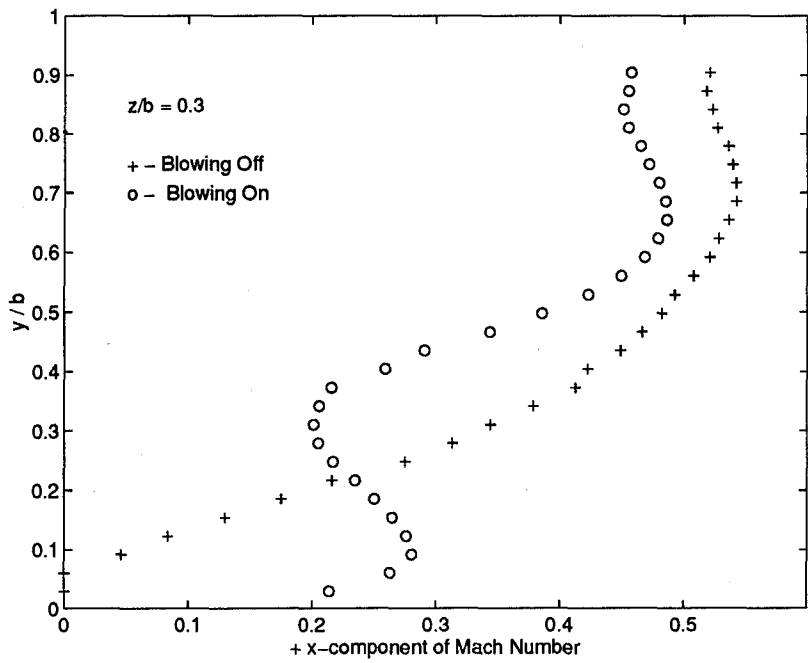


Figure 50. Mach Number Profiles Computed From Pitot-Static Data @ $z/b = 0.3$

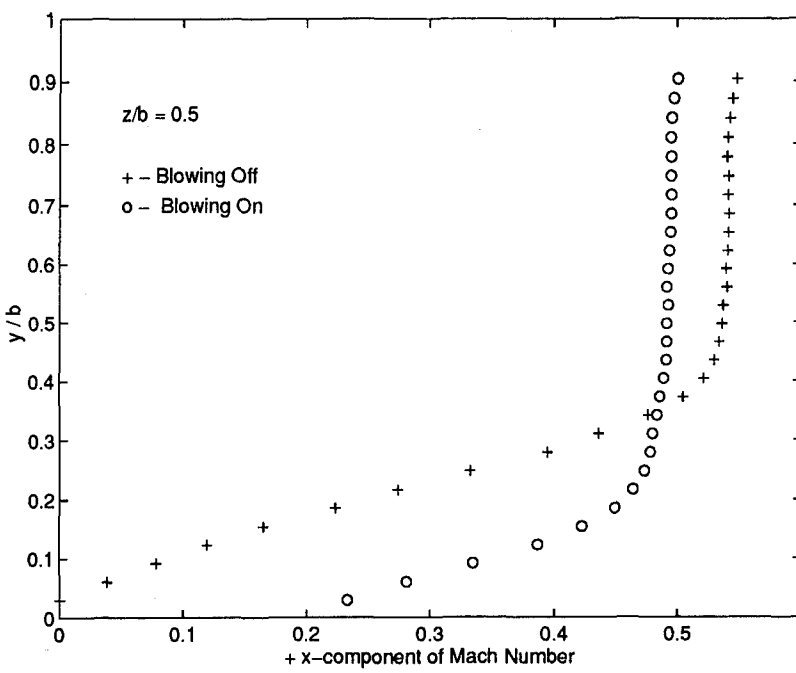


Figure 51. Mach Number Profiles Computed From Pitot-Static Data @ $z/b = 0.5$

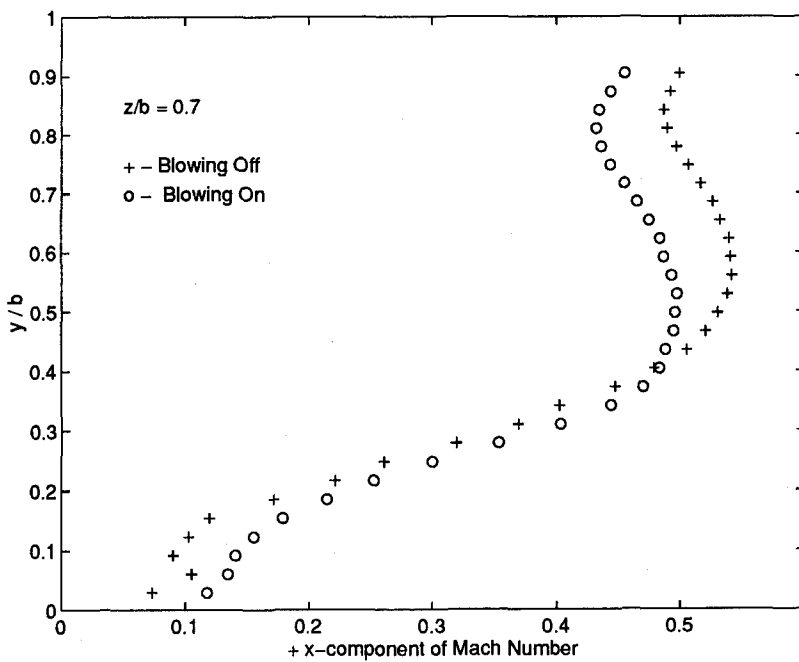


Figure 52. Mach Number Profiles Computed From Pitot-Static Data @ $z/b = 0.7$

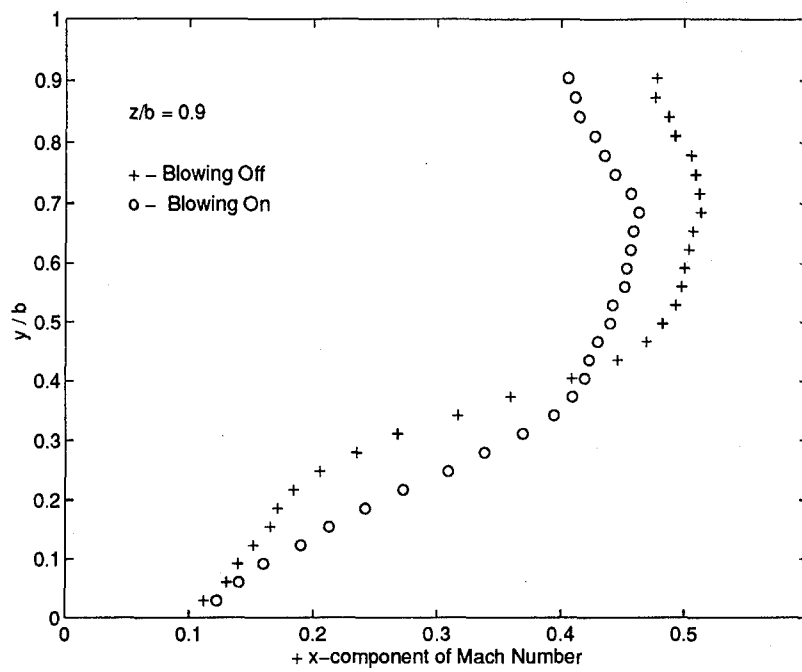


Figure 53. Mach Number Profiles Computed From Pitot-Static Data @ $z/b = 0.9$

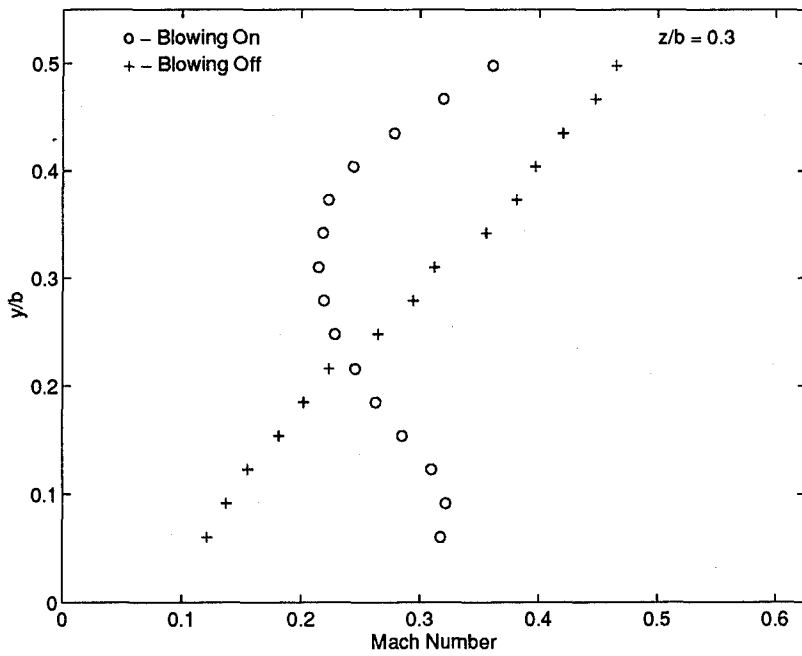


Figure 54. Mach Number Profiles Computed From Cross-Film Data @ $z/b = 0.3$

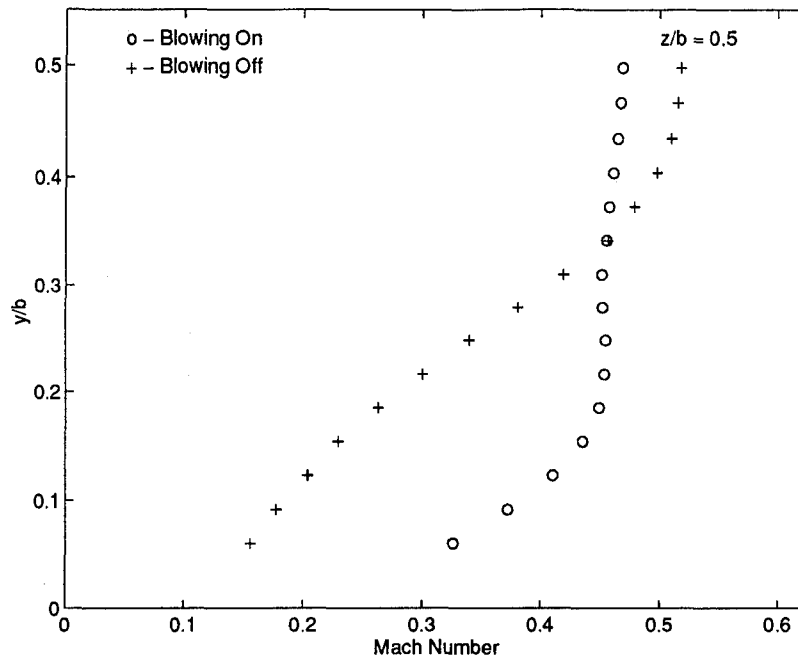


Figure 55. Mach Number Profiles Computed From Cross-Film Data @ $z/b = 0.5$

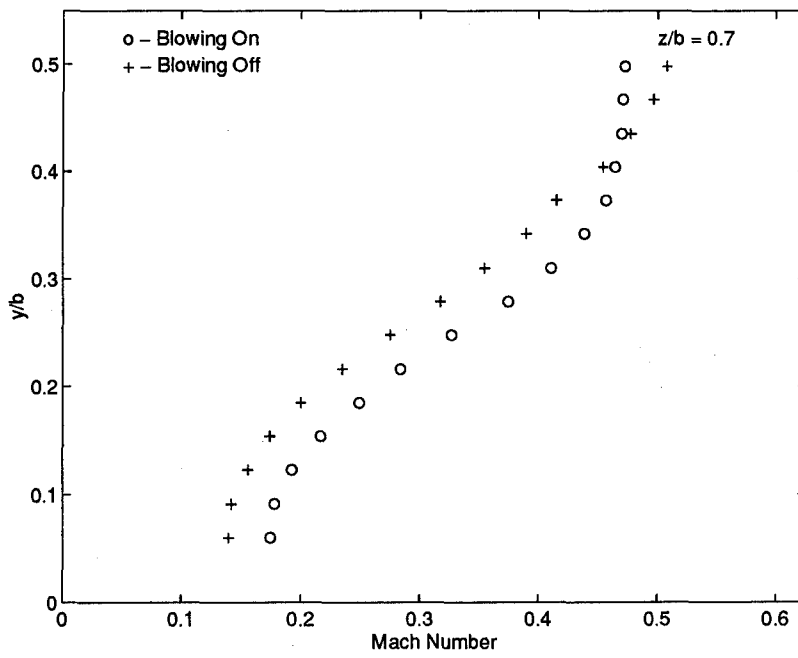


Figure 56. Mach Number Profiles Computed From Cross-Film Data @ $z/b = 0.7$

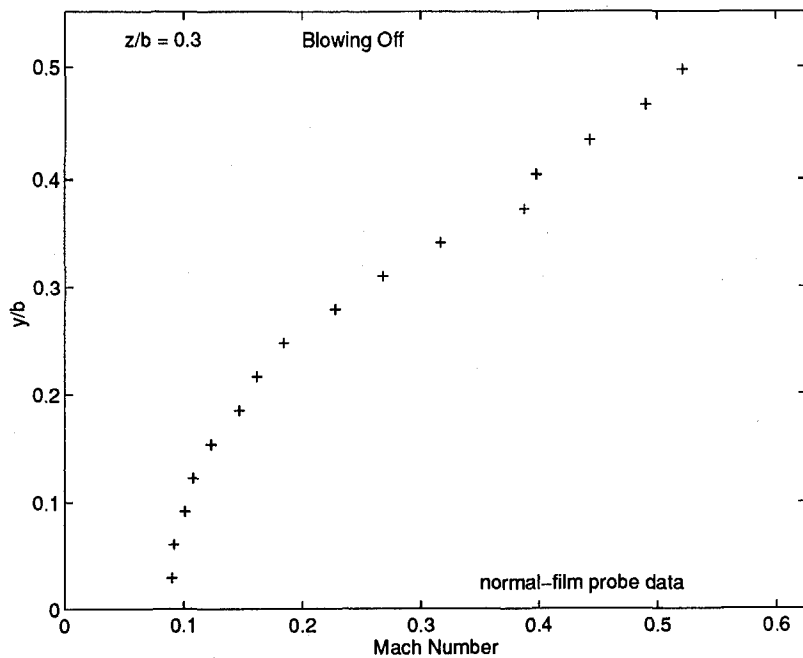


Figure 57. Mach Number Profile Computed From Normal-Film Data @ $z/b = 0.3$

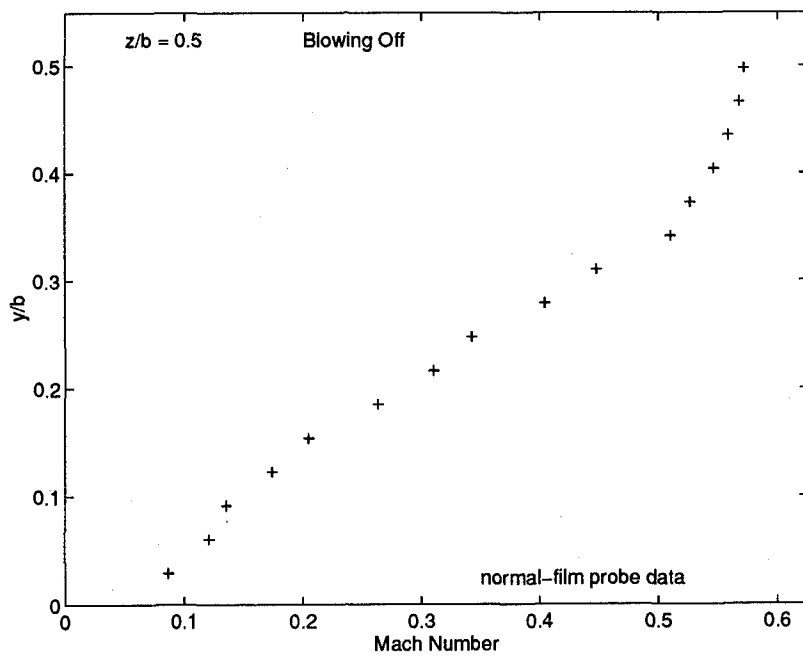


Figure 58. Mach Number Profile Computed From Normal-Film Data @ $z/b = 0.5$

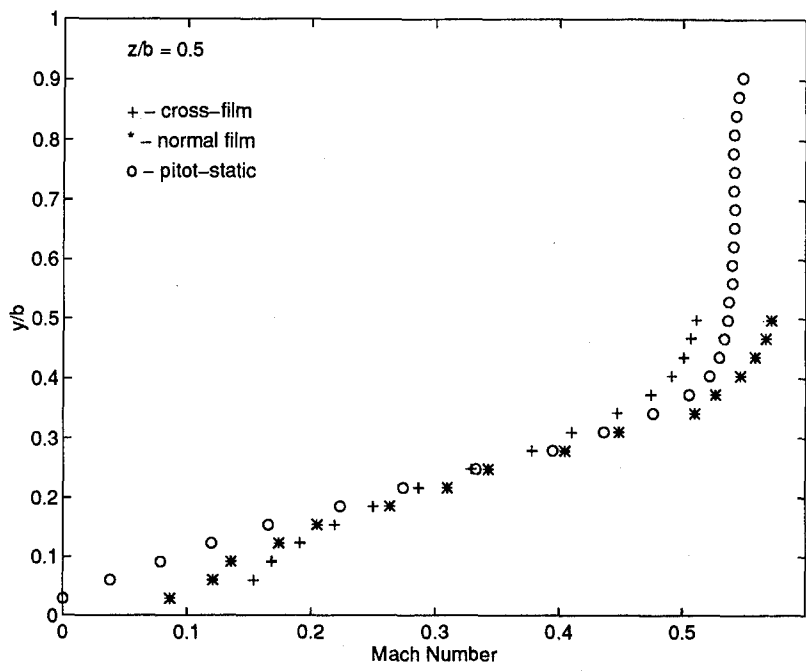


Figure 59. Comparison of 3 Sources for Mach Number - Blowing Off, $z/b = 0.5$

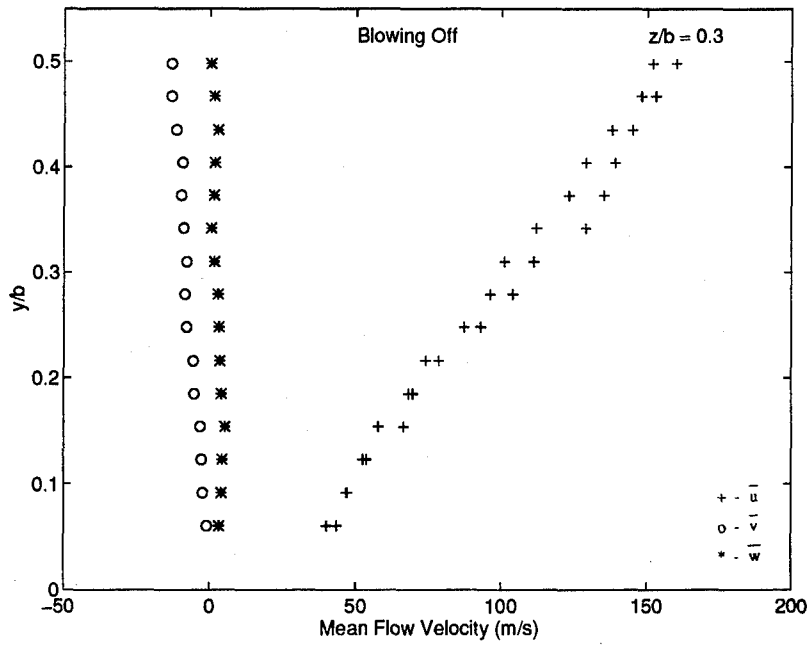


Figure 60. Mean Velocity Component Profiles - Blowing Off, $z/b = 0.3$

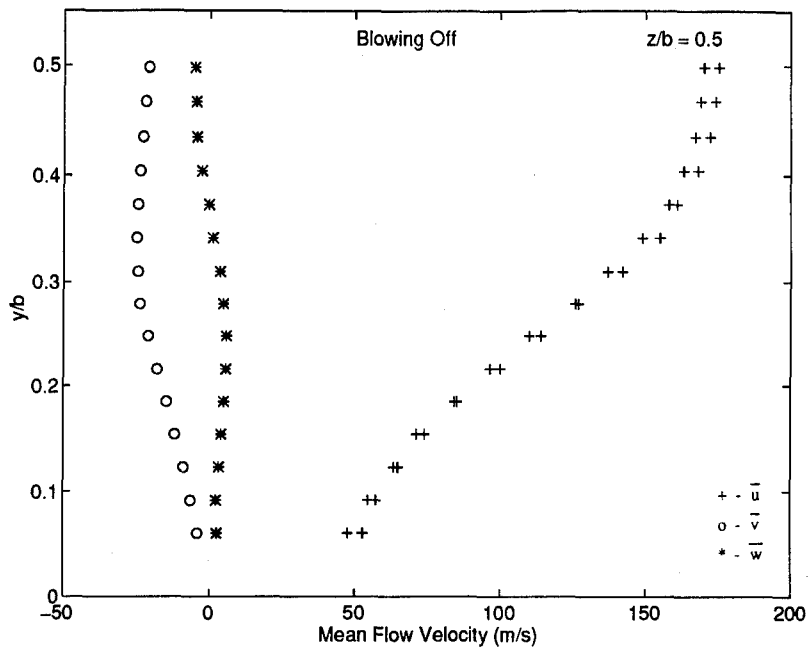


Figure 61. Mean Velocity Component Profiles - Blowing Off, $z/b = 0.5$

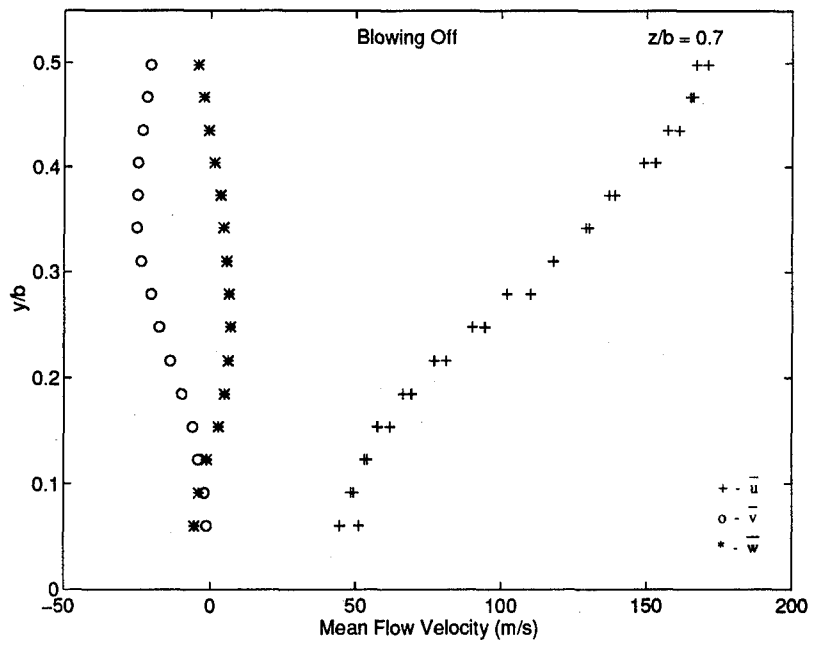


Figure 62. Mean Velocity Component Profiles - Blowing Off, $z/b = 0.7$

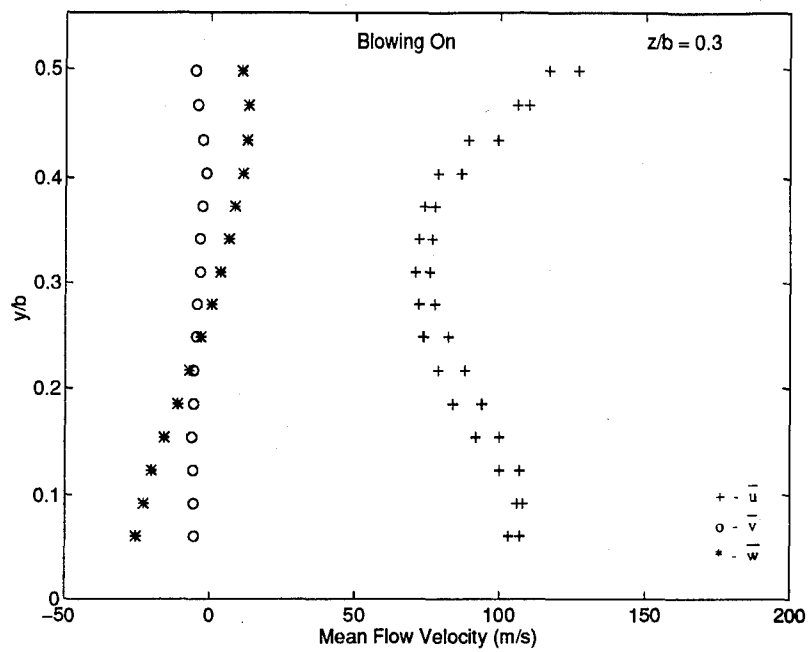


Figure 63. Mean Velocity Component Profiles - Blowing On, $z/b = 0.3$

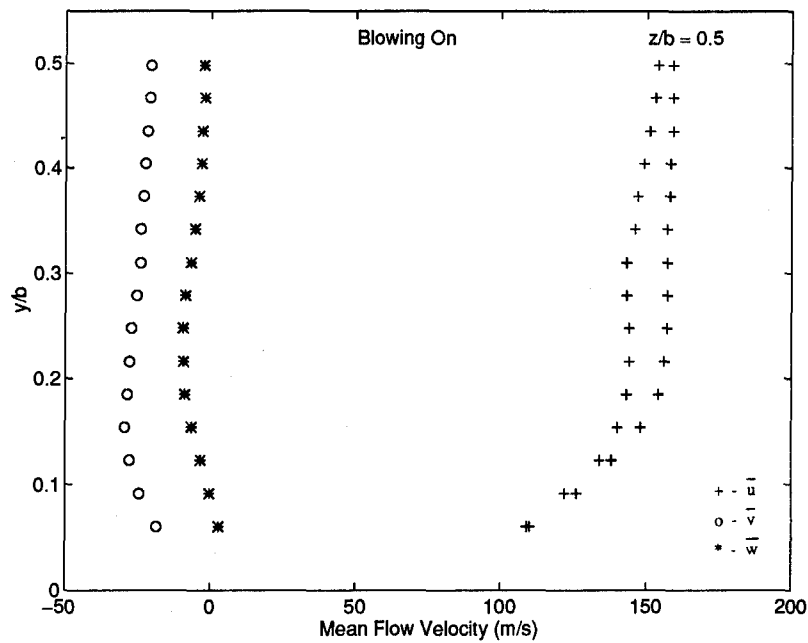


Figure 64. Mean Velocity Component Profiles - Blowing On, $z/b = 0.5$

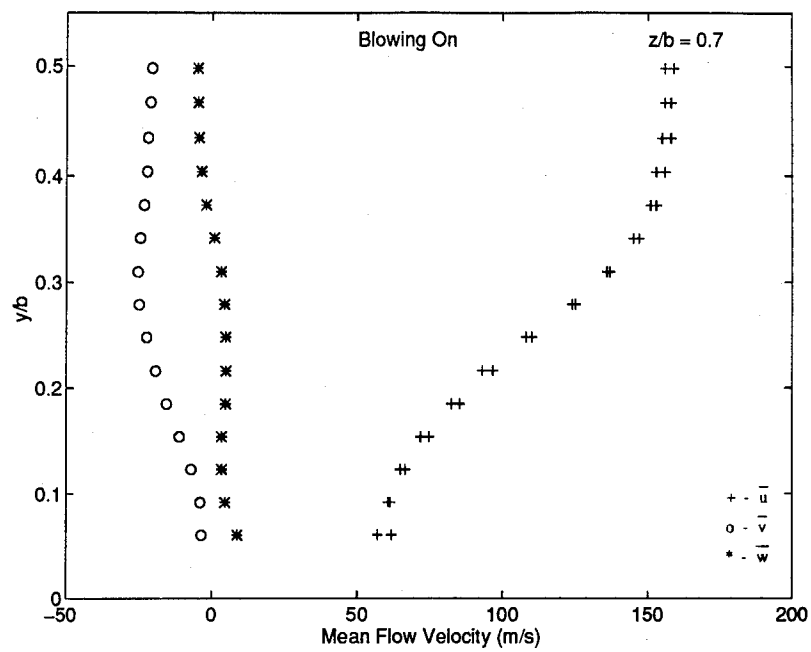


Figure 65. Mean Velocity Component Profiles - Blowing On, $z/b = 0.7$

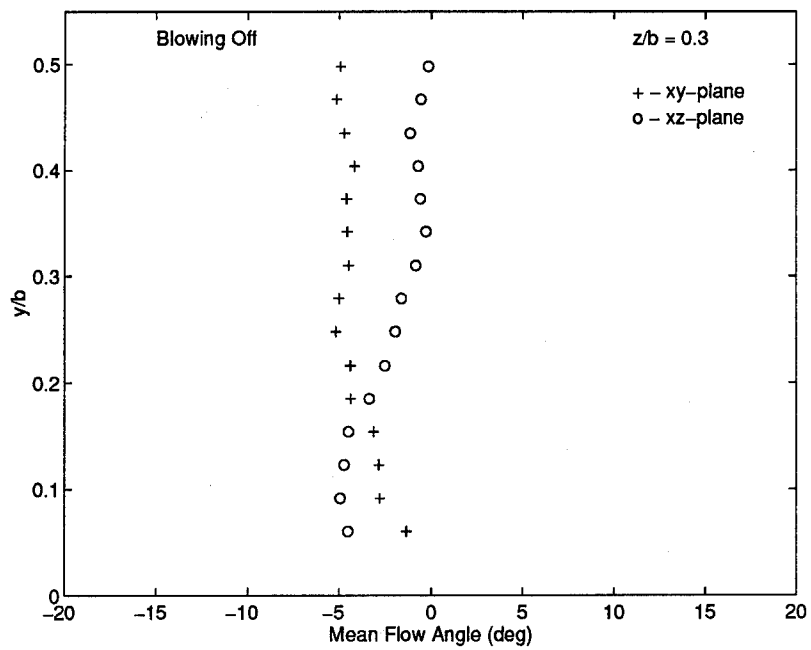


Figure 66. Mean Flow Angle Profiles - Blowing Off, $z/b = 0.3$

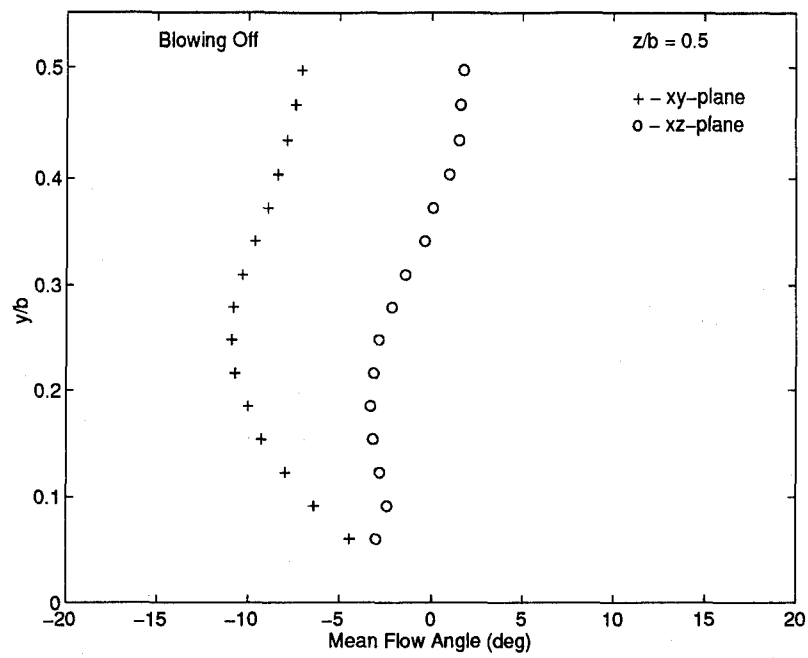


Figure 67. Mean Flow Angle Profiles - Blowing Off, $z/b = 0.5$

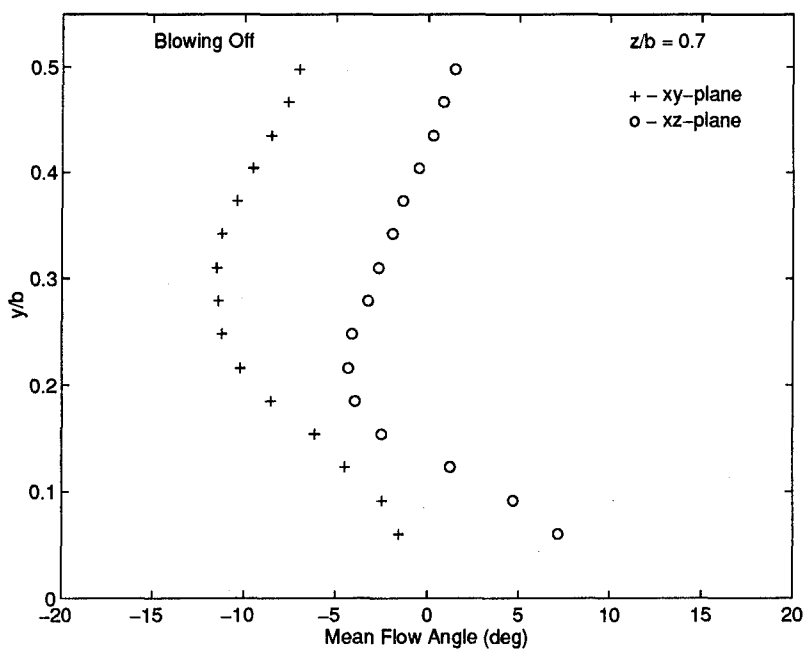


Figure 68. Mean Flow Angle Profiles - Blowing Off, $z/b = 0.7$

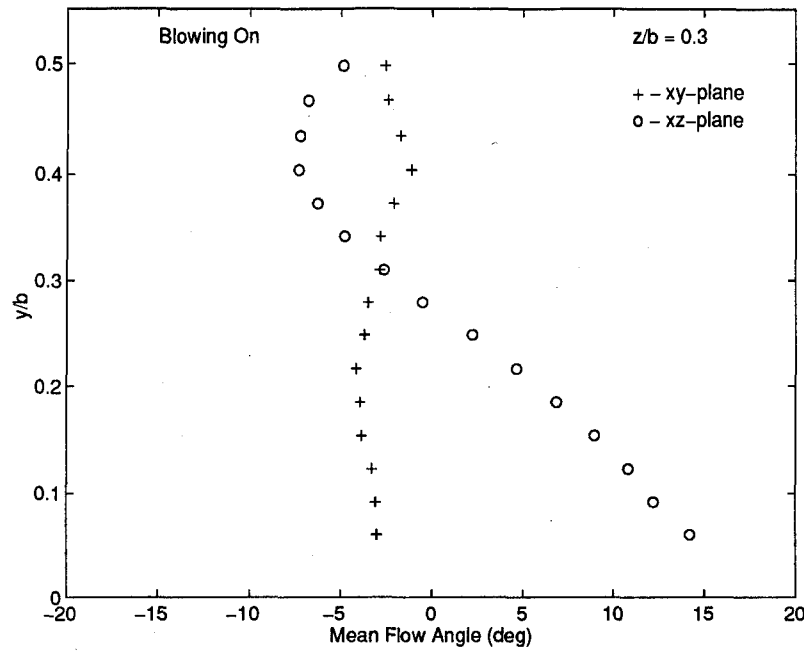


Figure 69. Mean Flow Angle Profiles - Blowing On, $z/b = 0.3$

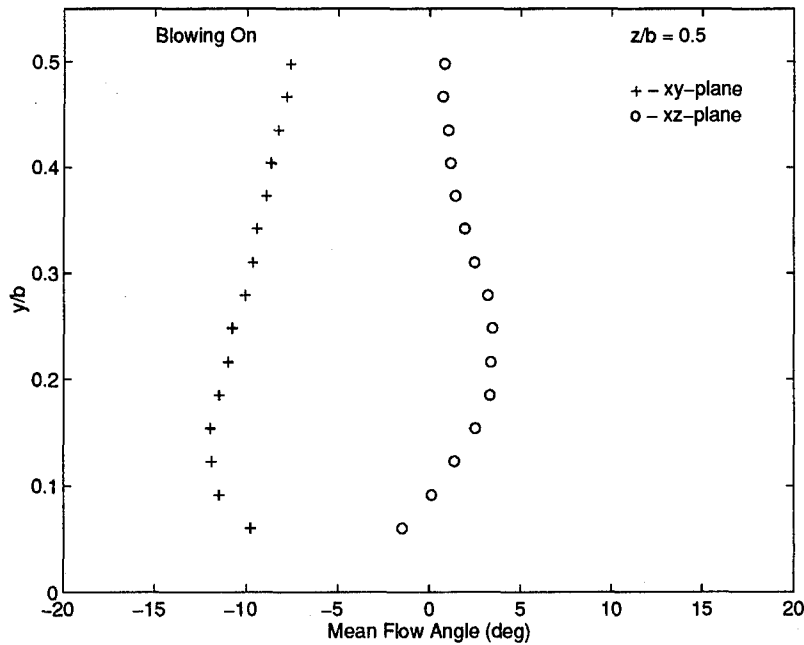


Figure 70. Mean Flow Angle Profiles - Blowing On, $z/b = 0.5$

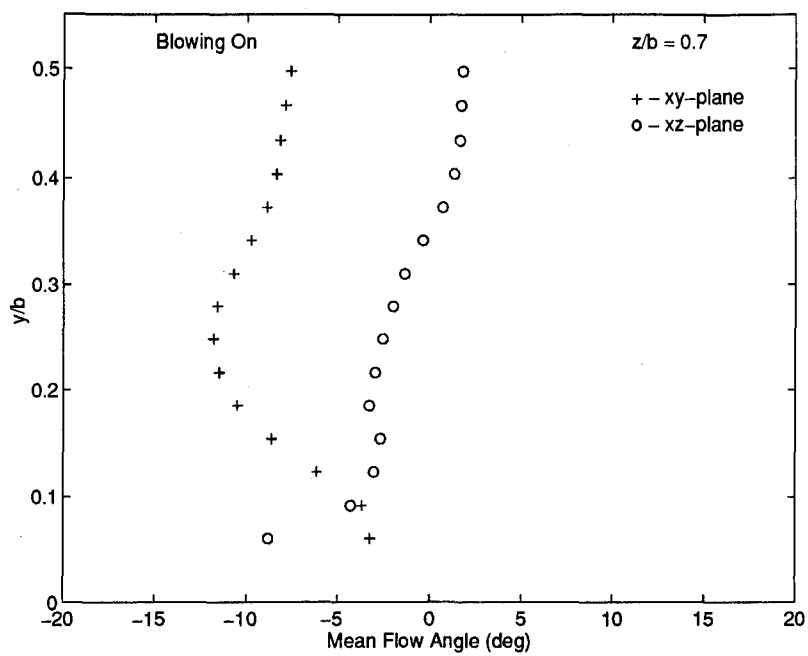
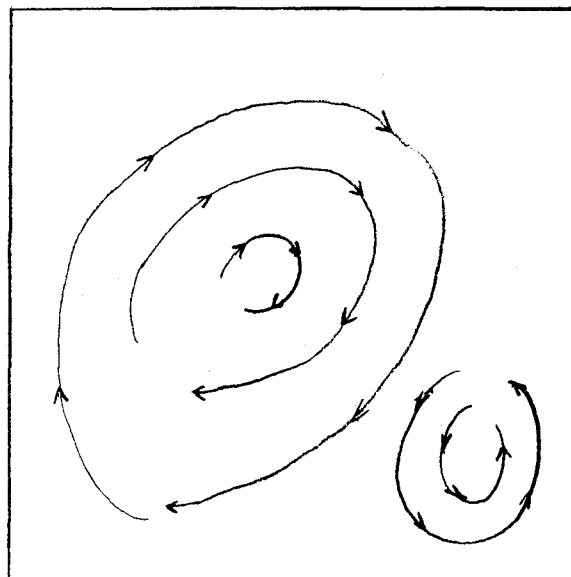


Figure 71. Mean Flow Angle Profiles - Blowing On, $z/b = 0.7$



$$\frac{z}{b} = 0.0$$

$$\frac{z}{b} = 1.0$$

Figure 72. Hypothesized Vortex Arrangement at the Exit Plane - Blowing On

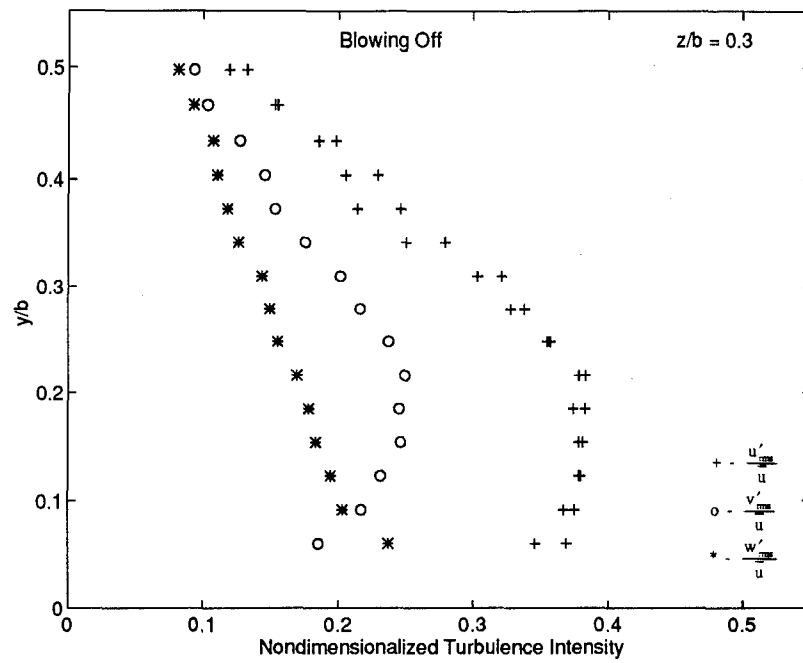


Figure 73. Turbulence Intensity (Cross-Film) - Blowing Off, $z/b = 0.3$

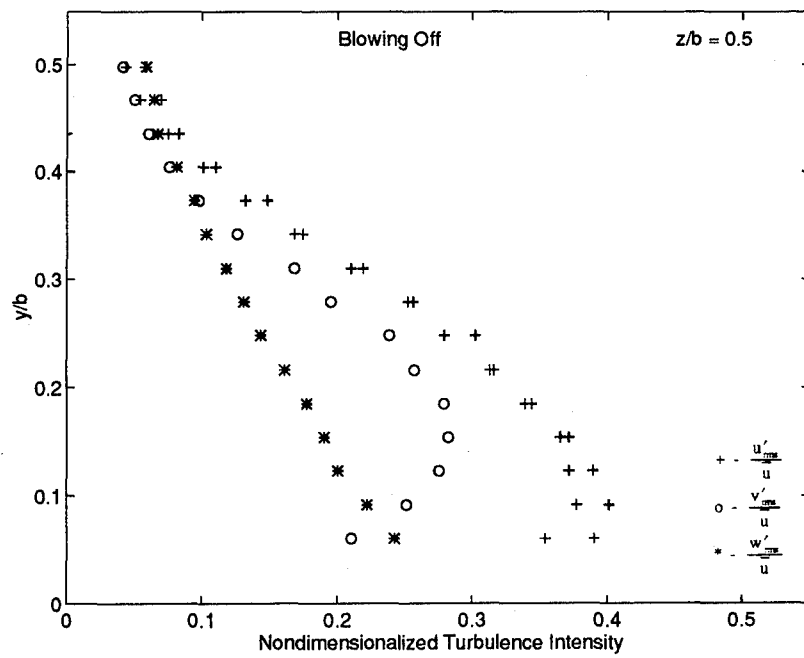


Figure 74. Turbulence Intensity (Cross-Film) - Blowing Off, $z/b = 0.5$

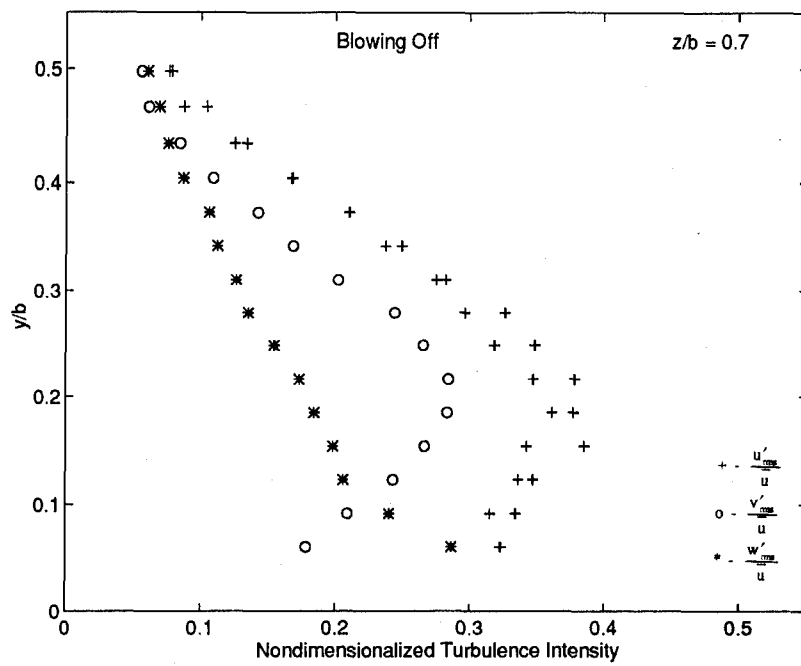


Figure 75. Turbulence Intensity (Cross-Film) - Blowing Off, $z/b = 0.7$

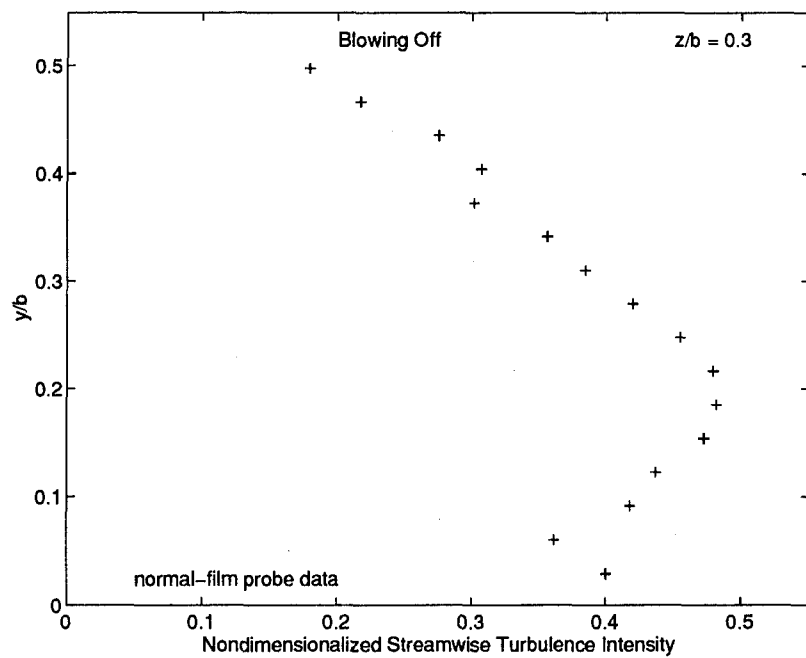


Figure 76. Turbulence Intensity (Normal-Film) - Blowing Off, $z/b = 0.3$

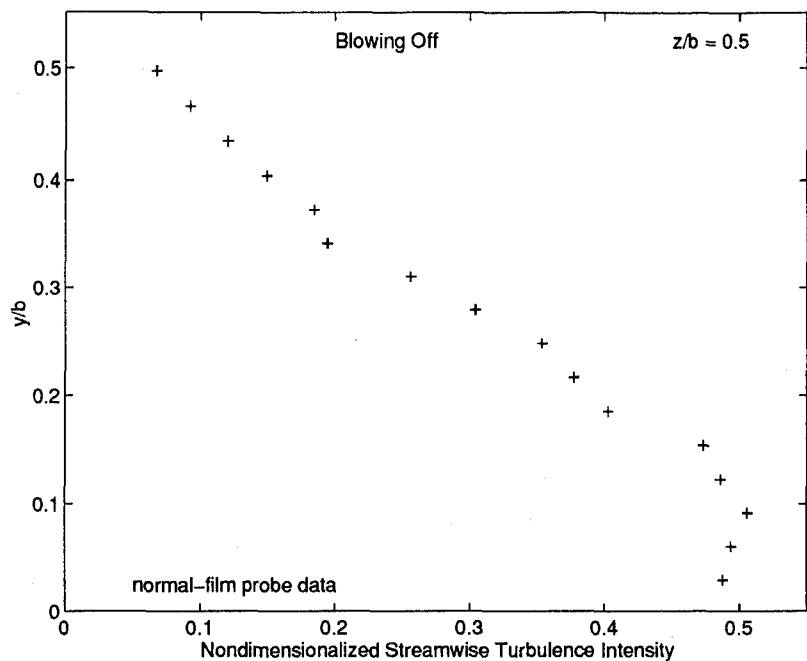


Figure 77. Turbulence Intensity (Normal-Film) - Blowing Off, $z/b = 0.5$

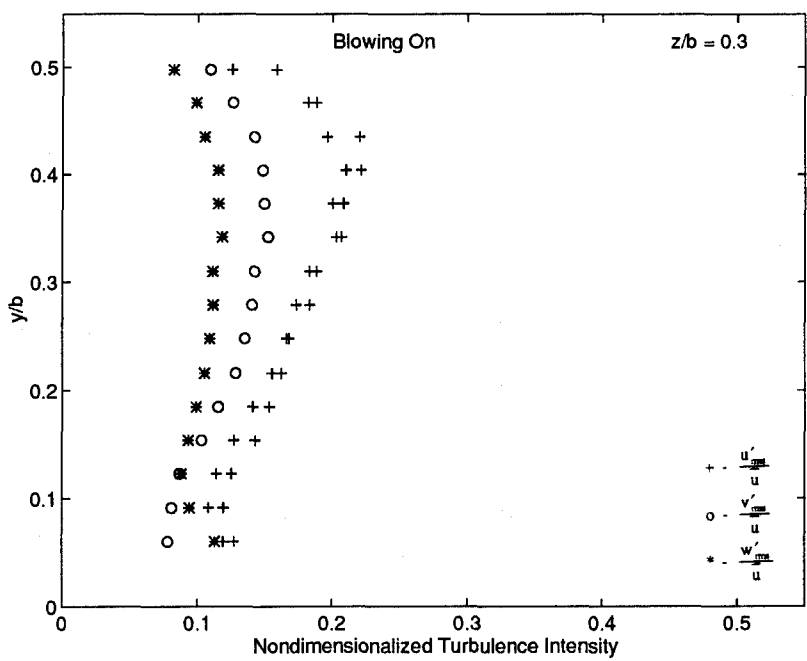


Figure 78. Turbulence Intensity (Cross-Film) - Blowing On, $z/b = 0.3$

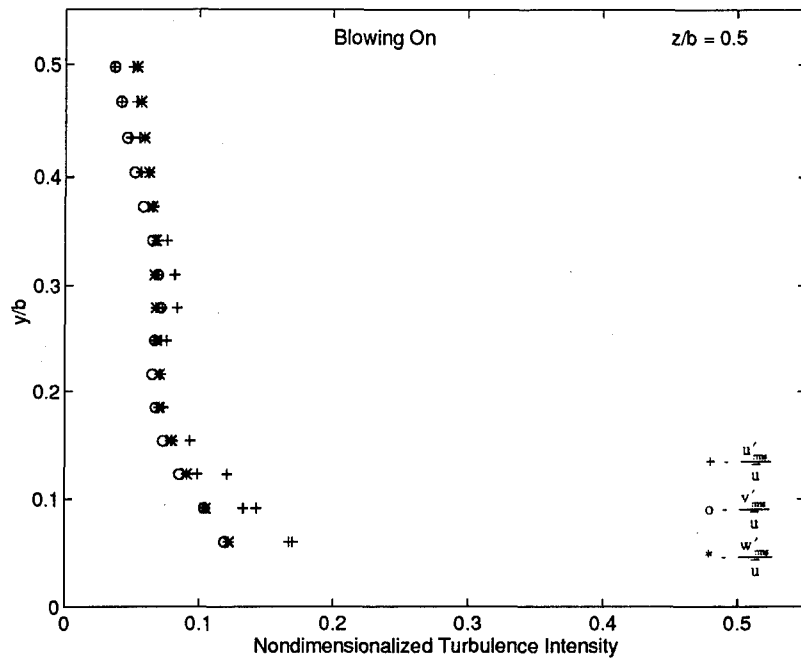


Figure 79. Turbulence Intensity (Cross-Film) - Blowing On, $z/b = 0.5$

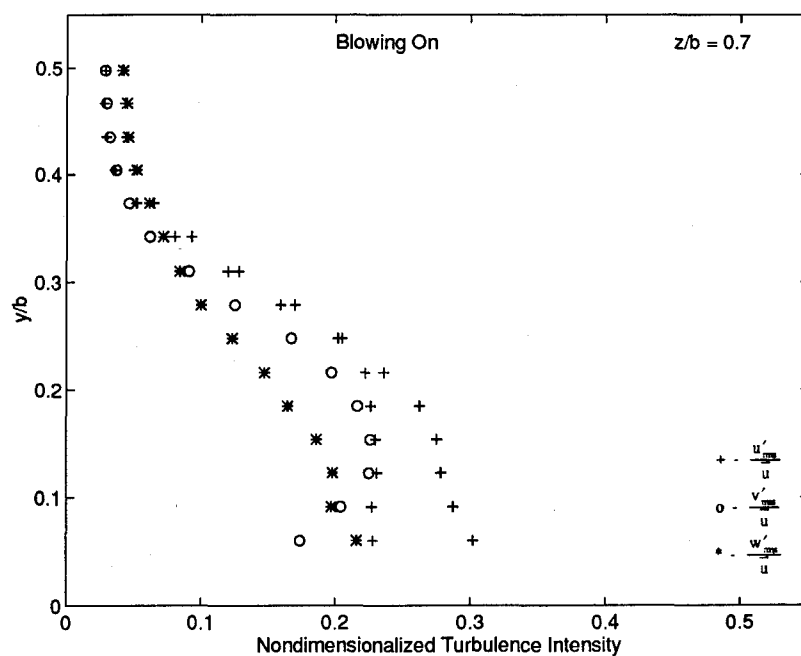


Figure 80. Turbulence Intensity (Cross-Film) - Blowing On, $z/b = 0.7$

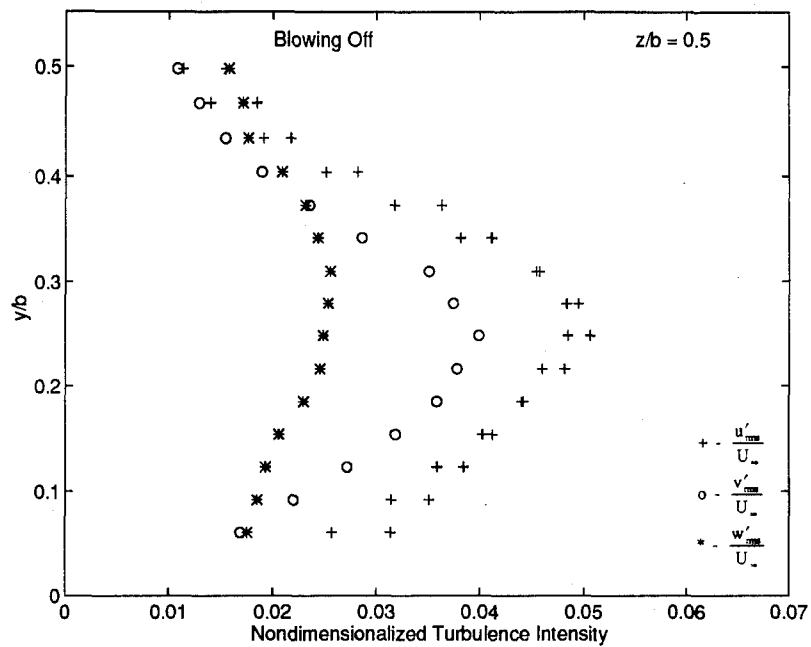


Figure 81. Turbulence Intensity (Cross-Film) Nondimensionalized by U_{∞} - Blowing Off,
 $z/b = 0.5$

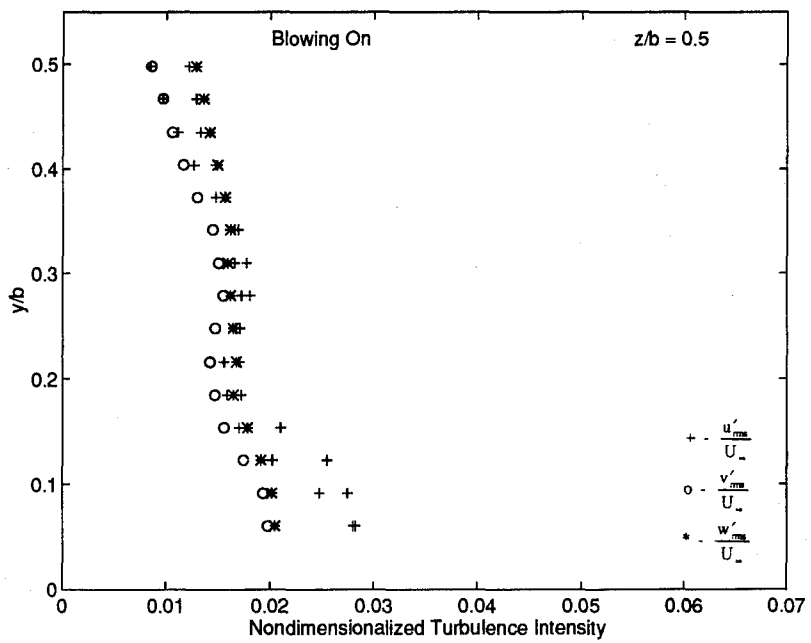


Figure 82. Turbulence Intensity(Cross Film) Nondimensionalized by U_{∞} - Blowing On, $z/b = 0.5$

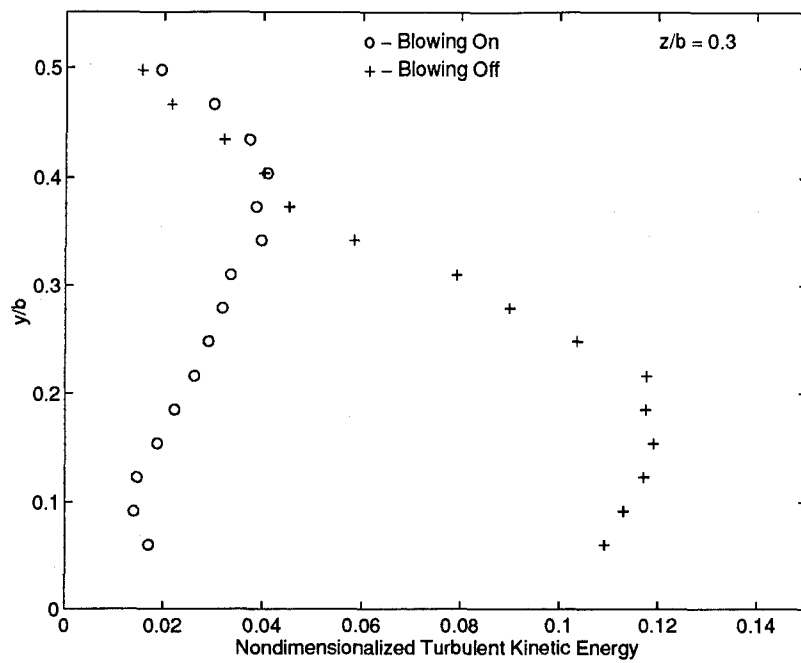


Figure 83. Turbulent Kinetic Energy - Blowing On and Off, $z/b = 0.3$

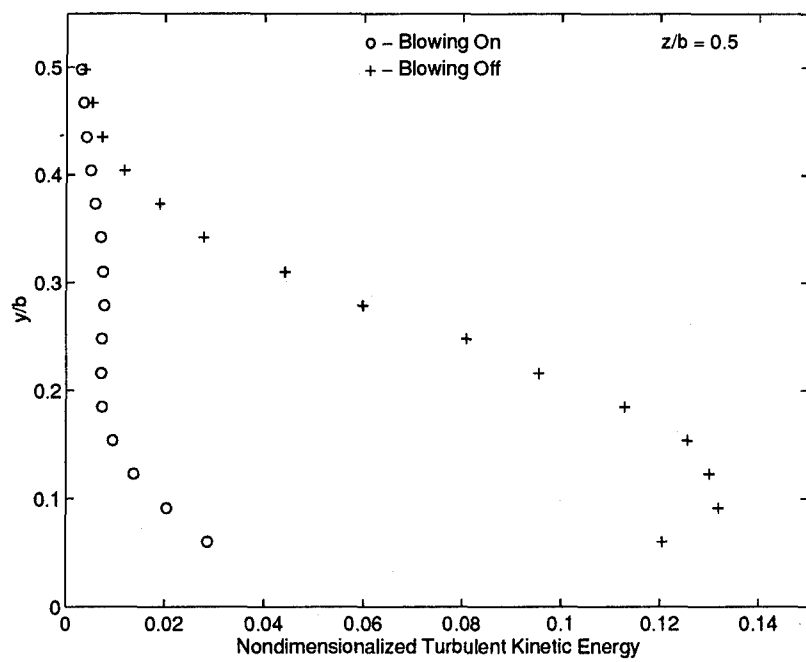


Figure 84. Turbulent Kinetic Energy - Blowing On and Off, $z/b = 0.5$

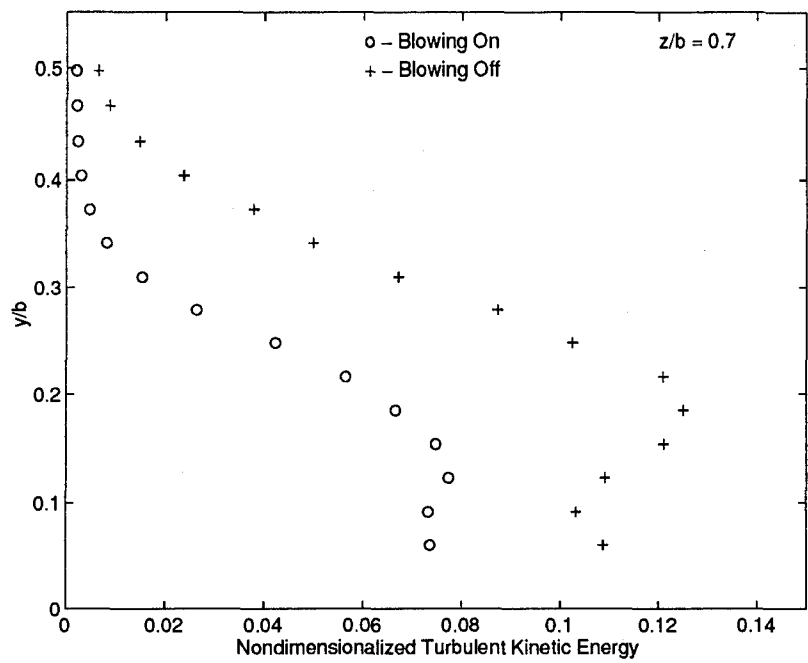


Figure 85. Turbulent Kinetic Energy - Blowing On and Off, $z/b = 0.7$

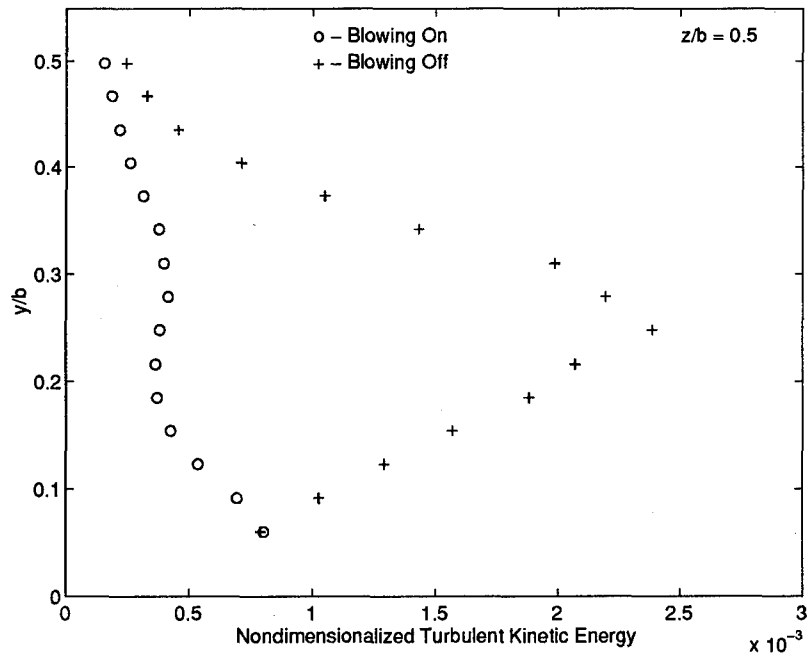


Figure 86. Turbulent Kinetic Energy Nondimensionalized by U_∞^2 - Blowing On and Off, $z/b = 0.5$

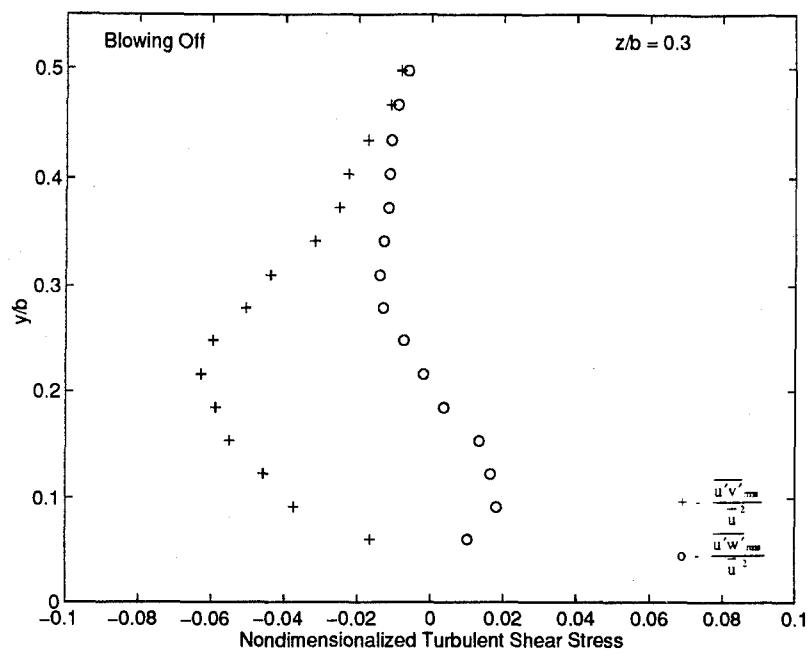


Figure 87. Turbulent Shear Stress Components - Blowing Off, $z/b = 0.3$

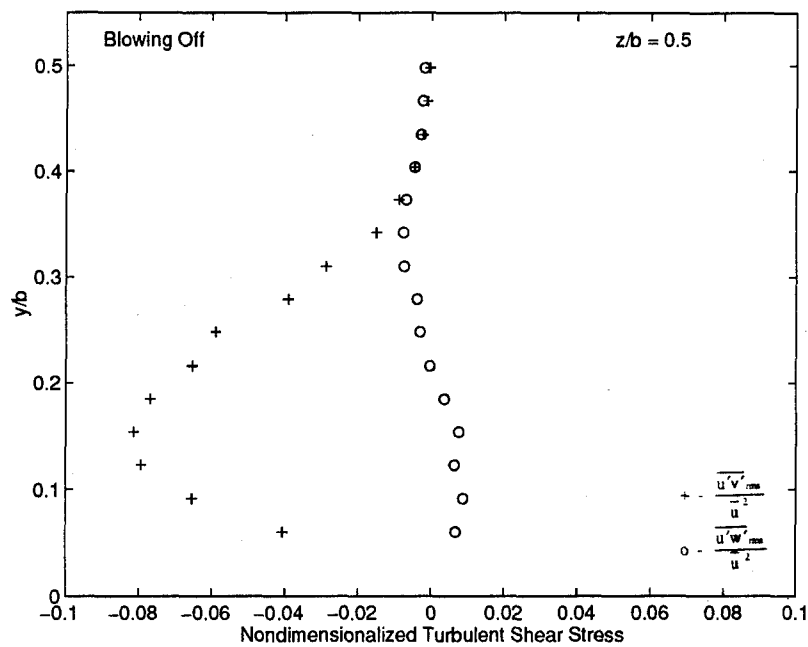


Figure 88. Turbulent Shear Stress Components - Blowing Off, $z/b = 0.5$

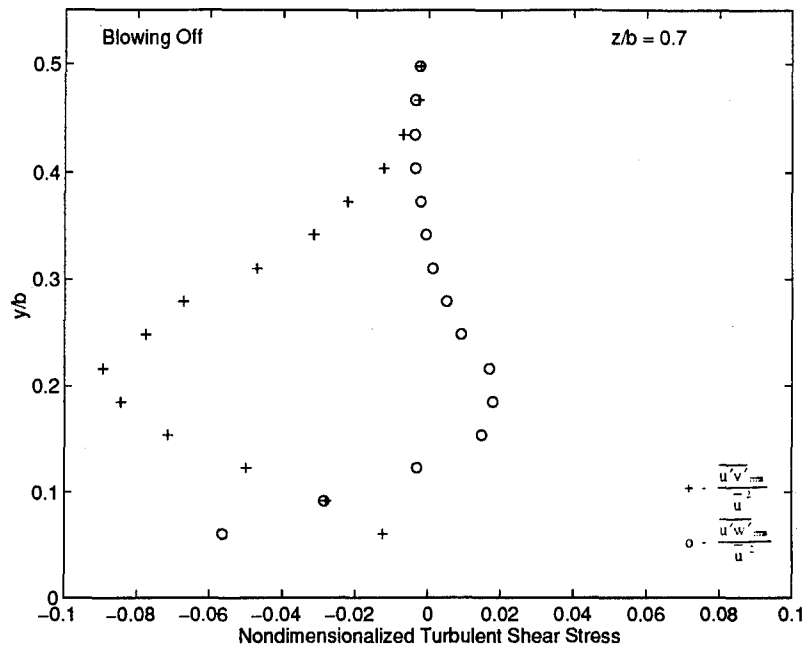


Figure 89. Turbulent Shear Stress Component s - Blowing Off, $z/b = 0.7$

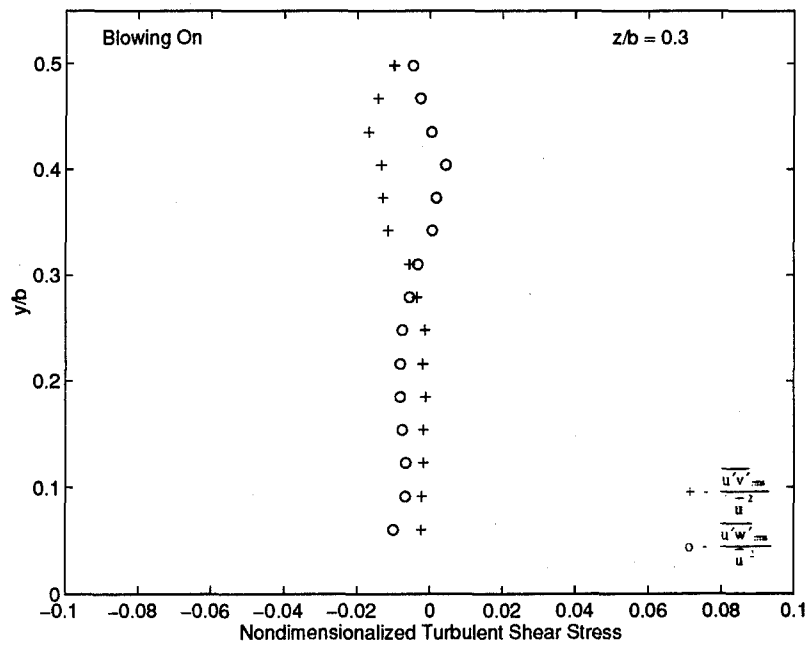


Figure 90. Turbulent Shear Stress Components - Blowing On, $z/b = 0.3$

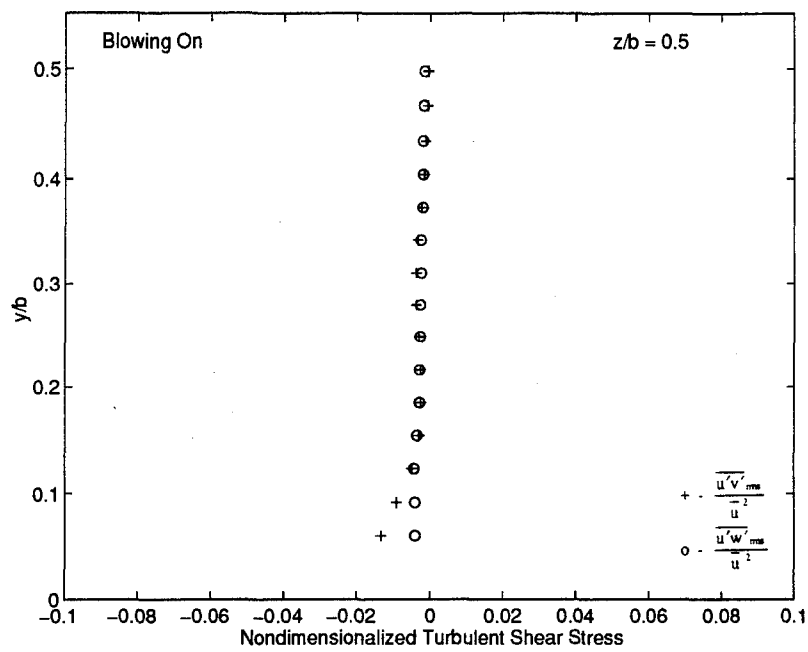


Figure 91. Turbulent Shear Stress Components - Blowing On, $z/b = 0.5$

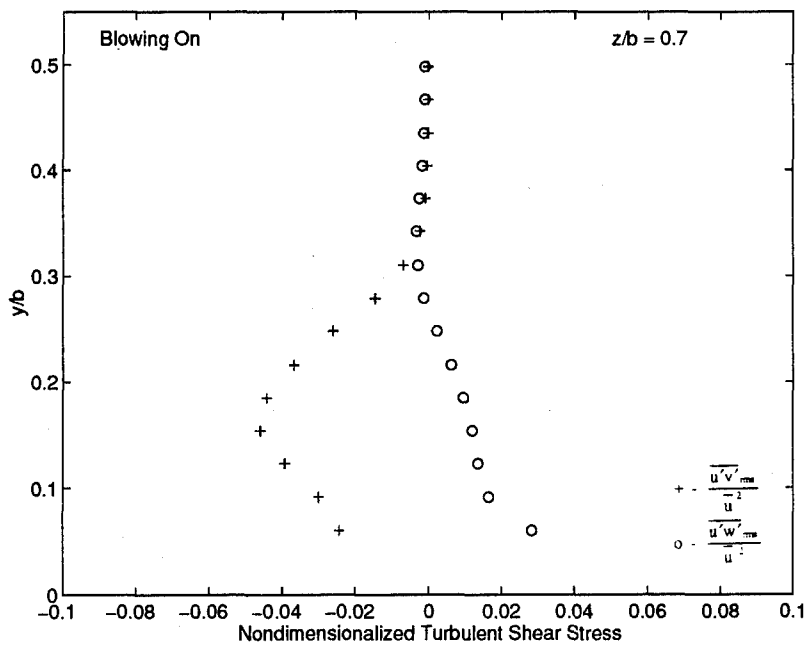


Figure 92. Turbulent Shear Stress Components - Blowing On, $z/b = 0.7$

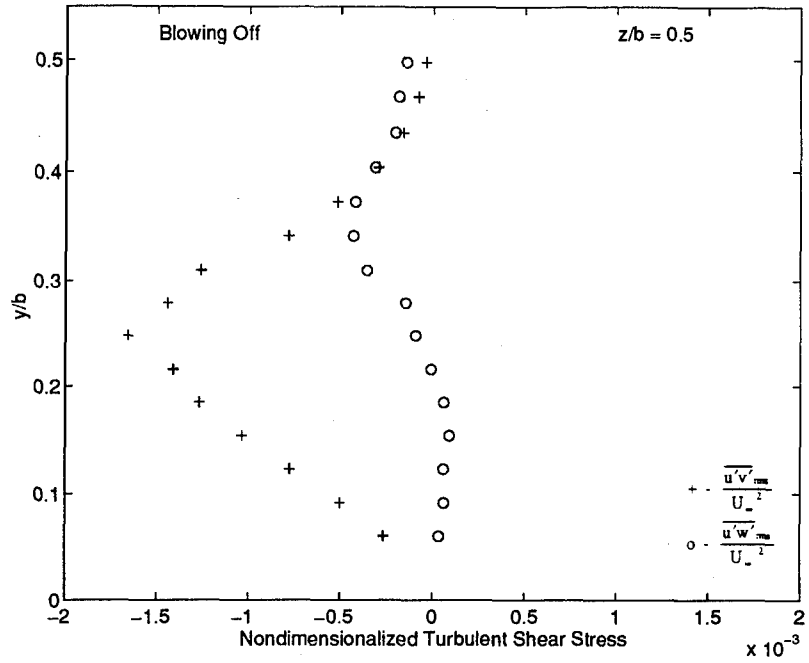


Figure 93. Turbulent Shear Stress Components Nondimensionalized by U_∞^2 - Blowing Off,
 $z/b = 0.5$

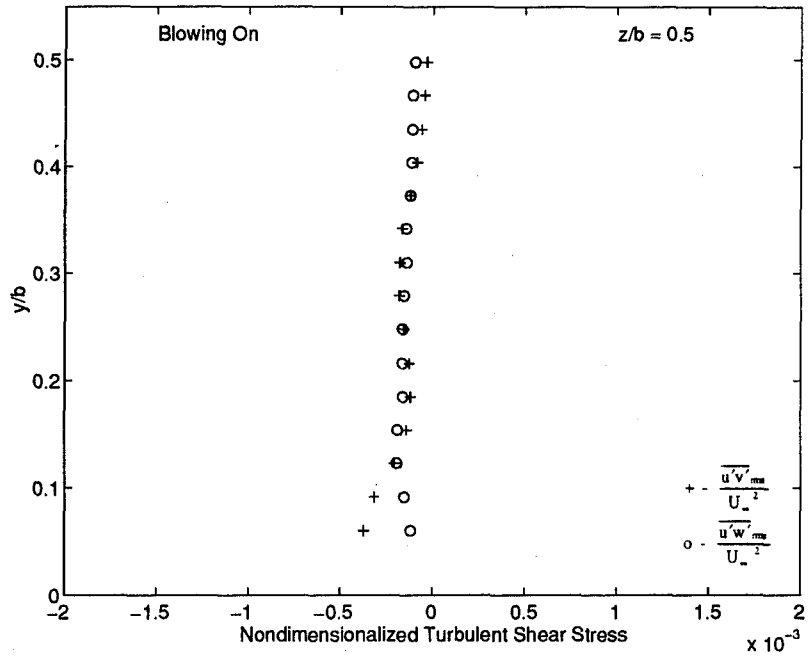


Figure 94. Turbulent Shear Stress Components Nondimensionalized by U_∞^2 - Blowing On,
 $z/b = 0.5$

Appendix A: Uncertainty Analysis

Experimental data is always subject to error introduced through the measurement and data reduction processes. The overall error in a measurement is a function of all the incremental errors introduced at each step in the measurement and analysis processes. It can be subdivided into two categories: bias error and random error. Bias error is characterized by a relatively constant shift of the measured value away from the actual value. It is a function of the accuracy of the measurement process; while bias error cannot be decreased by increasing the sample size, its effect can be largely eliminated post-test if its sign and approximate magnitude are known. Random error, on the other hand, represents the deviation of an instantaneous measurement from the mean measurement of a quantity; it is a function of the precision of the measurement process. It can be reduced by increasing the sample size.

Assume quantity q is a function of parameters a , b , and c . The error in q is then a function of errors in a , b , and c . The maximum error in q would be defined as:

$$E_q = \frac{\partial q}{\partial a} E_a + \frac{\partial q}{\partial b} E_b + \frac{\partial q}{\partial c} E_c + r_q \quad (A1)$$

where the partial derivatives are called the sensitivities of q to a , b , and c , respectively, and E_a , E_b , and E_c are the maximum elemental errors of a , b , and c . The final term, r_q , represents the random deviation of the measured quantity q from its mean value. Equation A1 gives a very pessimistic estimate of the error in q , though, since it assumes the errors in a , b , and c are all at their maximum values simultaneously. A more probable

estimate of the error is obtained by defining Eq as the root-sum-square (RSS) of the terms on the right side of equation A1:

$$E_q = \sqrt{\left(\frac{\partial q}{\partial a} E_a\right)^2 + \left(\frac{\partial q}{\partial b} E_b\right)^2 + \left(\frac{\partial q}{\partial c} E_c\right)^2 + r_q^2} \quad (A2)$$

All error estimates presented in this thesis used the RSS method of equation A2.

The elemental errors were estimated from data supplied by the manufacturers of the measurement equipment, experience, and observed results. Table A1 summarizes the elemental error values used throughout this error analysis

Table A1
Elemental Error Summary

Quantity	Error	Source
Pressure Transducer Accuracy	$\pm 0.5\%$ Full-Scale	Mfgr Data
Signal Conditioner Gain	$\pm 0.2\%$ Full-Scale	Mfgr Data
Data System Static Error	$\pm 0.25\%$ Full-Scale	Mfgr Data
Ambient Pressure Pa	± 0.01 PSI	Observed
Hot Film Anemometry System	$\pm 3.0\%$	Mfgr Data
Probe y-position	± 0.0145 in	Experience
Probe z-position	± 0.03 in	Experience

Random errors were estimated through statistical analysis of actual test data. The confidence interval is defined as the region around a measured value in which the true value lies with a known degree of uncertainty. Confidence intervals about a mean or a variance may be calculated through the following equations:

Confidence Interval About a Mean: $\bar{x} - \frac{s_x z_{\alpha/2}}{\sqrt{N}} \leq \mu_x \leq \bar{x} + \frac{s_x z_{\alpha/2}}{\sqrt{N}}$

Confidence Interval About a Variance: $\frac{ns^2}{\chi_{n;\alpha/2}^2} \leq \sigma_x^2 \leq \frac{ns^2}{\chi_{n;1-\alpha/2}^2}$

where \bar{x} is the estimated mean, s_x is the estimated sample standard deviation, s^2 is the estimated sample variance, N is the number of samples, $n = N-1$, z_α is the normal distribution function, $\chi_{n;\alpha}^2$ is the Chi-Square distribution function, μ_x is the true mean, and σ^2 is the true variance. The normal distribution function was used rather than the student-t distribution since more than 30 samples were taken at each station. 98% confidence intervals were calculated for each of the basic measured parameters: mean values of static and total pressure, hot-film probe output mean voltage \bar{V} , and hot-film probe output fluctuation rms voltage $\frac{V'_{rms}}{\bar{V}}$, realizing that rms is equivalent to variance. Results are summarized in Table A2.

Table A2
Confidence Interval Summary

Parameter	Confidence Interval (units)	Confidence Interval (%)
Total Pressure	± 0.12 psi	± 0.3
Static Pressure	± 0.06 psi	± 0.2
Hot-Film Mean Voltage \bar{V}	± 0.005 V	± 0.17
Hot-Film RMS Voltage $\frac{V'_{rms}}{\bar{V}}$	± 0.005	± 1.0

Note that the large number of samples used for analysis resulted in very small random errors.

With the information in Tables A1 and A2, RSS error estimates were obtained for all parameters presented in this thesis.

Rake Total Pressure: $P_T = P_T(y, z, P_a, \text{Transducer, Signal Conditioner, Data System, } r_{P_t})$:

Sensitivities:

$$\frac{\partial P_T}{\partial z} = 7.54 \text{ (psi / inch)} \quad \frac{\partial P_T}{\partial y} = 18.885 \text{ (psi / inch)} \quad \frac{\partial P_T}{\partial P_a} = 1.0 \text{ (psi / psi)}$$

$$\frac{\partial P_T}{\partial \text{trans.}} = 50 \text{ (psi / % fs)} \quad \frac{\partial P_T}{\partial \text{sig cond.}} = 50 \text{ (psi / % fs)} \quad \frac{\partial P_T}{\partial \text{data sys.}} = 50 \text{ (psi / % fs)}$$

RSS Error:

$$E_{PT} = \sqrt{(0.12)^2 + (7.54 \times 0.03)^2 + (18.885 \times 0.0145)^2 + (1 \times 0.01)^2 + (50 \times 0.005)^2 + (50 \times 0.002)^2 + (50 \times 0.0025)^2}$$

$$E_{PT} = \pm 0.478305 \text{ psi} \approx \pm 1.3 \text{ to } 1.5 \% \text{ of measured values}$$

Upstream Total Pressure: $P_{T0} = P_{T0}(P_a, \text{transducer, signal conditioner, data system})$

Sensitivities:

$$\frac{\partial P_T}{\partial P_a} = 1.0 \text{ (psi / psi)} \quad \frac{\partial P_T}{\partial \text{trans.}} = 50 \text{ (psi / % fs)} \quad \frac{\partial P_T}{\partial \text{sig cond.}} = 50 \text{ (psi / % fs)}$$

$$\frac{\partial P_T}{\partial \text{data sys.}} = 50 \text{ (psi / % fs)}$$

RSS Error:

$$E_{PT0} = \pm 0.364 \text{ psi} \approx \pm 1.0 \% \text{ of measured values}$$

Rake Static Pressure: $P_s = f(y, z, P_a, \text{Transducer, Signal Conditioner, Data System})$

Sensitivities:

$$\frac{\partial P_s}{\partial z} = 0.943 \text{ (psi / inch)} \quad \frac{\partial P_s}{\partial y} = 2.8275 \text{ (psi / inch)} \quad \frac{\partial P_s}{\partial P_a} = 1.0 \text{ (psi / psi)}$$

$$\frac{\partial P_s}{\partial \text{trans.}} = 50 \text{ (psi / % fs)} \quad \frac{\partial P_s}{\partial \text{sig cond.}} = 50 \text{ (psi / % fs)} \quad \frac{\partial P_s}{\partial \text{data sys.}} = 50 \text{ (psi / % fs)}$$

RSS Error:

$$E_{Ps} = \pm 0.307 \text{ psi} \approx \pm 1.0 \% \text{ of measured values}$$

Surface Static Pressure: $P_s = f(P_a, \text{Transducer, Signal Conditioner, Data System})$

Sensitivities:

$$\frac{\partial P_s}{\partial P_a} = 1.0 \text{ (psi / psi)} \quad \frac{\partial P_s}{\partial \text{trans.}} = 50 \text{ (psi / % fs)} \quad \frac{\partial P_s}{\partial \text{sig cond.}} = 50 \text{ (psi / % fs)}$$

$$\frac{\partial P_s}{\partial \text{data sys.}} = 50 \text{ (psi / % fs)}$$

RSS Error:

$$E_{P_s} \approx \pm 0.303 \text{ psi} \approx \pm 1.0 \% \text{ of measured values}$$

Total Pressure Recovery: $r_d = f(P_T, P_{T0})$

Governing Equation and Derivation:

$$dr_d = \frac{\partial r_d}{\partial P_T} dP_T + \frac{\partial r_d}{\partial P_{T0}} dP_{T0}$$

$$dr_d \approx \frac{1}{P_{T0}} \Delta P_T - \frac{P_T}{P_{T0}^2} \Delta P_{T0}$$

$$dr_d \approx r_d \frac{\Delta P_T}{P_T} - r_d \frac{\Delta P_{T0}}{P_{T0}}$$

$$\text{then } E_{rd} \approx \sqrt{\left(r_d \frac{\Delta P_T}{P_T} \right)^2 + \left(r_d \frac{\Delta P_{T0}}{P_{T0}} \right)^2} \quad (\text{A3})$$

Equation (A3) can be evaluated using uncertainties for P_T and P_{T0} calculated above.

RSS Error:

$$E_{rd} \approx \sqrt{(0.98 \times 0.015)^2 + (0.98 \times 0.01)^2} \approx \pm 0.018 \approx 1.8\% \text{ of measured value}$$

Static Pressure Recovery: $r_s = f(P_s, P_{T0})$

Governing Equation: Derived as above.

$$E_{rs} \approx \sqrt{\left(r_d \frac{\Delta P_s}{P_s}\right)^2 + \left(r_d \frac{\Delta P_{T0}}{P_{T0}}\right)^2}$$

RSS Error:

$$E_{rs} = \pm 0.012 \approx \pm 1.4 \% \text{ of measured values}$$

Pitot-Static Mach Number: $M = f(P_T, P_s)$

Governing Equation: Derived from:

$$\frac{P_T}{P_s} = \left(1 + \frac{\gamma - 1}{2} M^2\right)^{\frac{\gamma}{\gamma - 1}}$$

for $\gamma=1.4$, giving:

$$dM = \frac{1}{2} \left(5 \left(\frac{P_T}{P_s} \right)^{0.286} - 5 \right)^{\frac{1}{2}} \left[\frac{1.43}{P_s^{0.286} P_{T0}^{0.714}} dP_T + \frac{1.43 P_T^{0.286}}{P_s^{1.286}} dP_s \right]$$

RSS Error:

$$E_M \approx \pm 0.03$$

Hot-Film Mean Velocity: $\bar{u} = f(y, z, \text{anemometer}, \bar{V})$

Supplimental Equation: Derive dependency on anemometer and mean voltage:

$$\bar{u} = a(\bar{V})$$

$$\bar{u} + d\bar{u} = (a + da)(\bar{V} + d\bar{V})$$

$$\bar{u} + \Delta\bar{u} \approx a\bar{V} + a\Delta\bar{V} + \Delta a\bar{V} + \Delta a\Delta\bar{V}$$

neglecting second - order terms,

$$\bar{u} + \Delta\bar{u} \approx a\bar{V} \left(1 + \frac{\Delta\bar{V}}{\bar{V}} + \frac{\Delta a}{a} \right)$$

$$\bar{u} + \Delta\bar{u} \approx a\bar{V}(1 + 0.001 + 0.03)$$

$$\Delta\bar{u} = 0.031\bar{u}$$

This shows that the anemometer calibration error and random error combine to give up to $\pm 3.1\%$ error in \bar{u} . Calculate other error sources on a percentage basis as well.

Sensitivities:

$$\frac{\partial \frac{\Delta\bar{u}}{\bar{u}}}{\partial y} \approx 3.36 \text{ (% per inch)} \quad \frac{\partial \frac{\Delta\bar{u}}{\bar{u}}}{\partial z} \approx 0.625 \text{ (% per inch)}$$

RSS Error:

$$E_{\frac{\Delta\bar{u}}{\bar{u}}} \approx \sqrt{(3.36 \times 0.0145)^2 + (0.625 \times 0.03)^2 + (0.031)^2 + (0.0025)^2}$$

$$E_{\frac{\Delta\bar{u}}{\bar{u}}} \approx 0.061, \text{ so } E_{\bar{u}} \approx \pm 6.1\% \text{ of measured value}$$

Assume that error for other mean velocity components is similar.

Turbulence Intensity: $\frac{u'_{rms}}{\bar{u}} = f(y, z, \text{anemometer}, \frac{V'_{rms}}{\bar{V}})$

Supplimental Equation: Dependency on anemometer and $\frac{V'_{rms}}{\bar{V}}$ derived in a similar

fashion as above:

$$\frac{u'_{rms}}{\bar{u}} + \Delta \frac{u'_{rms}}{\bar{u}} \approx a \frac{V'_{rms}}{\bar{V}} \left(1 + \Delta \frac{V'_{rms}}{\bar{V}} + \frac{\Delta a}{a} \right) \approx 1.04 \frac{u'_{rms}}{\bar{u}}$$

For turbulence intensity, the combination of anemometer calibration error and random error total +4.0% of the measured value. Again, calculate other error sources in terms of percent as well.

Sensitivities:

$$\frac{\partial \frac{\Delta \frac{u'_{rms}}{\bar{u}}}{\frac{u'_{rms}}{\bar{u}}}}{\partial y} \approx 6.875 \text{ (% per inch)} \quad \frac{\partial \frac{\Delta \frac{u'_{rms}}{\bar{u}}}{\frac{u'_{rms}}{\bar{u}}}}{\partial z} \approx 3.4375 \text{ (% per inch)}$$

RSS Error:

$$E_{\frac{\Delta \frac{u'_{rms}}{\bar{u}}}{\frac{u'_{rms}}{\bar{u}}}} \approx \pm 0.119 \approx \pm 11.9\% \text{ of measured value}$$

Assume that RSS error for other turbulence intensity components is similar.

$$\text{Turbulent Shear Stress: } TSS = f\left(\frac{u'_{rms}}{u}, \frac{v'_{rms}}{u}\right)$$

Each turbulent shear stress component can be interpreted as the product of two turbulence

intensity terms: $\frac{\overline{u'v'}_{rms}}{u^2} \approx \frac{u'_{rms}}{u} \times \frac{v'_{rms}}{u}$. Then,

$$E_{TSS} \approx \sqrt{2E_{\frac{u'_{rms}}{u}}} \approx 0.168 \approx 16.8\% \text{ of measured value.}$$

$$\text{Turbulent Kinetic Energy: } TKE = f\left(\frac{u'_{rms}}{u}, \frac{v'_{rms}}{u}, \frac{w'_{rms}}{u}\right)$$

In a similar manner as described for turbulent shear stress,

$$E_{TKE} \approx \sqrt{3E_{\frac{u'_{rms}}{u}}} \approx 0.206 \approx 20.6\% \text{ of measured value.}$$

Appendix B: Test Run Log

Data was taken between July and October, 1994. Sample rates, sweep increments, and dwell times at each measurement station were adjusted as experience unveiled better choices for these parameters. The narrative which follows details the particulars for each run in chronological order.

Data Set A: This initial set of exit plane data was collected before the upstream pitot tube was installed. It showed that even the small variations in total pressure between runs made it impossible to correlate data taken at adjacent spanwise locations, so this data was discarded.

Data Sets B - E: These sets of data provided baseline information on the total pressure at the inlet and exit planes at $M_1 = 0.6$ and $M_1 = 0.8$. Data was collected every 0.254 cm (0.1 in) across the span, between $z = 0.254$ cm and $z = 2.286$ cm (0.9 in). Data in the y-direction was spaced every 0.397 mm (1/64 in), beginning with the total pressure rake in contact with the test section floor. This placed the center of the pitot port 0.737 mm (0.0290 in) above the floor. Exit plane sweeps consisted of 58 steps, while entrance plane sweeps consisted of 33 steps. Dwell time at each station was approximately 10 seconds. Lower surface static pressure data was taken during these runs as well. All pressure measurements were sampled at 20 Hz.

Flow Visualization 1: The first set of surface flow visualization data was acquired next. This was for the no-blowing case, and was useful in determining the separation location for installation of the VGJ's.

Data Sets F through H: These sets collected normal-film probe data at $z = 0.762$ cm (0.3 in), 1.27 cm (0.5 in), and 1.778 cm (0.7 in) on the exit plane at $M_1 = 0.6$. Sweeps started with the sensing wire 0.737 mm (0.0290 in) above the test section lower surface, and proceeded in 0.794 mm (1/32 in) increments for 16 steps. Hot film data in sets F and G was collected at 200 KHz, while set H was collected at 200 KHz but then filtered to 30 KHz. 0.25 seconds of hot film data was collected at each measurement station. surface static and upstream total pressure data taken simultaneously was sampled at 50 Hz. At some point during these sets of runs, the upstream pitot was bent to an angle of about 30° to the flow, towards the $z = 0$ sidewall, making this whole group of data suspect.

Data Set J: A partial set of normal-film probe data was collected at $z = 0.762$ cm on the exit plane at $M_1 = 0.8$. The short life of the probe due to extreme vibration at this condition led to the abandoning of any further tests at $M_1 = 0.8$.

Data Sets K through N, P, and Q: These runs gave baseline cross-film probe data at the exit plane. Sweeps began at $y = 0.153$ cm (0.06025 in) above the test section floor and continued in 0.794 mm (1/32 in) increments for 15 steps. 0.25 seconds of hot film data were recorded at each point at a sample rate of 50 KHz. Upstream total

pressure and exit plane lower surface static pressure data was sampled for 1 second at 50 Hz. The initial probe height setting for these runs was somewhat inaccurate, resulting in unacceptable scatter in some of this data.

Flow Visualization 2: Flow visualization tests were repeated with VGJ's installed to evaluate the effect of blowing on the surface flow pattern. Comparison of blowing-off results with those from the first set of flow visualization data showed that the new build of the model gave a much more symmetrical surface flow pattern.

Data Set R: These runs investigated the effect of several blowing mass flow rates on the total pressure recovery profiles at the exit plane. Blowing off data was recollected back-to-back with the blowing on data to ensure a valid comparison. Pressure data was sampled at 50 Hz. Sweeps were performed at the same spanwise stations as in runs B through E. They again began with the pitot in contact with the lower surface, but now proceeded in 0.794 mm (1/32 in) increments for 29 steps. Dwell time at each station remained 10 seconds.

Data Set S: The static pressure field at the exit plane was mapped during this set. Sweep and sampling parameters were as for set R, but data was collected at only 5 of the spanwise stations, spaced 0.508 cm (0.2 in) apart. Blowing on and blowing off data was collected. Additionally, one blowing-off sweep was performed on the centerline at the inlet plane.

Data Sets T through Z, A*, 1 through 4: These sets produced blowing on and blowing off cross-film probe data at the three spanwise hot-film measurement locations on the exit plane. Initial probe height, step increment, and number of steps were identical to the earlier cross-wire data sets, but a repeatable method for setting the initial height was employed. Hot film signals were sampled at 100 KHz for 0.2 seconds at each measurement station. Pressure data was again sampled at 50 Hz for 1 second.

Data Set 5: This data set collected cross-film data in the xz-plane at $z = 1.778 \text{ cm}$ (0.7 in) with blowing off as a repeatability check. Sweep and sampling parameters were as described in the preceding paragraph.

The table which follows lists all of the diffuser test runs from which data was collected and stored.

Table B1

Run Log

Run Number	M_o	z/b	Type	Inlet/Exit	Date	Blowing
A01	0.6	0.5	Pt 58 step	Exit	5-Jul-94	Off
A02	0.6	0.5	Pt 58 step	Exit	5-Jul-94	Off
A03	0.6	0.5	Pt 58 step	Exit	6-Jul-94	Off
A04	0.6	0.5	Pt 58 step	Exit	6-Jul-94	Off
A05	0.6	0.5	Pt 58 step	Exit	7-Jul-94	Off
A06	0.6	0.6	Pt 58 step	Exit	7-Jul-94	Off
A07	0.6	0.7	Pt 58 step	Exit	7-Jul-94	Off
A08	0.6	0.8	Pt 58 step	Exit	7-Jul-94	Off
A09	0.6	0.9	Pt 58 step	Exit	7-Jul-94	Off
A10	0.6	0.4	Pt 58 step	Exit	7-Jul-94	Off
A11	0.6	0.3	Pt 58 step	Exit	7-Jul-94	Off
A12	0.6	0.2	Pt 58 step	Exit	7-Jul-94	Off

Run Number	M_∞	z/b	Type	Inlet/Exit	Date	Blowing
A13	0.6	0.1	Pt 58 step	Exit	7-Jul-94	Off
B01	0.6	0.5	Pt 58 step	Exit	8-Jul-94	Off
B02	0.6	0.5	Pt 58 step	Exit	12-Jul-94	Off
B03	0.6	0.5	Pt 58 step	Exit	12-Jul-94	Off
B03	0.6	0.5	Pt 58 step	Exit	12-Jul-94	Off
B04	0.6	0.4	Pt 58 step	Exit	12-Jul-94	Off
B05	0.6	0.3	Pt 58 step	Exit	12-Jul-94	Off
B06	0.6	0.2	Pt 58 step	Exit	12-Jul-94	Off
B07	0.6	0.1	Pt 58 step	Exit	12-Jul-94	Off
B08	0.6	0.1	Pt 58 step	Exit	13-Jul-94	Off
B09	0.6	0.2	Pt 58 step	Exit	13-Jul-94	Off
B10	0.6	0.3	Pt 58 step	Exit	13-Jul-94	Off
B11	0.6	0.4	Pt 58 step	Exit	13-Jul-94	Off
B12	0.6	0.5	Pt 58 step	Exit	13-Jul-94	Off
B13	0.6	0.6	Pt 58 step	Exit	13-Jul-94	Off
B14	0.6	0.7	Pt 58 step	Exit	13-Jul-94	Off
B15	0.6	0.8	Pt 58 step	Exit	13-Jul-94	Off
B16	0.6	0.9	Pt 58 step	Exit	13-Jul-94	Off
B17	0.6	0.9	Pt 58 step	Exit	15-Jul-94	Off
B18	0.6	0.9	Pt 58 step	Exit	15-Jul-94	Off
B19	0.6	0.5	Pt 58 step	Exit	18-Jul-94	Off
B20	0.6	0.5	Pt 58 step	Exit	18-Jul-94	Off
B21	0.6	0.4	Pt 58 step	Exit	18-Jul-94	Off
B22	0.6	0.3	Pt 58 step	Exit	18-Jul-94	Off
B23	0.6	0.2	Pt 58 step	Exit	18-Jul-94	Off
B24	0.6	0.1	Pt 58 step	Exit	18-Jul-94	Off
B25	0.6	0.6	Pt 58 step	Exit	18-Jul-94	Off
B26	0.6	0.7	Pt 58 step	Exit	18-Jul-94	Off
B27	0.6	0.8	Pt 58 step	Exit	18-Jul-94	Off
B28	0.6	0.9	Pt 58 step	Exit	18-Jul-94	Off
C01	0.6	0.5	Pt 58 step	Inlet	19-Jul-94	Off
C02	0.6	0.4	Pt 58 step	Inlet	19-Jul-94	Off
C03	0.6	0.3	Pt 58 step	Inlet	19-Jul-94	Off
C04	0.6	0.2	Pt 58 step	Inlet	19-Jul-94	Off
C05	0.6	0.1	Pt 58 step	Inlet	19-Jul-94	Off
C06	0.6	0.6	Pt 58 step	Inlet	19-Jul-94	Off
C07	0.6	0.7	Pt 58 step	Inlet	19-Jul-94	Off
C08	0.6	0.8	Pt 58 step	Inlet	19-Jul-94	Off
C09	0.6	0.9	Pt 58 step	Inlet	19-Jul-94	Off
D01	0.8	0.8	Pt 58 step	Inlet	19-Jul-94	Off
D02	0.8	0.5	Pt 58 step	Inlet	19-Jul-94	Off
D03	0.8	0.4	Pt 58 step	Inlet	19-Jul-94	Off
D04	0.8	0.4	Pt 58 step	Inlet	19-Jul-94	Off
D05	0.8	0.3	Pt 58 step	Inlet	19-Jul-94	Off
D06	0.8	0.2	Pt 58 step	Inlet	19-Jul-94	Off

Run Number	M _o	z/b	Type	Inlet/Exit	Date	Blowing
D07	0.8	0.1	Pt 58 step	Inlet	19-Jul-94	Off
D08	0.8	0.6	Pt 58 step	Inlet	19-Jul-94	Off
D09	0.8	0.7	Pt 58 step	Inlet	19-Jul-94	Off
D10	0.8	0.8	Pt 58 step	Inlet	19-Jul-94	Off
D11	0.8	0.9	Pt 58 step	Inlet	19-Jul-94	Off
E01	0.8	0.5	Pt 58 step	Exit	20-Jul-94	Off
E02	0.8	0.4	Pt 58 step	Exit	20-Jul-94	Off
E03	0.8	0.3	Pt 58 step	Exit	20-Jul-94	Off
E04	0.8	0.2	Pt 58 step	Exit	20-Jul-94	Off
E05	0.8	0.1	Pt 58 step	Exit	20-Jul-94	Off
E06	0.8	0.6	Pt 58 step	Exit	20-Jul-94	Off
E07	0.8	0.7	Pt 58 step	Exit	20-Jul-94	Off
E08	0.8	0.8	Pt 58 step	Exit	20-Jul-94	Off
E09	0.8	0.9	Pt 58 step	Exit	20-Jul-94	Off
B29	0.6	0.8	Pt 58 step	Exit	25-Jul-94	Off
B30	0.6	0.5	Pt 58 step	Exit	25-Jul-94	Off
C10	0.6	0.5	Pt 58 step	Inlet	25-Jul-94	Off
C11	0.6	0.1	Pt 58 step	Inlet	25-Jul-94	Off
C12	0.6	0.5	Pt 58 step	Inlet	25-Jul-94	Off
C13	0.6	0.1	Pt 58 step	Inlet	25-Jul-94	Off
F01	0.6	0.5	normal wire	Exit	24-Aug-94	Off
F02	0.6	0.5	normal wire	Exit	24-Aug-94	Off
F03	0.6	0.5	normal wire	Exit	24-Aug-94	Off
F04	0.6	0.5	normal wire	Exit	24-Aug-94	Off
F05	0.6	0.5	normal wire	Exit	24-Aug-94	Off
F06	0.6	0.5	normal wire	Exit	24-Aug-94	Off
F07	0.6	0.5	normal wire	Exit	24-Aug-94	Off
F08	0.6	0.5	normal wire	Exit	24-Aug-94	Off
F09	0.6	0.5	normal wire	Exit	24-Aug-94	Off
F10	0.6	0.5	normal wire	Exit	24-Aug-94	Off
F11	0.6	0.5	normal wire	Exit	24-Aug-94	Off
F12	0.6	0.5	normal wire	Exit	24-Aug-94	Off
F13	0.6	0.5	normal wire	Exit	24-Aug-94	Off
F14	0.6	0.5	normal wire	Exit	24-Aug-94	Off
F15	0.6	0.5	normal wire	Exit	24-Aug-94	Off
F16	0.6	0.5	normal wire	Exit	24-Aug-94	Off
F17	0.6	0.5	normal wire	Exit	24-Aug-94	Off
F18	0.6	0.5	normal wire	Exit	24-Aug-94	Off
F19	0.6	0.5	normal wire	Exit	24-Aug-94	Off
F20	0.6	0.5	normal wire	Exit	24-Aug-94	Off
F21	0.6	0.5	normal wire	Exit	24-Aug-94	Off
F22	0.6	0.5	normal wire	Exit	24-Aug-94	Off
F23	0.6	0.5	normal wire	Exit	24-Aug-94	Off
F24	0.6	0.5	normal wire	Exit	24-Aug-94	Off
F25	0.6	0.5	normal wire	Exit	24-Aug-94	Off

Run Number	M_∞	z/b	Type	Inlet/Exit	Date	Blowing
F26	0.6	0.5	normal wire	Exit	24-Aug-94	Off
F27	0.6	0.5	normal wire	Exit	24-Aug-94	Off
F28	0.6	0.5	normal wire	Exit	24-Aug-94	Off
F29	0.6	0.5	normal wire	Exit	24-Aug-94	Off
F30	0.6	0.5	normal wire	Exit	24-Aug-94	Off
F32	0.6	0.5	normal wire	Exit	24-Aug-94	Off
G10	0.6	0.3	normal wire	Exit	24-Aug-94	Off
G11	0.6	0.3	normal wire	Exit	24-Aug-94	Off
G12	0.6	0.3	normal wire	Exit	24-Aug-94	Off
G13	0.6	0.3	normal wire	Exit	24-Aug-94	Off
G14	0.6	0.3	normal wire	Exit	24-Aug-94	Off
G15	0.6	0.3	normal wire	Exit	24-Aug-94	Off
G16	0.6	0.3	normal wire	Exit	24-Aug-94	Off
G17	0.6	0.3	normal wire	Exit	24-Aug-94	Off
G18	0.6	0.3	normal wire	Exit	24-Aug-94	Off
G19	0.6	0.3	normal wire	Exit	24-Aug-94	Off
G20	0.6	0.3	normal wire	Exit	24-Aug-94	Off
G21	0.6	0.3	normal wire	Exit	24-Aug-94	Off
G22	0.6	0.3	normal wire	Exit	24-Aug-94	Off
G23	0.6	0.3	normal wire	Exit	24-Aug-94	Off
G24	0.6	0.3	normal wire	Exit	24-Aug-94	Off
G25	0.6	0.3	normal wire	Exit	24-Aug-94	Off
G26	0.6	0.3	normal wire	Exit	24-Aug-94	Off
H01	0.6	0.7	normal wire	Exit	24-Aug-94	Off
H02	0.6	0.7	normal wire	Exit	24-Aug-94	Off
H03	0.6	0.7	normal wire	Exit	24-Aug-94	Off
H04	0.6	0.7	normal wire	Exit	24-Aug-94	Off
H05	0.6	0.7	normal wire	Exit	24-Aug-94	Off
H06	0.6	0.7	normal wire	Exit	24-Aug-94	Off
H07	0.6	0.7	normal wire	Exit	24-Aug-94	Off
H08	0.6	0.7	normal wire	Exit	24-Aug-94	Off
H09	0.6	0.7	normal wire	Exit	24-Aug-94	Off
H10	0.6	0.7	normal wire	Exit	24-Aug-94	Off
H11	0.6	0.7	normal wire	Exit	24-Aug-94	Off
H12	0.6	0.7	normal wire	Exit	24-Aug-94	Off
H13	0.6	0.7	normal wire	Exit	24-Aug-94	Off
H14	0.6	0.7	normal wire	Exit	24-Aug-94	Off
H15	0.6	0.7	normal wire	Exit	24-Aug-94	Off
H16	0.6	0.7	normal wire	Exit	24-Aug-94	Off
J01	0.8	0.3	UV-Wire	Exit	24-Aug-94	Off
J02	0.8	0.3	UV-Wire	Exit	24-Aug-94	Off
J03	0.8	0.3	UV-Wire	Exit	24-Aug-94	Off
J04	0.8	0.3	UV-Wire	Exit	24-Aug-94	Off
J05	0.8	0.3	UV-Wire	Exit	24-Aug-94	Off
J06	0.8	0.3	UV-Wire	Exit	24-Aug-94	Off

Run Number	M _o	z/b	Type	Inlet/Exit	Date	Blowing
J07	0.8	0.3	UV-Wire	Exit	24-Aug-94	Off
J08	0.8	0.3	UV-Wire	Exit	24-Aug-94	Off
J09	0.8	0.3	UV-Wire	Exit	24-Aug-94	Off
K01	0.6	0.5	UV-Wire	Exit	31-Aug-94	Off
K03	0.6	0.5	UV-Wire	Exit	31-Aug-94	Off
K04	0.6	0.5	UV-Wire	Exit	31-Aug-94	Off
K05	0.6	0.5	UV-Wire	Exit	31-Aug-94	Off
K06	0.6	0.5	UV-Wire	Exit	31-Aug-94	Off
K07	0.6	0.5	UV-Wire	Exit	31-Aug-94	Off
K08	0.6	0.5	UV-Wire	Exit	31-Aug-94	Off
K09	0.6	0.5	UV-Wire	Exit	31-Aug-94	Off
K10	0.6	0.5	UV-Wire	Exit	31-Aug-94	Off
K11	0.6	0.5	UV-Wire	Exit	31-Aug-94	Off
K12	0.6	0.5	UV-Wire	Exit	31-Aug-94	Off
K13	0.6	0.5	UV-Wire	Exit	31-Aug-94	Off
K14	0.6	0.5	UV-Wire	Exit	31-Aug-94	Off
K15	0.6	0.5	UV-Wire	Exit	31-Aug-94	Off
L01	0.6	0.3	UV-Wire	Exit	31-Aug-94	Off
L02	0.6	0.3	UV-Wire	Exit	31-Aug-94	Off
L03	0.6	0.3	UV-Wire	Exit	31-Aug-94	Off
L04	0.6	0.3	UV-Wire	Exit	31-Aug-94	Off
L05	0.6	0.3	UV-Wire	Exit	31-Aug-94	Off
L06	0.6	0.3	UV-Wire	Exit	31-Aug-94	Off
L07	0.6	0.3	UV-Wire	Exit	31-Aug-94	Off
L08	0.6	0.3	UV-Wire	Exit	31-Aug-94	Off
L09	0.6	0.3	UV-Wire	Exit	31-Aug-94	Off
L10	0.6	0.3	UV-Wire	Exit	31-Aug-94	Off
L11	0.6	0.3	UV-Wire	Exit	31-Aug-94	Off
L12	0.6	0.3	UV-Wire	Exit	31-Aug-94	Off
L13	0.6	0.3	UV-Wire	Exit	31-Aug-94	Off
L14	0.6	0.3	UV-Wire	Exit	31-Aug-94	Off
L15	0.6	0.3	UV-Wire	Exit	31-Aug-94	Off
M01	0.6	0.7	UV-Wire	Exit	31-Aug-94	Off
M02	0.6	0.7	UV-Wire	Exit	31-Aug-94	Off
M03	0.6	0.7	UV-Wire	Exit	31-Aug-94	Off
M04	0.6	0.7	UV-Wire	Exit	31-Aug-94	Off
M05	0.6	0.7	UV-Wire	Exit	31-Aug-94	Off
M06	0.6	0.7	UV-Wire	Exit	31-Aug-94	Off
M07	0.6	0.7	UV-Wire	Exit	31-Aug-94	Off
M08	0.6	0.7	UV-Wire	Exit	31-Aug-94	Off
M09	0.6	0.7	UV-Wire	Exit	31-Aug-94	Off
M10	0.6	0.7	UV-Wire	Exit	31-Aug-94	Off
M11	0.6	0.7	UV-Wire	Exit	31-Aug-94	Off
M12	0.6	0.7	UV-Wire	Exit	31-Aug-94	Off
M13	0.6	0.7	UV-Wire	Exit	31-Aug-94	Off

Run Number	M ₀	z/b	Type	Inlet/Exit	Date	Blowing
M14	0.6	0.7	UV-Wire	Exit	31-Aug-94	Off
M15	0.6	0.7	UV-Wire	Exit	31-Aug-94	Off
N01	0.6	0.5	UW-Wire	Exit	1-Sep-94	Off
N02	0.6	0.5	UW-Wire	Exit	1-Sep-94	Off
N03	0.6	0.5	UW-Wire	Exit	1-Sep-94	Off
N04	0.6	0.5	UW-Wire	Exit	1-Sep-94	Off
N05	0.6	0.5	UW-Wire	Exit	1-Sep-94	Off
N06	0.6	0.5	UW-Wire	Exit	1-Sep-94	Off
N07	0.6	0.5	UW-Wire	Exit	1-Sep-94	Off
N08	0.6	0.5	UW-Wire	Exit	1-Sep-94	Off
N09	0.6	0.5	UW-Wire	Exit	1-Sep-94	Off
N10	0.6	0.5	UW-Wire	Exit	1-Sep-94	Off
N11	0.6	0.5	UW-Wire	Exit	1-Sep-94	Off
N12	0.6	0.5	UW-Wire	Exit	1-Sep-94	Off
N13	0.6	0.5	UW-Wire	Exit	1-Sep-94	Off
N14	0.6	0.5	UW-Wire	Exit	1-Sep-94	Off
N15	0.6	0.5	UW-Wire	Exit	1-Sep-94	Off
P01	0.6	0.3	UW-Wire	Exit	1-Sep-94	Off
P02	0.6	0.3	UW-Wire	Exit	1-Sep-94	Off
P03	0.6	0.3	UW-Wire	Exit	1-Sep-94	Off
P04	0.6	0.3	UW-Wire	Exit	1-Sep-94	Off
P05	0.6	0.3	UW-Wire	Exit	1-Sep-94	Off
P06	0.6	0.3	UW-Wire	Exit	1-Sep-94	Off
P07	0.6	0.3	UW-Wire	Exit	1-Sep-94	Off
P08	0.6	0.3	UW-Wire	Exit	1-Sep-94	Off
P09	0.6	0.3	UW-Wire	Exit	1-Sep-94	Off
P10	0.6	0.3	UW-Wire	Exit	1-Sep-94	Off
P11	0.6	0.3	UW-Wire	Exit	1-Sep-94	Off
P12	0.6	0.3	UW-Wire	Exit	1-Sep-94	Off
P13	0.6	0.3	UW-Wire	Exit	1-Sep-94	Off
P14	0.6	0.3	UW-Wire	Exit	1-Sep-94	Off
P15	0.6	0.3	UW-Wire	Exit	1-Sep-94	Off
Q01	0.6	0.7	UW-Wire	Exit	1-Sep-94	Off
Q02	0.6	0.7	UW-Wire	Exit	1-Sep-94	Off
Q03	0.6	0.7	UW-Wire	Exit	1-Sep-94	Off
Q04	0.6	0.7	UW-Wire	Exit	1-Sep-94	Off
Q05	0.6	0.7	UW-Wire	Exit	1-Sep-94	Off
Q06	0.6	0.7	UW-Wire	Exit	1-Sep-94	Off
Q07	0.6	0.7	UW-Wire	Exit	1-Sep-94	Off
Q08	0.6	0.7	UW-Wire	Exit	1-Sep-94	Off
Q09	0.6	0.7	UW-Wire	Exit	1-Sep-94	Off
Q10	0.6	0.7	UW-Wire	Exit	1-Sep-94	Off
Q11	0.6	0.7	UW-Wire	Exit	1-Sep-94	Off
Q12	0.6	0.7	UW-Wire	Exit	1-Sep-94	Off
Q13	0.6	0.7	UW-Wire	Exit	1-Sep-94	Off

Run Number	M_∞	z/b	Type	Inlet/Exit	Date	Blowing
Q14	0.6	0.7	UW-Wire	Exit	1-Sep-94	Off
Q15	0.6	0.7	UW-Wire	Exit	1-Sep-94	Off
R01	0.6	0.5	Pt 29 step	Exit	7-Sep-94	Off
R02	0.6	0.5	Pt 29 step	Exit	7-Sep-94	0.0025
R03	0.6	0.5	Pt 29 step	Exit	8-Sep-94	Off
R04	0.6	0.5	Pt 29 step	Exit	9-Sep-94	Off
R05	0.6	0.5	Pt 29 step	Exit	9-Sep-94	0.0025
R06	0.6	0.5	Pt 29 step	Exit	9-Sep-94	0.0030
R07	0.6	0.5	Pt 29 step	Exit	9-Sep-94	0.0020
R08	0.6	0.3	Pt 29 step	Exit	9-Sep-94	Off
R09	0.6	0.3	Pt 29 step	Exit	9-Sep-94	0.0025
R10	0.6	0.3	Pt 29 step	Exit	9-Sep-94	0.0030
R11	0.6	0.3	Pt 29 step	Exit	9-Sep-94	0.0020
R12	0.6	0.3	Pt 29 step	Exit	12-Sep-94	Off
R13	0.6	0.3	Pt 29 step	Exit	12-Sep-94	0.0025
R14	0.6	0.7	Pt 29 step	Exit	12-Sep-94	Off
R15	0.6	0.7	Pt 29 step	Exit	12-Sep-94	0.0025
R16	0.6	0.7	Pt 29 step	Exit	12-Sep-94	0.0030
R17	0.6	0.7	Pt 29 step	Exit	12-Sep-94	0.0020
R18	0.6	0.7	Pt 29 step	Exit	14-Sep-94	0.0048
R19	0.6	0.3	Pt 29 step	Exit	14-Sep-94	0.0048
R20	0.6	0.7	Pt 29 step	Exit	14-Sep-94	0.0048
R21	0.6	0.6	Pt 29 step	Exit	15-Sep-94	0.0048
R22	0.6	0.6	Pt 29 step	Exit	15-Sep-94	Off
R23	0.6	0.4	Pt 29 step	Exit	15-Sep-94	Off
R24	0.6	0.4	Pt 29 step	Exit	15-Sep-94	0.0048
R25	0.6	0.2	Pt 29 step	Exit	15-Sep-94	0.0048
R26	0.6	0.2	Pt 29 step	Exit	15-Sep-94	Off
R27	0.6	0.1	Pt 29 step	Exit	15-Sep-94	Off
R28	0.6	0.1	Pt 29 step	Exit	15-Sep-94	Off
R29	0.6	0.1	Pt 29 step	Exit	15-Sep-94	0.0048
R30	0.6	0.8	Pt 29 step	Exit	15-Sep-94	Off
R31	0.6	0.8	Pt 29 step	Exit	15-Sep-94	0.0048
R32	0.6	0.9	Pt 29 step	Exit	15-Sep-94	Off
R33	0.6	0.9	Pt 29 step	Exit	15-Sep-94	0.0048
R34	0.6	0.9	Pt 29 step	Exit	15-Sep-94	Off
S01	0.6	0.5	Ps 29 step	Exit	15-Sep-94	Off
S02	0.6	0.5	Ps 29 step	Exit	15-Sep-94	0.0048
S03	0.6	0.3	Ps 29 step	Exit	15-Sep-94	Off
S04	0.6	0.3	Ps 29 step	Exit	15-Sep-94	0.0048
S05	0.6	0.7	Ps 29 step	Exit	15-Sep-94	Off
S06	0.6	0.7	Ps 29 step	Exit	15-Sep-94	0.0048
S07	0.6	0.9	Ps 29 step	Exit	15-Sep-94	Off
S08	0.6	0.9	Ps 29 step	Exit	15-Sep-94	0.0048
S09	0.6	0.1	Ps 29 step	Exit	15-Sep-94	Off

Run Number	M ₀	z/b	Type	Inlet/Exit	Date	Blowing
S10	0.6	0.1	Ps 29 step	Exit	15-Sep-94	0.0048
T01	0.6	0.3	UV-Wire	Exit	21-Sep-94	Off
T02	0.6	0.3	UV-Wire	Exit	21-Sep-94	Off
T03	0.6	0.3	UV-Wire	Exit	21-Sep-94	Off
T04	0.6	0.3	UV-Wire	Exit	21-Sep-94	Off
T05	0.6	0.3	UV-Wire	Exit	21-Sep-94	Off
T06	0.6	0.3	UV-Wire	Exit	21-Sep-94	Off
T07	0.6	0.3	UV-Wire	Exit	21-Sep-94	Off
T08	0.6	0.3	UV-Wire	Exit	21-Sep-94	Off
T09	0.6	0.3	UV-Wire	Exit	21-Sep-94	Off
T10	0.6	0.3	UV-Wire	Exit	21-Sep-94	Off
T11	0.6	0.3	UV-Wire	Exit	21-Sep-94	Off
T12	0.6	0.3	UV-Wire	Exit	21-Sep-94	Off
T13	0.6	0.3	UV-Wire	Exit	21-Sep-94	Off
T14	0.6	0.3	UV-Wire	Exit	21-Sep-94	Off
T15	0.6	0.3	UV-Wire	Exit	21-Sep-94	Off
U01	0.6	0.3	UV-Wire	Exit	21-Sep-94	0.0048
U02	0.6	0.3	UV-Wire	Exit	21-Sep-94	0.0048
U03	0.6	0.3	UV-Wire	Exit	21-Sep-94	0.0048
U04	0.6	0.3	UV-Wire	Exit	21-Sep-94	0.0048
U05	0.6	0.3	UV-Wire	Exit	21-Sep-94	0.0048
U06	0.6	0.3	UV-Wire	Exit	21-Sep-94	0.0048
U07	0.6	0.3	UV-Wire	Exit	21-Sep-94	0.0048
U08	0.6	0.3	UV-Wire	Exit	21-Sep-94	0.0048
U09	0.6	0.3	UV-Wire	Exit	21-Sep-94	0.0048
U10	0.6	0.3	UV-Wire	Exit	21-Sep-94	0.0048
U11	0.6	0.3	UV-Wire	Exit	21-Sep-94	0.0048
U12	0.6	0.3	UV-Wire	Exit	21-Sep-94	0.0048
U13	0.6	0.3	UV-Wire	Exit	21-Sep-94	0.0048
U14	0.6	0.3	UV-Wire	Exit	21-Sep-94	0.0048
U15	0.6	0.3	UV-Wire	Exit	21-Sep-94	0.0048
V01	0.6	0.5	UV-Wire	Exit	21-Sep-94	0.0048
V02	0.6	0.5	UV-Wire	Exit	21-Sep-94	0.0048
V03	0.6	0.5	UV-Wire	Exit	21-Sep-94	0.0048
V04	0.6	0.5	UV-Wire	Exit	21-Sep-94	0.0048
V05	0.6	0.5	UV-Wire	Exit	21-Sep-94	0.0048
V06	0.6	0.5	UV-Wire	Exit	21-Sep-94	0.0048
V07	0.6	0.5	UV-Wire	Exit	21-Sep-94	0.0048
V08	0.6	0.5	UV-Wire	Exit	21-Sep-94	0.0048
V09	0.6	0.5	UV-Wire	Exit	21-Sep-94	0.0048
V10	0.6	0.5	UV-Wire	Exit	21-Sep-94	0.0048
V11	0.6	0.5	UV-Wire	Exit	21-Sep-94	0.0048
V12	0.6	0.5	UV-Wire	Exit	21-Sep-94	0.0048
V13	0.6	0.5	UV-Wire	Exit	21-Sep-94	0.0048
V14	0.6	0.5	UV-Wire	Exit	21-Sep-94	0.0048

Run Number	M ₀	z/b	Type	Inlet/Exit	Date	Blowing
V15	0.6	0.5	UV-Wire	Exit	21-Sep-94	0.0048
W01	0.6	0.5	UV-Wire	Exit	21-Sep-94	Off
W02	0.6	0.5	UV-Wire	Exit	21-Sep-94	Off
W03	0.6	0.5	UV-Wire	Exit	21-Sep-94	Off
W04	0.6	0.5	UV-Wire	Exit	21-Sep-94	Off
W05	0.6	0.5	UV-Wire	Exit	21-Sep-94	Off
W06	0.6	0.5	UV-Wire	Exit	21-Sep-94	Off
W07	0.6	0.5	UV-Wire	Exit	21-Sep-94	Off
W08	0.6	0.5	UV-Wire	Exit	21-Sep-94	Off
W09	0.6	0.5	UV-Wire	Exit	21-Sep-94	Off
W10	0.6	0.5	UV-Wire	Exit	21-Sep-94	Off
W11	0.6	0.5	UV-Wire	Exit	21-Sep-94	Off
W12	0.6	0.5	UV-Wire	Exit	21-Sep-94	Off
W13	0.6	0.5	UV-Wire	Exit	21-Sep-94	Off
W14	0.6	0.5	UV-Wire	Exit	21-Sep-94	Off
W15	0.6	0.5	UV-Wire	Exit	21-Sep-94	Off
X01	0.6	0.7	UV-Wire	Exit	21-Sep-94	0.0048
X02	0.6	0.7	UV-Wire	Exit	21-Sep-94	0.0048
X03	0.6	0.7	UV-Wire	Exit	21-Sep-94	0.0048
X04	0.6	0.7	UV-Wire	Exit	21-Sep-94	0.0048
X05	0.6	0.7	UV-Wire	Exit	21-Sep-94	0.0048
X06	0.6	0.7	UV-Wire	Exit	21-Sep-94	0.0048
X07	0.6	0.7	UV-Wire	Exit	21-Sep-94	0.0048
X08	0.6	0.7	UV-Wire	Exit	21-Sep-94	0.0048
X09	0.6	0.7	UV-Wire	Exit	21-Sep-94	0.0048
X10	0.6	0.7	UV-Wire	Exit	21-Sep-94	0.0048
X11	0.6	0.7	UV-Wire	Exit	21-Sep-94	0.0048
X12	0.6	0.7	UV-Wire	Exit	21-Sep-94	0.0048
X13	0.6	0.7	UV-Wire	Exit	21-Sep-94	0.0048
X14	0.6	0.7	UV-Wire	Exit	21-Sep-94	0.0048
X15	0.6	0.7	UV-Wire	Exit	21-Sep-94	0.0048
Y01	0.6	0.7	UV-Wire	Exit	21-Sep-94	Off
Y02	0.6	0.7	UV-Wire	Exit	21-Sep-94	Off
Y03	0.6	0.7	UV-Wire	Exit	21-Sep-94	Off
Y04	0.6	0.7	UV-Wire	Exit	21-Sep-94	Off
Y05	0.6	0.7	UV-Wire	Exit	21-Sep-94	Off
Y06	0.6	0.7	UV-Wire	Exit	21-Sep-94	Off
Y07	0.6	0.7	UV-Wire	Exit	21-Sep-94	Off
Y08	0.6	0.7	UV-Wire	Exit	21-Sep-94	Off
Y09	0.6	0.7	UV-Wire	Exit	21-Sep-94	Off
Y10	0.6	0.7	UV-Wire	Exit	21-Sep-94	Off
Y11	0.6	0.7	UV-Wire	Exit	21-Sep-94	Off
Y12	0.6	0.7	UV-Wire	Exit	21-Sep-94	Off
Y13	0.6	0.7	UV-Wire	Exit	21-Sep-94	Off
Y14	0.6	0.7	UV-Wire	Exit	21-Sep-94	Off

Run Number	M _o	z/b	Type	Inlet/Exit	Date	Blowing
Y15	0.6	0.7	UV-Wire	Exit	22-Sep-94	Off
Z01	0.6	0.5	UW-Wire	Exit	22-Sep-94	0.0048
Z02	0.6	0.5	UW-Wire	Exit	22-Sep-94	0.0048
Z03	0.6	0.5	UW-Wire	Exit	22-Sep-94	0.0048
Z04	0.6	0.5	UW-Wire	Exit	22-Sep-94	0.0048
Z05	0.6	0.5	UW-Wire	Exit	22-Sep-94	0.0048
Z06	0.6	0.5	UW-Wire	Exit	22-Sep-94	0.0048
Z07	0.6	0.5	UW-Wire	Exit	22-Sep-94	0.0048
Z08	0.6	0.5	UW-Wire	Exit	22-Sep-94	0.0048
Z09	0.6	0.5	UW-Wire	Exit	22-Sep-94	0.0048
Z10	0.6	0.5	UW-Wire	Exit	22-Sep-94	0.0048
Z11	0.6	0.5	UW-Wire	Exit	22-Sep-94	0.0048
Z12	0.6	0.5	UW-Wire	Exit	22-Sep-94	0.0048
Z13	0.6	0.5	UW-Wire	Exit	22-Sep-94	0.0048
Z14	0.6	0.5	UW-Wire	Exit	22-Sep-94	0.0048
Z15	0.6	0.5	UW-Wire	Exit	22-Sep-94	0.0048
A*01	0.6	0.5	UW-Wire	Exit	22-Sep-94	Off
A*02	0.6	0.5	UW-Wire	Exit	22-Sep-94	Off
A*03	0.6	0.5	UW-Wire	Exit	22-Sep-94	Off
A*04	0.6	0.5	UW-Wire	Exit	22-Sep-94	Off
A*05	0.6	0.5	UW-Wire	Exit	22-Sep-94	Off
A*06	0.6	0.5	UW-Wire	Exit	22-Sep-94	Off
A*07	0.6	0.5	UW-Wire	Exit	22-Sep-94	Off
A*08	0.6	0.5	UW-Wire	Exit	22-Sep-94	Off
A*09	0.6	0.5	UW-Wire	Exit	22-Sep-94	Off
A*10	0.6	0.5	UW-Wire	Exit	22-Sep-94	Off
A*11	0.6	0.5	UW-Wire	Exit	22-Sep-94	Off
A*12	0.6	0.5	UW-Wire	Exit	22-Sep-94	Off
A*13	0.6	0.5	UW-Wire	Exit	22-Sep-94	Off
A*14	0.6	0.5	UW-Wire	Exit	22-Sep-94	Off
A*15	0.6	0.5	UW-Wire	Exit	22-Sep-94	Off
101	0.6	0.3	UW-Wire	Exit	22-Sep-94	0.0048
102	0.6	0.3	UW-Wire	Exit	22-Sep-94	0.0048
103	0.6	0.3	UW-Wire	Exit	22-Sep-94	0.0048
104	0.6	0.3	UW-Wire	Exit	22-Sep-94	0.0048
105	0.6	0.3	UW-Wire	Exit	22-Sep-94	0.0048
106	0.6	0.3	UW-Wire	Exit	22-Sep-94	0.0048
107	0.6	0.3	UW-Wire	Exit	22-Sep-94	0.0048
108	0.6	0.3	UW-Wire	Exit	22-Sep-94	0.0048
109	0.6	0.3	UW-Wire	Exit	22-Sep-94	0.0048
110	0.6	0.3	UW-Wire	Exit	22-Sep-94	0.0048
111	0.6	0.3	UW-Wire	Exit	22-Sep-94	0.0048
112	0.6	0.3	UW-Wire	Exit	22-Sep-94	0.0048
113	0.6	0.3	UW-Wire	Exit	22-Sep-94	0.0048
114	0.6	0.3	UW-Wire	Exit	22-Sep-94	0.0048

Run Number	M ₀	z/b	Type	Inlet/Exit	Date	Blowing
115	0.6	0.3	UW-Wire	Exit	22-Sep-94	0.0048
201	0.6	0.3	UW-Wire	Exit	22-Sep-94	Off
202	0.6	0.3	UW-Wire	Exit	22-Sep-94	Off
203	0.6	0.3	UW-Wire	Exit	22-Sep-94	Off
204	0.6	0.3	UW-Wire	Exit	22-Sep-94	Off
205	0.6	0.3	UW-Wire	Exit	22-Sep-94	Off
206	0.6	0.3	UW-Wire	Exit	22-Sep-94	Off
207	0.6	0.3	UW-Wire	Exit	22-Sep-94	Off
208	0.6	0.3	UW-Wire	Exit	22-Sep-94	Off
209	0.6	0.3	UW-Wire	Exit	22-Sep-94	Off
210	0.6	0.3	UW-Wire	Exit	22-Sep-94	Off
211	0.6	0.3	UW-Wire	Exit	22-Sep-94	Off
212	0.6	0.3	UW-Wire	Exit	22-Sep-94	Off
213	0.6	0.3	UW-Wire	Exit	22-Sep-94	Off
214	0.6	0.3	UW-Wire	Exit	22-Sep-94	Off
215	0.6	0.3	UW-Wire	Exit	22-Sep-94	Off
301	0.6	0.7	UW-Wire	Exit	22-Sep-94	0.0048
302	0.6	0.7	UW-Wire	Exit	22-Sep-94	0.0048
303	0.6	0.7	UW-Wire	Exit	22-Sep-94	0.0048
304	0.6	0.7	UW-Wire	Exit	22-Sep-94	0.0048
305	0.6	0.7	UW-Wire	Exit	22-Sep-94	0.0048
306	0.6	0.7	UW-Wire	Exit	22-Sep-94	0.0048
307	0.6	0.7	UW-Wire	Exit	22-Sep-94	0.0048
308	0.6	0.7	UW-Wire	Exit	22-Sep-94	0.0048
309	0.6	0.7	UW-Wire	Exit	22-Sep-94	0.0048
310	0.6	0.7	UW-Wire	Exit	22-Sep-94	0.0048
311	0.6	0.7	UW-Wire	Exit	22-Sep-94	0.0048
312	0.6	0.7	UW-Wire	Exit	22-Sep-94	0.0048
313	0.6	0.7	UW-Wire	Exit	22-Sep-94	0.0048
314	0.6	0.7	UW-Wire	Exit	22-Sep-94	0.0048
315	0.6	0.7	UW-Wire	Exit	22-Sep-94	0.0048
401	0.6	0.7	UW-Wire	Exit	22-Sep-94	Off
402	0.6	0.7	UW-Wire	Exit	22-Sep-94	Off
403	0.6	0.7	UW-Wire	Exit	22-Sep-94	Off
404	0.6	0.7	UW-Wire	Exit	22-Sep-94	Off
405	0.6	0.7	UW-Wire	Exit	22-Sep-94	Off
406	0.6	0.7	UW-Wire	Exit	22-Sep-94	Off
407	0.6	0.7	UW-Wire	Exit	22-Sep-94	Off
408	0.6	0.7	UW-Wire	Exit	22-Sep-94	Off
409	0.6	0.7	UW-Wire	Exit	22-Sep-94	Off
410	0.6	0.7	UW-Wire	Exit	22-Sep-94	Off
411	0.6	0.7	UW-Wire	Exit	22-Sep-94	Off
412	0.6	0.7	UW-Wire	Exit	22-Sep-94	Off
413	0.6	0.7	UW-Wire	Exit	22-Sep-94	Off
414	0.6	0.7	UW-Wire	Exit	22-Sep-94	Off

Run Number	M ₀	z/b	Type	Inlet/Exit	Date	Blowing
415	0.6	0.7	UW-Wire	Exit	22-Sep-94	Off
501	0.6	0.7	UW-Wire	Exit	29-Sep-94	0.0048
502	0.6	0.7	UW-Wire	Exit	29-Sep-94	0.0048
503	0.6	0.7	UW-Wire	Exit	29-Sep-94	0.0048
504	0.6	0.7	UW-Wire	Exit	29-Sep-94	0.0048
505	0.6	0.7	UW-Wire	Exit	29-Sep-94	0.0048
506	0.6	0.7	UW-Wire	Exit	29-Sep-94	0.0048
507	0.6	0.7	UW-Wire	Exit	29-Sep-94	0.0048
508	0.6	0.7	UW-Wire	Exit	29-Sep-94	0.0048
509	0.6	0.7	UW-Wire	Exit	29-Sep-94	0.0048
510	0.6	0.7	UW-Wire	Exit	29-Sep-94	0.0048
511	0.6	0.7	UW-Wire	Exit	29-Sep-94	0.0048
512	0.6	0.7	UW-Wire	Exit	29-Sep-94	0.0048
513	0.6	0.7	UW-Wire	Exit	29-Sep-94	0.0048
514	0.6	0.7	UW-Wire	Exit	29-Sep-94	0.0048
515	0.6	0.7	UW-Wire	Exit	29-Sep-94	0.0048

Appendix C: Hot-Film Probe Data Repeatability

Two sets of data were collected with a uw-film probe at $z/b = 0.7$ with

$\frac{m_j}{m_d} = 0.0048$. Run 3 was conducted on 22 September 1994, and run 5 was conducted

on 29 September 1994. While the test section was not disassembled between these two runs, comparison of results obtained from each set of data gave some indication of the repeatability of both turbulent and mean flow data acquired by hot-film probes.

Figures C1 through C4 compare mean velocity, xz-plane mean flow angle, turbulence intensity, and turbulent shear stress data obtained during each run. Generally, repeatability of the data was very good. Table C1 summarizes the maximum difference in the value measured for each of the above quantities:

Table C1
Repeatability Check Maximum Difference Summary

Quantity	Maximum Difference Between Set 3 and Set 5
Mean Velocity \bar{u}	5.0 m/s
Mean Velocity \bar{w}	0.69 m/s
xz-Plane Flow Angle	0.53 deg
Turbulence Intensity $\frac{u'_{rms}}{\bar{u}}$	0.008
Turbulence Intensity $\frac{w'_{rms}}{\bar{w}}$	0.005
Turbulent Shear Stress Component $\frac{u' w'_{rms}}{\bar{u}^2}$	0.0025

The values in Table C1 are consistent with the results of the uncertainty analysis summarized in Chapter 3 and detailed in Appendix A. Note also that these values represent the maximum error measured at any station; as Figures C1 through C4 suggest, data from each set agreed much more closely at most measurement stations.

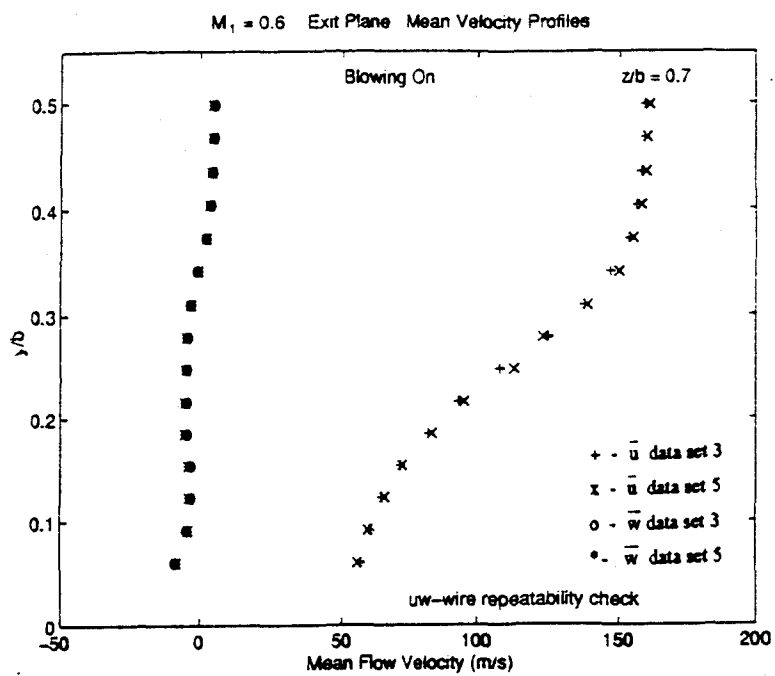


Figure C1: Hot-Film Repeatability Check Mean Velocity Comparison

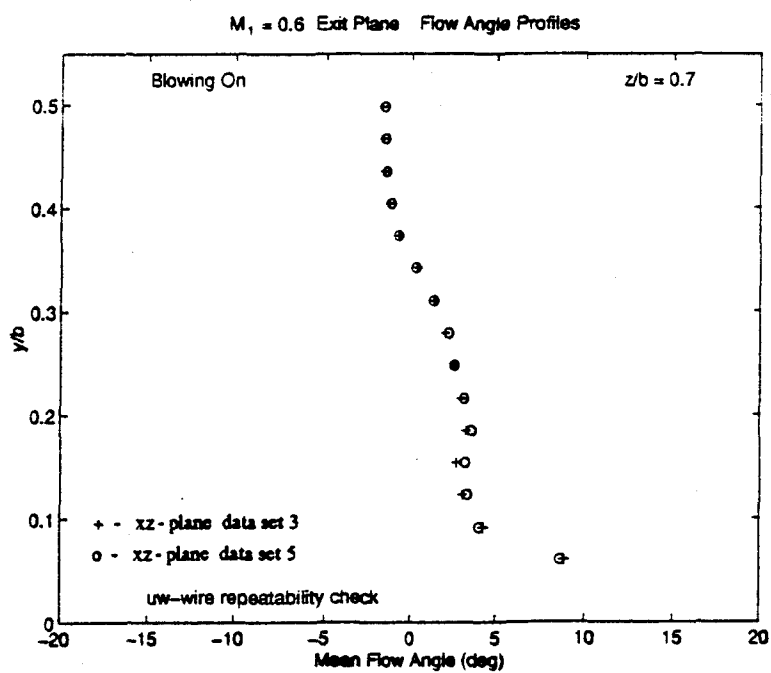


Figure C2: Hot-Film Repeatability Check Flow Angle Comparison

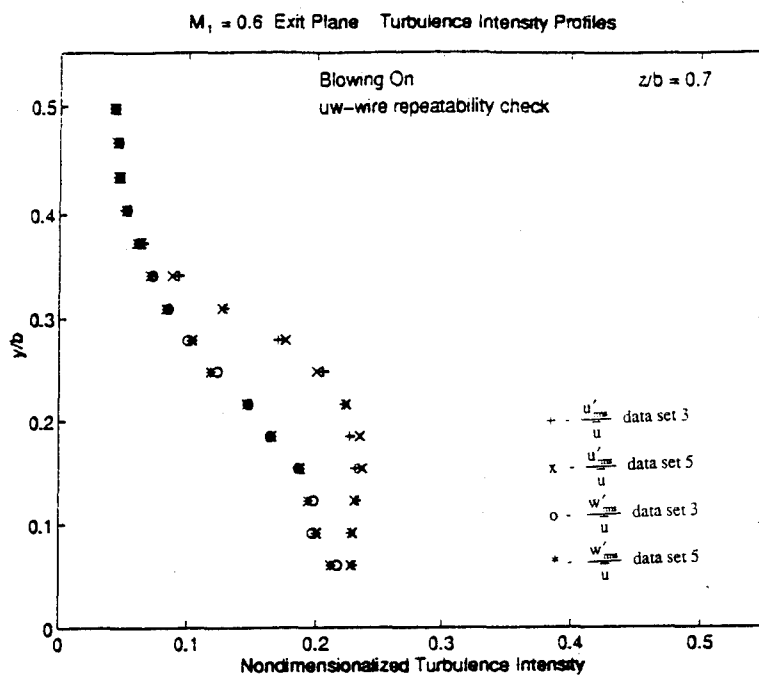


Figure C3: Hot-Film Repeatability Check Turbulence Intensity Comparison

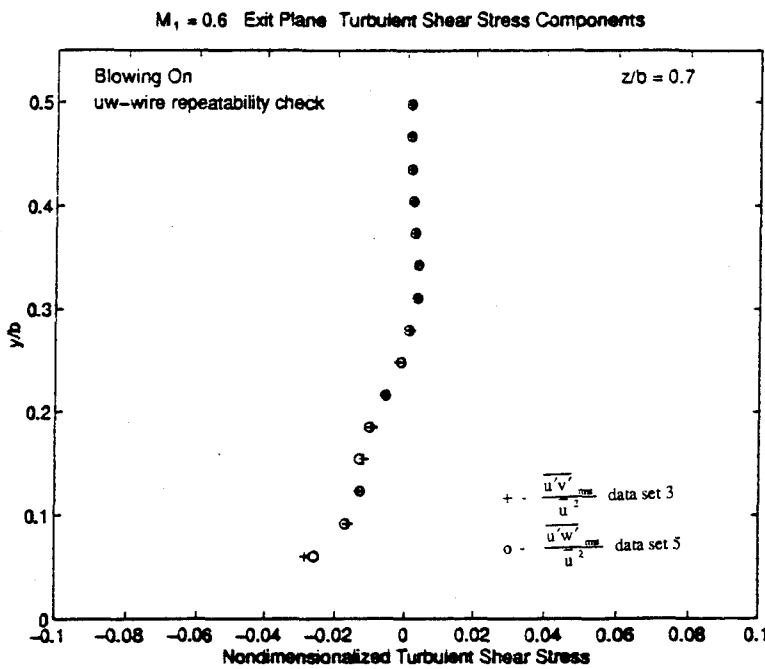


Figure C4: Hot-Film Repeatability Check Turbulent Shear Stress Comparison

Bibliography

Adkins, R. C. "Diffusers and their Performance Improvement by means of Boundary Layer Control," in AGARD-R-654, Special Course on Concepts for Drag Reduction. Neuilly sur Seine, France, 1977

Anderson, B. H. and J. Gibb. "Application of Computational Fluid Dynamics to the Study of Vortex Flow Control for the Management of Inlet Distortion," Proceedings of the AIAA/SAE/ASME/ASEE 28th Joint Propulsion Conference and Exhibit. Paper No. AIAA-92-3177. New York: American Institute of Aeronautics and Astronautics, 1992.

Ball, W. H. "Tests of Wall Blowing Concepts for Diffuser Boundary Layer Control," Proceedings of the AIAA/SAE/ASME 20th Joint Propulsion Conference. Paper No. AIAA-84-1276. New York: American Institute of Aeronautics and Astronautics, 1984.

Ball, W. H. "Experimental Investigation of the Effects of Wall Suction and Blowing on the Performance of Highly Offset Diffusers," Proceedings of the AIAA/SAE/ASME 19th Joint Propulsion Conference. Paper No. AIAA-83-1169. New York: American Institute of Aeronautics and Astronautics, 1983.

Ball, W. H. "Effects of S-Bends on Diffuser Internal Performance and Turbulence Characteristics," Proceedings of the AIAA/ASME/SAE/ASEE 22nd Joint Propulsion Conference. Paper No. AIAA-86-1459. New York: American Institute of Aeronautics and Astronautics, 1986.

Bansod, P. and P. Bradshaw. "The Flow in S-Shaped Ducts," The Aeronautical Quarterly 23-2: 131-140 (May 1972).

Bowersox, R. D. W. Compressible Turbulence in a High Speed High Reynolds Number Mixing Layer. PhD dissertation. Virginia Polytechnic Institute and State University, Blacksburg, Va, 1992.

Compton, D. A. and J. P. Johnston. "Streamwise Vortex Production by Pitched and Skewed Jets in a Turbulent Boundary Layer," Proceedings of the 29th Aerospace Sciences Meeting. Paper No. AIAA-91-0038. New York: American Institute of Aeronautics and Astronautics, 1991.

Fiedler, R. A. and F. B. Gessner. "Influence of Tangential Fluid Injection on the Performance of Two-Dimensional Diffusers," J Basic Engineering srs D 94-3 (September 1972).

Hill, P. G. and C. R. Peterson. Mechanics and Thermodynamics of Propulsion. Reading, MA: Addison-Wesley Publishing Co., 1992

Johnston, J. P. and M. Nishi. "Vortex Generator Jets - A Means for Passive and Active Control of Boundary Layer Separation," Proceedings of the 27th Aerospace Sciences Meeting. Paper No. AIAA-89-0564. New York: American Institute of Aeronautics and Astronautics, 1989.

Kline, S. J. "On the Nature of Stall," J Basic Engineering srs D 81-3: 305 (September 1959).

Lee, C. C., and W. A. Price. Subsonic Diffusers for Highly Survivable Aircraft. Technical Report AFWAL-TR-86-3025. McDonnell Aircraft Division, McDonnell-Douglas Corp, St Louis, MO, 1986.

Lin, J. C., F. G. Howard, D. M. Bushnell, and G. V. Selby. "Investigation of Several Passive and Active Methods for Turbulent Flow Separation Control," Proceedings of the AIAA 21st Fluid Dynamics, Plasma Dynamics, and Lasers Conference. Paper No. AIAA-90-1598. New York: American Institute of Aeronautics and Astronautics, 1990.

Mattingly, J. D. and others. Aircraft Engine Design. Washington, DC: American Institute of Aeronautics and Astronautics, 1987.

Neumann, H. E., L. A. Povinelli, and R. E. Coltrin. "An Analytical and Experimental Study of a Short S-Shaped Subsonic Diffuser of a Circular Inlet," Proceedings of the 18th AIAA Aerospace Sciences Meeting. Paper No. AIAA-80-0386. New York: American Institute of Aeronautics and Astronautics, 1980.

Nicolet, Incorporated. Nicolet Multipro Data Acquisition System Operations Manual. Madison, WI: Nicolet, Inc., 1991.

Nicoll, W. B. and B. R. Ramaprian. "Performance of Conical Diffusers with Annular Injection at Inlet," J Basic Engineering srs D 92-4: 827-835 (December 1970).

Prandtl, L. "Uber Flussigkeitsbewegung ei sehr kleiner Reibung," Proceedings of the Third International Math Congress. Heidelberg, 1904.

Prandtl, L. Essentials of Fluid Dynamics. London: Blackie, 1952.

Rehman, F., and J. M. Bowyer, Jr. "Turbulent Incompressible Air Flow Through S-Shaped Ducts with Cross-Sectional Area Change," Proceedings of the 3rd Joint ASCE/ASME Mechanics Conference. New York: American Society of Mechanical Engineers, 1989.

Schetz, J. A. Boundary Layer Analysis. Englewood Cliffs, NJ: Pentice Hall, 1993.

Schlichting, H. Boundary Layer Theory (Seventh Edition). New York: McGraw-Hill, Inc, 1979.

Selby, G. V., J. C. Lin, and F. G. Howard. "Control of Low-Speed Turbulent Separated Flow Using Jet Vortex Generators," Experiments in Fluids, 12-6: 394-400.

Smith, C. F., J. E. Bruns, G. J. Harloff, and J. R. DeBonis. Three-dimensional Compressible Turbulent Computations for a Diffusing S-Duct. Technical Report NASA-CR-4392. National Aeronautics and Space Administration, Washington, DC, April 1992.

Tindell, R.H. "Highly Compact Inlet Diffuser Technology," Proceedings of the AIAA/SAE/ASME/ASEE 23rd Joint Propulsion Conference. Paper No. AIAA-87-1747. New York: American Institute of Aeronautics and Astronautics, 1987.

TSI, Incorporated. IFA 100 System Instruction Manual. St Paul, MN: TSI, Inc., 1987.

Vakili, A. D., J. M. Wu, W. R. Hingst, and C. E. Towne. "Comparison of Experimental and Computational Compressible Flow in an S-Duct," Proceedings of the 22nd AIAA Aerospace Sciences Meeting. Paper No. AIAA-84-0033. New York: American Institute of Aeronautics and Astronautics, 1984.

Vakili, A. D., J. M. Wu, M. K. Bhat, and P. Liver. "Compressible Flow in a Diffusing S-Duct with Flow Separation," Proceedings of the First International Symposium on Transport Phenomenon. Washington, DC: Hemisphere Publishing Corp., 1987.

Wallis, R. A. "The Use of Air Jets for Boundary Layer Control," Aero Note 110, Aerodynamics Research Laboratories, Australia, 1952.

Wellborn, S. R., B. A. Reichert, and T. H. Okiishi. "An Experimental Investigation of the Flow in a Diffusing S-Duct," Proceedings of the AIAA/SAE/ASME/ASEE 28th Joint Propulsion Conference and Exhibit. Paper No. AIAA-92-3622. New York: American Institute of Aeronautics and Astronautics, 1992.

White, F. M. Viscous Fluid Flow (Second Edition). New York: McGraw-Hill, Inc., 1991.

Zhang, X. and M. W. Collins. "Flow and Heat Transfer in a Turbulent Boundary Layer through Skewed and Pitched Jets," AIAA Journal, 31-9: 1590-1598 (September 1993).

Vita

Captain Michael B. Senseney was born on 4 May 1967 in Lackawanna, New York. He graduated from Hamburg High School in Hamburg, New York in 1985 and attended Rensselaer Polytechnic Institute in Troy, New York. He graduated from RPI with a Bachelor of Science in Aeronautical Engineering in May, 1989. He was a distinguished graduate of the Air Force ROTC program there and received a regular commission in the USAF upon graduation. In October, 1989, he was assigned to the 6510th Test Wing (now 412th Test Wing) at Edwards AFB, CA. He began his tour there as a performance and flying qualities engineer on the MC-130H Combat Talon II test program while awaiting clearance to the B-2 flight test program. He served first as a propulsion and performance flight test engineer, then as lead propulsion flight test engineer on the B-2 program, between March 1990 and October 1992. He was then chosen to manage all B-2 inflight icing and rain testing as a lead all-weather systems flight test engineer. In May 1993, Captain Senseney entered the Air Force Institute of Technology's School of Engineering.

Permanent Address:
S-4686 Parker Rd
Hamburg, NY 14075